TESE DE DOUTORADO

Through-The-Earth (TTE) Communication Systems: Channel characterization and system evaluation.

Josua Daniel Pena Carreno

Brasília, Dezembro de 2020

UNIVERSIDADE DE BRASÍLIA

FACULDADE DE TECNOLOGIA

UNIVERSIDADE DE BRASÍLIA
Faculdade de Tecnologia

TESE DE DOUTORADO

Through-The-Earth (TTE) Communication Systems: Channel characterization and system evaluation.

Josua Daniel Pena Carreno

Tese de Doutorado submetida ao Departamento de Engenharia Elétrica como requisito parcial para obtenção do grau de Doutor em Engenharia Elétrica

Banca Examinadora

Prof. Dr. Adoniran Judson de Barros Braga, FT/UnB _____
Orientador

Prof. Dr. Karlo Queiroz da Costa, UFPA _____
Examinador Externo

Dr. Robson Domingos Vieira, FAPEG/GO _____
Examinador Externo

Prof. Dr. Leonardo Rodrigues Araujo Xavier de Menezes _____
Examinador Interno

FICHA CATALOGRÁFICA

CARRENO, JOSUA DANIEL PENA
Through-The-Earth (TTE) Communication Systems:Channel characterization and system evaluation. [Distrito Federal] 2020.
xvi, 114 p., 210 x 297 mm (ENE/FT/UnB, Doutor, Engenharia Elétrica, 2020).
Tese de Doutorado - Universidade de Brasília, Faculdade de Tecnologia.
Departamento de Engenharia Elétrica

1. Through-The-Earth communication	2. Effective conductivity
3. Low frequency antennas	4. Underwater communication
I. ENE/FT/UnB	II. Título (série)

REFERÊNCIA BIBLIOGRÁFICA

CARRENO, J.D.P. (2020). *Through-The-Earth (TTE) Communication Systems:Channel characterization and system evaluation.*. Tese de Doutorado, Publicação PPGENE.TD-171/20, Departamento de Engenharia Elétrica, Universidade de Brasília, Brasília, DF, 114 p.

CESSÃO DE DIREITOS

AUTOR: Josua Daniel Pena Carreno
TÍTULO: Through-The-Earth (TTE) Communication Systems:Channel characterization and system evaluation..
GRAU: Doutor em Engenharia Elétrica ANO: 2020

Josua Daniel Pena Carreno
Depto. de Engenharia Elétrica (ENE) - FT
Universidade de Brasília (UnB)
Campus Darcy Ribeiro
CEP 70919-970 - Brasília - DF - Brasil

To Ana and Jonathan for always helping me to go on.

Josua Daniel Pena Carreno

ACKNOWLEDGEMENTS

I would like to thank:
Judson Braga for being a good teacher and a strict leader.
Vale Technological Institute for the financial support.
Companhia do Metropolitano do Distrito Federal for lending their space to carry out the tests.
Professors Andre Noll, Leonardo Aguayo, Paulo Portela, and Wellinton Avelino do Amaral for always having a constructive critics and giving good ideas to solve problems.
Bernardo Bianchetti, Rodrigo Severo and Jérôme Baglin from the Espeleo grupo de Brasilia for their invaluable support during the expedition to the Ecos Cave.
Luiz de Freitas for doing a great job on digging the trench for the underwater tests.
Anderson Barros Rodrigues from UnBall for lending me a place at his office to carry out some tests.
Henrique Berilli, João Antônio Rondina, Lucas Baião Pires, Lucas Sousa e Silva, Geordana Maeda, Tony Reis, Sofia Disegna, Bruno Chaves, Breno Dantas de Castro, Gabriel Teixeira Brasil, and Vitor Guedes da Silva for contributing to build the simulation and measurement platform, without your excellent work this thesis would not be possible.
Rodrigo Fischer, Gustavo Viana, Gabriel Helbourn, Rafael Lima, Jackson Costa and Hiago Machado for always keeping a positive attitude and being excellent colleagues.
Calil Bento, George Caldwell, and Bruno Farias for believing in me and letting me show my potential.
José Pereira Filho, Jorge Aranda, Stephanie Álvarez, André Vieira, Laila Wanick, Luziane Wanick, Alan Lima, Luciano Grossi, Uirá Godoy, Renielton Santos, Linniker Corado, Leandro Machado, Leonardo Alencar, Fabrício Mirandes, Cássio Giorgio Couto Coelho, Felipe Xavier, and Harisson Sampaio for being there for me through this turmoil.
Rennan Gladson Sousa da Cruz, your unconditional friendship made me a better person.
Gustavo Sandri et Marcio Sales merci pour être avec moi quand j'ai touché le fond.
And my grandmother and my father for taking care of me from heaven.

Josua Daniel Pena Carreno

ABSTRACT

THROUGH-THE-EARTH (TTE) COMMUNICATION SYSTEMS: CHANNEL CHARACTERIZATION AND SYSTEM EVALUATION.

Author: Josua Daniel Pena Carreno

Supervisor: Adoniran Judson de Barros Braga

Programa de Pós-graduação em Engenharia Elétrica

Brasilia, December 2020

This thesis presents realistic simulations of a variety of underground structures to statistically characterize magnetic field attenuation, propagation loss and apparent electric conductivity in coal mines. Additionally, several antennas were designed, built and tested in underground and underwater environments both for data transmission and for noise measurements. Furthermore, a software platform were developed to generate and process signals in Through-The-Earth communication.

RESUMO

SISTEMAS DE COMUNICAÇÃO ATRAVÉS DA TERRA (TTE): CARACTERIZAÇÃO DO CANAL E AVALIAÇÃO DO SISTEMA.

Autor: Josua Daniel Pena Carreno

Orientador: Adoniran Judson de Barros Braga

Programa de Pós-graduação em Engenharia Elétrica

Brasília, dezembro de 2020

Esta tese apresenta simulações realistas de uma variedade de estruturas subterrâneas para caracterizar estatisticamente a atenuação do campo magnético, perda de propagação e condutividade elétrica aparente em minas de carvão. Além disso, várias antenas foram projetadas, construídas e testadas em ambientes subterrâneos e subaquáticos, tanto para transmissão de dados quanto para medições de ruído. Igualmente, uma plataforma de software foi desenvolvida para gerar e processar sinais na comunicação através da Terra.

INDEX

FIGURE LIST

TABLE LIST

LIST OF SYMBOLS

LATIN SYMBOLS

Md	Magnetic moment	$[A/m^2]$

GREEK SYMBOLS

δ	Skin Depth
μ_0	Vacuum Magnetic Permeability
ϵ_0	Vacuum Electric permittivity

ABBREVIATIONS

CST	Computer Simulation Technology
DSP	Digital Signal Processor
EFIE	Electric Field Integral Equation
FDTD	Finite-Difference Time-Domain
FEM	Finite Element Method
FSK	Frequency Shift Keying
GPD	Generalized Pareto Distribution
HHS	Homogeneous Half-Space
IC	Infinite Conductive Medium
ISI	InterSymbol Interference
MFIE	Magnetic Field Integral Equation
MoM	Method of Moments
NIOSH	National Institute for Occupational Safety and Health (United States of America)
PEC	Perfect Electric Conductor
PMC	Perfect Magnetic Conductor
PSK	Phase Shift Keying
RF	Radio Frequency
RFID	Radio Frequency IDentification
RMSE	Random Mean Square Error
SSB	Single Side Band
TS	Thin Sheet model
TTA	Through-The-Air
TTE	Through-The-Earth
TTW	Through-The-Wire
VBA	Visual Basic for Applications

1 INTRODUCTION

A mass of mineral or fossil substance found in the nature whether in the surface or underneath it and has commercial value can be denominated as a mine [3]. Specifically, underground mines are challenging environments due to the presence of high humidity, suspended dust, explosive or toxic gases and other dangerous situations that put on risk workers' safety. Thus, it is necessary to provide a reliable communication system that connect different underground sites to the surface without the use of cabling.

This scenario is similar to many construction applications, such as subway tunnels, but under more challenging conditions. However, a particular feature of the mine sites is that through ore extraction the mine grows proportionally, such expansion requires updates on the telecommunications system. This is particularly true in Through-The-Air (TTA) communications, where air within the mine is the propagation medium and whose form and type alters the propagation path. For instance, pillar-based open pit mines provide different propagation conditions than underground mines in which exist a tendency to create a low propagation loss rate waveguide effect within the tunnels.

With regard to soil characteristics, every mine present a unique combination of strata and minerals that impact directly the electric conductivity that in turn conditions the equipment used in that mine. In the case of Through-The-Earth communications, a more conductive medium can reduce the penetration range. Similarly, for other radio-frequency underground communications systems, as TTA and TTW (Through-The-Wire), differences on conductivity in the mine tunnel structure can affect reflection and diffraction coefficients and, consequently, the propagation channel time dispersion.

The majority of wireless communication systems use high frequency radiating antennas operating in far-field and the transmission medium close to vacuum conditions. If rocks, soil, water, and other materials with non-neglecting electric conductivity, are part of the propagation medium, those systems cannot be used. That is because exists a significant attenuation rate of electromagnetic waves at those frequencies which compromise the installation of TTA communication systems.

Through-The-Earth communication electromagnetic waves are used to establish a link between surface and the underground mine using soil as propagation medium. Generally, frequencies below 30 kHz are used in magnetic induction transmission to overcome the attenuation inside the conductive medium. Such telecommunication systems are also prone to atmospheric and man-made noise, which can forbid the communication.

Keeping a permanent link with personnel working inside confined spaces has been always an important issue in the mining industry. Through the use of communication system it is possible to keep real-time contact with all team members and transmitting back-up information in emergency

situations. Furthermore, new applications related to mining automation require efficiency and reliability in cases of emergency, because cable and high frequency systems are vulnerable to break during explosions, fires, floods, and landslides.

Another structure related to the mining process, that is important to control, is the tailings dam that is usually build to store the by-products generated during operation. The traditional manner of controlling the structural stability is by using cabled sensors that are installed in the interior of those constructions, method that is also vulnerable to cable damages so TTE communication could be an additional tool to backup these systems.

A US congressional settlement has been expanded, requiring reliable underground mine emergency systems. This regulation was named Mining Improvement Act and the new Emergency Response Act (MINER Act) and led to research on TTE communication. According to this law, this system must be wireless, bidirectional, allow surface mine communication to the underground mine and vice-versa, and allow monitoring buried people and equipment.

Some models were created to simulate the TTE propagation ([4], [5], [6]), having different levels of complexity, starting from a simple homogeneous channel to a much more close-to-reality model yet complicated to implement. The simplest approach for transmitting a magnetic field created by an electrically small loop antenna is obtained by considering vacuum as a homogeneous medium, neglecting any boundary conditions and assuming an evenly distributed current in the loop. Then this homogeneous medium can be modified to replace the vacuum with an Infinite Conductive (**IC**) medium.

Wait in [7] and [8] enhance this simplification and propose a model for describing a homogeneous half-space (**HHS**) model in which an antenna is located in the air over a homogeneous electric conductivity ground σ different from the vacuum, and the other antenna is buried some distance from the surface. Hill and Wait later on [9] proposed a model that modifies Wait's **HHS** model by introducing a conductive barrier between air and ground. This barrier has a higher electrical conductivity than the homogeneous ground where the receiver antenna is buried due to the use of superficial electrical equipment and cables. Finally, in 2014, Lincan, in his doctoral thesis [5], proposed a more complex and laborious model that characterized the propagation medium as a stratified soil with different electrical conductivities for each layer. This model also provides for the configuration of two loop antennas with one of them buried at a specific distance.

In the consulted literature, there are few studies on the apparent electrical conductivity in stratified underground mine soils. In fact, some simplifications are made by assuming homogeneous materials or using a weighted arithmetic average to produce equivalent conductivity and then using the homogeneous model.

This study aims the statistical characterization of the electrical conductivity and attenuation of the magnetic field in underground coal mines. The proposed model is based on measurements made at 94 different coal mines in the United States in the 1970s and on electromagnetic simulations using numerical methods. In addition, a TTE platform is proposed for transmission/reception on short to medium distances, describing the MATLAB software developed to

carry out channel transfer function estimation, Bit Error Rate calculation and tuning circuit characterization. Afterwards, measurements results are presented, specifically noise measurements, TTE transmission from a subway station to the exterior and from an underground cave. Aside from this, some simulations and measurements on tailing dam-likes scenarios are included.

This thesis is organized as follows: Chapter 2 introduces a brief revision of general concepts related to mining and underground communication; Chapter 3 brings a revision about propagation models for TTE communication systems; Chapter 4 presents the models of apparent conductivity, propagation loss and magnetic field attenuation; in Chapter 5 are described the antennas that were built for TTE communication; in Chapter 6 can be found the measurement and simulation results; and finally in Chapter 8 are presented the conclusions and some proposals for future researches related to TTE.

2 STATE OF THE ART

In this chapter the most relevant subjects found in literature related to underground communication are presented. An entire approach is outside the scope of this work. Sections 2.1 and 2.3 introduce concepts related to mines and communication in such environment. Section 2.2 presents the concept of tailing dams and some sensors used on them. Section 2.4 presents some communication protocols used for underground communication. Finally, in section 2.6 some commercial equipment are presented.

2.1 MINE

Before introducing the concept of Underground Communication, it is important to show some characteristics of a mine. In general, depending on where the material is placed and how it is exploited, it is possible to classify mines in two types: surface and underground mines shown in figure 2.1 and described hereafter:

Surface mine:

According to [10], if the mineral is on the surface or close to it, that mine is classified as surface mine. Such kind of mine is exploited through open pits or open cast methods, generally mining in benches or steps. This type of mine is the most predominant used around the world, due to its high productivity, its low operating cost, and its usually good safety conditions.

Underground mine:

In the same manner, according to [10] and [11], if the mineral is several meters under the surface it is denoted as underground mine. Moreover, the wall type and the roof support technique used present a wider classification: unsupported, supported or caves. This designation is defined as follows:

- `Unsupported mine:` such excavation type presents mineral deposits that are roughly tabular, generally associated with strong ore and surrounding rock, which makes possible building structures without artificial pillars for supporting of the openings.
- `Supported mines:` this type of mine shows weak rock structures that require external pillars and other structures to guarantee its integrity. The most common construction method used is the "Cut-and-fill" method, which comprises the fill of voids, created during mineral extraction, with rock waste, rock leftovers, cemented gravel, or other suitable materials, to build the walls.
- `Caved mines:` those mines are built by caving and extracting extensive amounts of rocks that can result in the formation of a surface depression, similar to a natural cave that permits

the mineral exploitation without the use of additional structures.

(a) Surface mine (b) Underground mine

Figure 2.1: Surface and underground mines.
Sources: a) Madeline Ratcliffe [12] b) ASSOCIATED PRESS [13]

2.2 TAILING DAMS

According to Vick in [14] in the mining process usually the ore is ground before separate mineral from unused materials. To carry out this separation, several processes are used as Gravity Separation, Froth Floatation, and Magnetic separation [15], which use water to handle the residues more efficiently. That mined metal constitutes a small percentage of the total mass of the ore and, therefore, the vast majority of the mined material ends up as finely ground mud that is usually disposed in tailing dams. Such structures are susceptible to geological and environmental events that could compromise their stability, so it is mandatory to monitor them in a regular basis by the means of instruments as shown in Figure 2.2.

As shown by Geokon on their online catalogue [16], there are several cabled sensors that are connected to an external transmitter that sends the data to a central station.

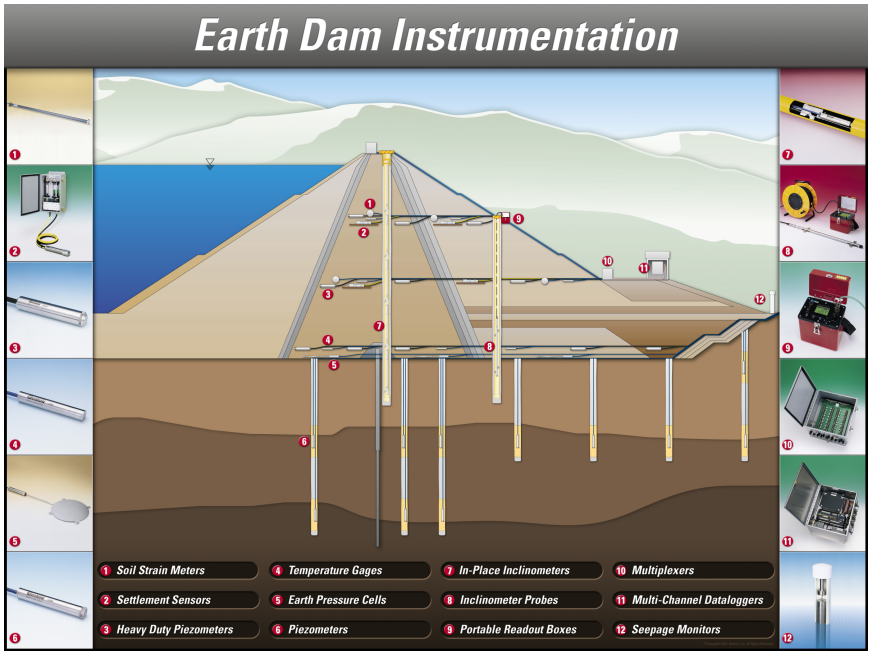

Figure 2.2: Earth dam instrumentation
Source: Geokon [16]

In this sense, Hajduk and Paikowsky in [17] carried out a performance evaluation of instruments in a soil pile to test several parameters such as total radial pressure, interior stress wave, and temperature, by the means of wired sensors. They concluded that about 20% of those instruments stopped working during the tests, which was an excessively high rate failure, but overall it was a successful experiment. Such tests may be improved with the adaptation of low-frequency wireless transmitters that could be used to provide a redundant link to the system.

More recently, Mining3 -an Australian research center- is working on Autonomous sensors monitoring tailings dams and spoil dumps, by the development of a Magnetic Pulse (MP) communication method, which is: "similar to the cave tracking method, but with higher data transfer rates and Tx/Rx capability in the one module" [18]. However, the report abstract was only published on the The Australian Coal Industry's Research Program website on March 2020 without disclosing any details regarding the communication system, though the author affirms they transmitted groundwater pressure and position data through a 220m communication link [19].

In summary, the fact of using cables to transmit data from within the dam or a soil pile, represents an opportunity of developing another solutions that uses Through-The-Earth communication instead, as attaching a transmitter to the existing sensor or create a new product that embeds a TTE transmitter. Therefore, in this work some simulations of TTE transmission in soils similar to those found in tailing dams will be presented.

2.3 UNDERGROUND MINE COMMUNICATION

Communication with and between workers working in confined spaces has always been a vitally important issue for the mining industry, because communication systems make possible to establish real-time contact with all team members and transfer support information during emergency situations. More recently, with the increasing mining automation, it is also important to ensure reliable connection between different equipment and surface. There are several communication systems available in underground mines in the world, with systems based on coaxial cables or fiber optics being the most used. However, they are not efficient in the event of a disaster, can suffer breakages and isolate workers when explosions, fires, floods and burials occur. Additionally, those networks must be flexible enough to be reconfigured in environments whose topology changes in a regular basis.

The vast majority of wireless communication systems use radio-frequency (RF) communication topologies based on radiant antennas, distant field and transmission medium with near vacuum electrical characteristics. In the event that rocks, soil, water and other materials of non-negligible electrical conductivity become the propagation medium between the communication tips, the high attenuation rate of high frequency electromagnetic waves does not allow the use of such systems [20]. Within the available telecommunication systems to provide reliable communication there are three categories: Through-The-Wire (TTW), Through-The-Air (TTA) and Through-The-Earth (TTE). The first two types are being described in this section and the third one will be presented in the next section.

2.3.1 TTW: Through-The-Wire

Communication systems that use guided media such as coaxial cables, metallic wires, fiber optics, or wave-guides are identified as Through-The-Wire systems [21]. In the mining industry there are several TTW systems that have been used throughout its history, some of them are presented below:

- `Magnetic telephone`: This is a communication device operated by a manual crank that is constructed by: a manual generator, a battery, two pair of bells, a switch-hook, cable coupling, a transmitter, and a receiver.

  For its operation, it is necessary to use the battery as a direct current source to activate the transmitter. Then, an alternate current of about 100 V @ 15-20 Hz is generated by actuating the crank, which, in turn, propagates a signal through the cable coupling to activate the bells at the receiver and the call is initiated when the switch-hook is unhooked. Even though this is a useful gadget, its weak signal does not allow the use of several telephones [22]. In figure 2.3 a picture of one of this devices is shown.

Figure 2.3: Magnetic telephone
Source: ATM MINING TELEPHONES [23]

- `Optical fiber`: these systems use long thin clear glass or plastic rods usually covered with a plastic layer that confines light in its interior 2.4. Despite its higher price, glass fibers allow long distance and high velocity data transmission with less losses when compared to their plastic counterpart [24]. In the mining industry, optical fibers' reliability and transmission speed permit monitoring critical systems as fire system, closed-circuit television, automatic systems among others. [25]

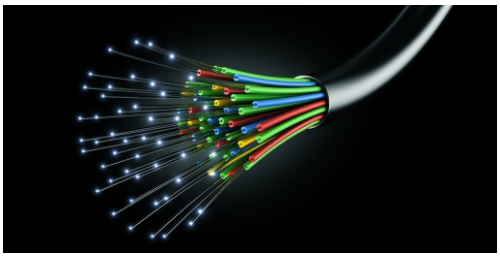

Figure 2.4: Fiber optics
Source: Telecommunications Industry Association [26]

- `Radiating cable`: this technology might be seen as a hybrid between Through-The-Wire and Through-The-Air because it uses a remodeled coaxial cable to transmit and receive signal inside tunnels. The main difference of these cables, when compared to coaxial wires, is that the outside woven shield is replaced with a multi slotted copper layer that acts as an aperture array, which makes mandatory the signal amplification at regular distances, usually every 350 to 500 m [27]. Miners in the interior of a mine use this system via portable two way devices working in VHF (150 MHz) and UHF (450 MHz) bands [28].

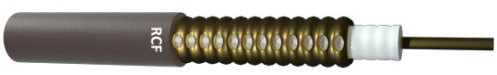

Figure 2.5: Radiating cable
Source: CDCP [27]

2.3.2 TTA: Through-The-Air

Through-The-Air communication, i.e., wireless systems, is a suitable solution for underground mines due to its rapid installation and adaptability to mine structure changes. In the particular case of underground mines, the interior tunnels grow along with the mine expansion so the telecommunication systems must be upgraded at the same rate [21]. The inner architecture plays an important role in the telecommunication project since open mines built with supporting columns provide a different propagation channel when compared to tunneled mines.

In present days, these systems are usually formed by short-range wireless systems such as those listed below [29]:

- `Wave-guides tunnels`: Forooshane et al. in [30] identified the possibility of using underground mine tunnels as wave-guides with low propagation loss index, and described six analytic models for electromagnetic propagation inside tunnels. This article presents a simple propagation model of transmission in Transverse Magnetic and Transverse Electric modes, which is shown in Figure 2.6.

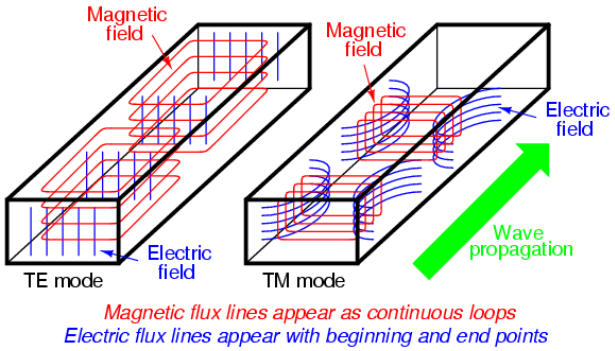

Figure 2.6: TE and TM modes in wave-guides
Source: Physics Stack Exchange [31]

- `Zigbee`: Pei et al. in [32] describe this wireless system as a technique distributed under IEEE recommendation 802.15.4 for low-power consumption and low-cost personal area networks, which commonly operates at frequencies around 2.4 GHz for industrial applications, scientific solutions and medical radios (ISM). Such networks are often used as backbone for RFID transmission in underground mines.

- `Wireless LAN`: based on IEEE 802.11, these non licensed networks provide elevated transmission data rates [33] and are usually used to form low-priced ad hoc networks that are also simple to deploy in underground mines. Thanks to its versatility, those networks are easy to maintain and to upgrade when it is needed.

- `Radio-Frequency Identification - RFID`: these systems are based on passive or active tags that permit the unique identification of persons, objects or equipment in the interior of an underground mine from distances that vary from 8 m for passive tags to 100

m for active tags. The signals are received by fixed routers and are sent to base-stations that monitor user's position in real time [29].

2.3.3 TTE: Through-The-Earth

Through-the-earth communication (TTE) consist of using electromagnetic waves to establish a link between the surface and the underground mine using the earth as a means of propagation. Transmission is typically by magnetic induction at frequencies below 30 kHz, which may be subject to atmospheric noise and equipment-produced harmonics, limiting communication performance, especially in the uplink [20]. These systems are described thoroughly in the next sections.

2.4 COMMON PROTOCOLS USED IN UNDERGROUND COMMUNICATION

TTA systems are the most common in underground communication, therefore, the protocols associated with them are the most used; however, some of them can be adapted to be used in TTE applications. For instance, Yin in [34] analyzed the MINECOM protocol which is based on Time Division Multiple Access - Time Division Duplexing (TDMA-TDD) for controlling media access.

With regard to routing protocols, Jing et al in [35] worked on the Geographical and Energy Aware Routing (GEAR) to generate a hybrid routing protocol for mobile nodes in which the nodes have restricted communication with other nodes due to the distance between them and their relative motion. Those restrictions permit to augment their life expectancy.

Chetan and Wu in [36, 37] carried out performance analysis on Destination-Sequenced Distance-Vector (DSDV) and on Ad hoc On-demand Distance Vector (AODV) within coal mines. They considered package end-to-end delay, video transmission spreading and loss rate. Similarly, Sun et al in [38] studied the impact of latency, jitter and spreading in voice and video transmission within mines.

Wenqi and Zhao in [39] developed a multi-hop routing protocol based on a recursive algorithm to connect close nodes and find the shortest path from one position to another. The algorithm uses the Received Signal Strength Indication (RSSI) metrics and the Radio Pulse MG2455 transmitter to verify the protocol.

Jiang in [40] modeled a routing protocol that uses the underground internal architecture to identify a main tunnel connected to smaller tunnels as branches. Then, according the nodal distribution and clustering, the network is optimized to assure its balance and good clusterization.

Zheng in [41] worked on underground sensor networks positioning and wireless underground channels, specifically on the development of a cross-layered structures that may mitigate the impact of obstacles within the telecommunication system.

2.5 PREVIOUS WORK RELATED TO CHANNEL MODELING FOR TTE COMMUNICATIONS

Regarding the electromagnetic behavior of underground communication, several authors worked on different models to predict how magnetic and electric fields behave inside a mine. Some of them developed deterministic models to estimate the magnetic field generated by a loop antenna at every point in space within an underground environment [8, 9, 42]. Wait and Durkin in their work proposed models that consider electromagnetic propagation in a stratified soil, yet they limited the structure to a small number of homogeneous layers separating both transmitter and receiver.

Similarly, Yan presented in [5] a more general and complicated model to characterize the propagation medium as a multi-layer soil with diverse electric conductivity for each horizontal stratum. Nevertheless, his model was applied for five layers only for being computationally challenging.

The underground propagation model proposed by Wait in [8] (named Wait model in this document) has been used as a reference in several studies, notably in researches related to apparent conductivity empirical modeling [42, 43]. The apparent conductivity concept is an artificial measurement that connects magnetic and electric fields values, sensed in challenging environments, to a simpler homogeneous one-layer soil model with an equivalent conductivity.

Little in [44] presented a measurement campaign carried out by him at the American Bureau of Mines showing the feasibility of using Through-The-Earth communication in coal mines. Those measurements took place in the 1970s and 1980s in 94 coal mines across the United States, they used coaxially aligned loop antennas operating at frequencies from 630 Hz to 3030 Hz. The database created in that report constitutes one of the most complete sources of TTE data and has been used by many authors to develop, among others, apparent conductivity models as those present in [42] and [43]. Durkin and Lincan provide an apparent conductivity analysis that can help to estimate field strength in coal mines; however, they did not present any information about channel variability at the optimal frequency because of the small diversity of frequency considered by Lincan.

In recent years, Mendes et al. in [45] proposed a short-range TTE communication platform that use magnetic induction to estimate channel parameters and digital transmission performance. Similarly, Ralchenko et al. in [46] simulated TTE communication at 4 kHz in the interior of a multiple floor building, in which every floor was modeled as a thin sheet. In addition, Kisseleff in [47] proposed a TTE-based wireless underground sensor network to locate silent target nodes inside an underground spaces. In a similar manner, Korolkova et al. in [48] proposed a numerical attenuation model of electrical field for TTE communication inside underground mines.

2.6 SOME EQUIPMENT FOR UNDERGROUND COMMUNICATION

After the Mine Improvement and New Emergency Response (MINER) Act was approved in 2006 (see Appendix I), the American National Institute for Occupational Safety and Health (NIOSH) supported the development of several communication and tracking devices for underground mines [49]. Five prototypes where carried out by five different companies: **Alertek**, **E-Spectrum Technologies**, **Lockheed Martin**, **Stolar**, and **Ultra Electronics**. One of them senses electric fields and the rest detect magnetic field by the means of loop antennas.

Those systems support unidirectional or bidirectional communication up to 300 m for voice and 600 m for text at frequencies from 3.15 kHz to 4.82 kHz. Some of them have a location feature based on triangulation that uses a single tone in the up-link transmission that is detected by superficial receivers which in turn treat the received signals to locate the underground transmitter.

Regarding modulation, some prototypes use Single Side Band and others digital Phase Shift Keying (PSK) or Frequency Shift Keying (FSK). The companies also tested some noise cancellation techniques as a comb filter for 60-Hz harmonics [49]. Additionally, some of those prototypes became commercial products [50] and are described below:

- `Flex Alert`: this device provides a unidirectional communication system that can be used from outside to the mine interior in emergency situations. It uses a loop antenna, of ten to 120 m long positioned on the mine surface, to send a low frequency electromagnetic field and activate a flicker lamp and a secondary LED on each miner's helmets [33].

- `TeleMag`: this bidirectional system operates in a band from three to eight kHz, uses the modulation technique Single-Side Band (SSB) and tracking Digital Signal Processor (DSP) filters, which attenuates the induced noise generated by the transmitted signal harmonics and improves Signal-To-Noise ratio. Additionally, it features a fixed base-to-base system with filamentary loop antennas in both transmission and reception, which permit communication up to 100 m. However, this device is not in compliance with MSHA regulations related to risk of explosions and/or fire [33].

- `Personal Emergency Device (PED)`: this unidirectional device permits wireless down-link transmission of preprepared text messages to the interior of a mine and, in the opposite direction, it is possible to use a leaky feeder cable to complete the bidirectional system [33]. This system is particularly useful for explosives remote detonation and equipment remote control.

- `MagneLink MCS`: **Lockheed Martin** commercialized this equipment after carrying out joint experiments with the NIOSH, it is a bidirectional device featuring voice and text transmission, and localization by using low-frequency magnetic waves. Specifically, it uses a 130 m wide circular loop antenna for transmission and a multiple turns receiving antenna providing text and voice transfer up to 500 m.

- `Canary`: this product was developed by the Canadian company **Vital Alert** [51] to provide bidirectional digital communication for data and voice transmission using software defined radio operating between 300 Hz and 9 kHz. In addition, they included adaptive modulation scheme to deliver transmission rates from 9 bps to 1 kbps.

In recent years, the MSHA approved several new devices for underground communication and listed them in [52]. That list includes some TTE-oriented devices as: "Rescue Dog" from E-Spectrum Tech Inc, which uses metallic rods inserted in soil to provide wireless communication between the surface and the galleries; "Model STE 1000 Subsurface Through-The-Earth Communication System" from Strata Products World-Wide LLC, which specifications were not available on their website by October 2019.

3 ELECTROMAGNETIC FIELD BEHAVIOR IN UNDERGROUND MINES FOR THROUGH-THE-EARTH COMMUNICATION.

Environments as challenging as underground mines present several difficulties for using well-known traditional telecommunication systems as Wi-Fi, Global System for Mobile Communications (GSM), Long-Term Evolution (LTE) and other high frequency technologies. This gives origin to the necessity of other technologies that can mitigate the attenuation suffered by wireless signals when are propagated in a medium different than air.

Particularities of each site, as soil conductivity, affect the electromagnetic waves passing through soil. That change can be better described by the diffusion equation (3.1) rather than the wave equation (3.3).

$$\nabla^2 H = \mu\sigma\frac{\partial H}{\partial t} \tag{3.1}$$

$$\nabla^2 H = \mu\epsilon\frac{\partial^2 H}{\partial t^2} \tag{3.2}$$

These telecommunication systems use soil to propagate the transmitted signals. It is also known that magnetic field decays exponentially as a function of distance in the interior a soil and that decay may be described by the skin depth δ:

$$\delta = \sqrt{\frac{2}{\mu_0\sigma\omega}}, \tag{3.3}$$

in which μ_0 is the vacuum magnetic conductivity, σ soil electrical conductivity, and ω the angular frequency. In this kind of medium, the skin depth is the distance in which the propagation plane wave intensity reduces in a e^{-1}th of its initial value, and it is inversely proportional to square root frequency. This characteristic facilitates the use of low frequencies to have less propagation loss, usually in Very Low Frequencies (VLF 3-30 kHz) or Low Frequencies (30-300 kHz) [4].

Figure 3.1 represents a classical TTE working system composed by an external antenna located outside a mine and another within an underground space. Their physical dimensions are determined by the operation conditions needed in a specific site, and some examples of this is going to be presented in the following chapters.

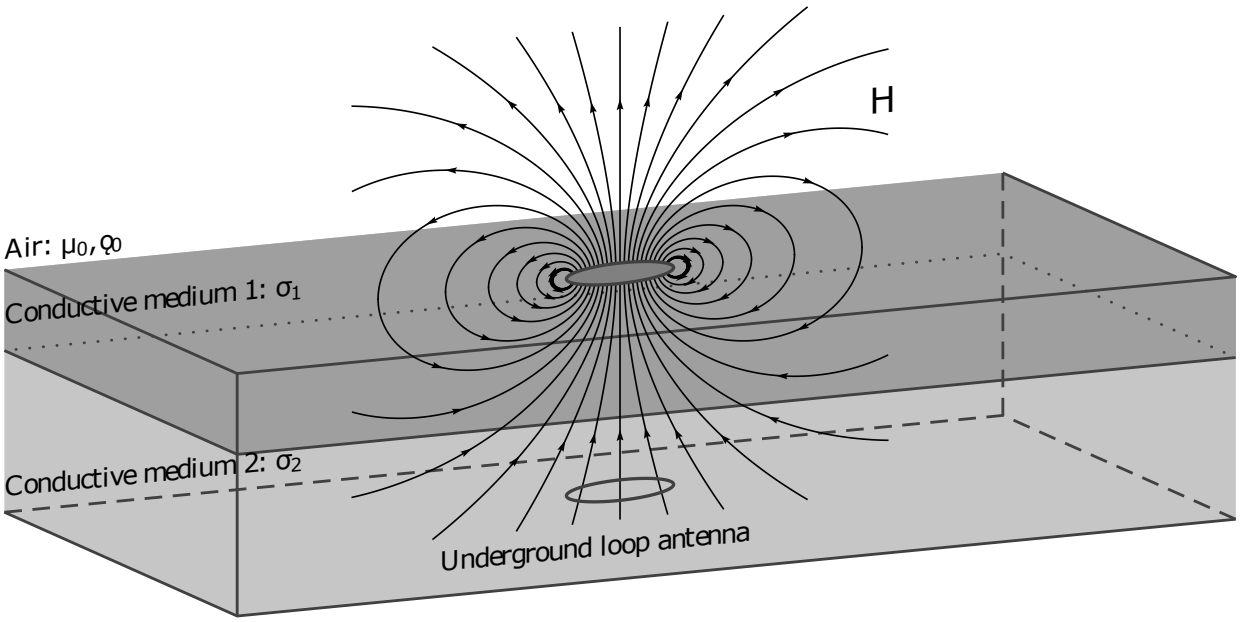

Figure 3.1: Through-The-Earth communication.

3.1 FIELD ZONES

3.1.1 Free space

According to OSHA in [1], propagation in air or in vacuum might be classified in field zones named Reactive Near Field, Radiant Near Field, Transition Zone and Far field.

Precisely, in both Reactive and Radiant zones, the electromagnetic field is created by the interaction and interference of the antenna with itself, which can be described as an antenna array made of small dipoles contributing to the resulting field.

In opposition to this behavior, the far field zone is characterized by:

- The transmitting antenna can be observed as punctual radiating source,
- There is a fixed ratio between electric and magnetic field,
- The phase between electric and magnetic field is the same,
- The resulting field can be seen as a plane wave front.

The transition zone is in between both behaviors presenting characteristics of one and another zone. Figure 3.2 shows this field classification.

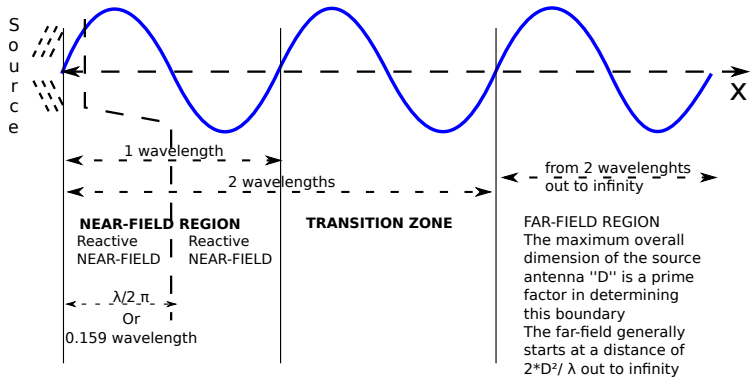

Figure 3.2: Field regions for typical Antennas
Adapted from: OSHA [1]

3.1.2 Within a conductive medium

In a similar manner, Gibson in [4] proposed an alternate field zone classification for propagation within a conductive medium.

In the vicinity of the transmitting antenna, the field exhibits a "quasi-static" behavior and follows the electrostatic laws, varying in time and attenuating as a function of inverse cube distance. Farther from the source, yet in near-field, the conductive medium increments the attenuation significantly. While in far-field, the electromagnetic field attenuates linearly as a function of the inverse distance and the induced currents, inside the media, generate parasitic fields that contribute to the total received field [53]. A similar behavior of mixed characteristics of near and far field is seen in the transition zone.

In order to show the differences between both approaches, the following Table 3.1 lists the borders of all field zones for a conductive and a non conductive media where the transmission and reception antennas are at $r = 300$ m apart from each other.

Model	*Type of approximation*	*Conditions*
Vacuum	Reactive near field	$0 < r < \frac{\lambda_0}{2\pi}$
	Radiant near field	$\frac{\lambda_0}{2\pi} < r < \lambda_0$
	Transition zone	$\lambda_0 < r < 2\lambda_0$
	Far field	$r > 2\lambda_0$
Conductive Medium	Quasi-static	$r << \frac{\lambda_{soil}}{2\pi}$
	Near field	$r^2 << (\frac{\lambda_{soil}}{2\pi})^2$
	Transition zone	$r = \frac{\lambda_{soil}}{2\pi}$
	Far field	$r >> \frac{\lambda_{soil}}{2\pi}$

Table 3.1: Comparison between near and far field for free space and a conductive medium.
[2]

The free space scenario is working at 10 kHz, giving a wavelength λ = 30 km and makes the whole system to be in the Reactive Near-Field ($\frac{\lambda_0}{2\pi} \approx 4775$ m).

In the contrary, the conductive medium is characterized by an electric conductivity $\sigma = 10^{-3}$ S/m and magnetic permeability of vacuum $\mu = \mu_0$, resulting in a wavelength of approximately

160 m ($\frac{\lambda_{soil}}{2\pi} = \delta \approx 160$ m < 300 m), which implies that the system is in the far field.

3.2 THEORETICAL MODELS FOR TTE PROPAGATION

A useful quantity related to loop antennas is the magnetic moment m_d in (3.4), because it establish a connection between the physical dimensions and its inductive transmission capacity.

$$m_d = N_{tx} I_{tx} S_{tx} \tag{3.4}$$

Such transmission loop dimensions are defined as:

- N_{tx} transmitter loop number of turns
- I_{tx} RMS current value for a unique transmission frequency
- S_{tx} loop area

Considering the power dissipation equation $P_{tx} = R_{tx} I_{tx}^2$, it is possible to realize that the magnetic moment rise will rise the power dissipation in the transmitting antenna. Such augmentation is due to changes on the antenna resistance R generated by alterations on N_{tx} and S_{tx}, that affect the transmission current which in turn affects the magnetic field generation and power transmission.

An approximation for the magnetic field, generated by a electrically small loop antenna and described by Starkey et al. in [54], considers the vacuum as a homogeneous medium, neglects boundary conditions and assumes that the current in the loop is uniformly distributed. Moreover, in the source vicinity ($r << \lambda/2\pi$), the time varying magnetic field intensity is analogous to that calculated by the Biot-Savart law [53]. Then, for a loop antenna, the quasi-static magnetic field is estimated by:

$$\boldsymbol{H}_{qe} = \frac{m_d}{4\pi r^3}\{2\cos(\theta)\hat{\boldsymbol{r}} + \sin(\theta)\hat{\boldsymbol{\theta}}\}, \tag{3.5}$$

in which $\hat{\boldsymbol{r}}$, $\hat{\boldsymbol{\theta}}$ are the spherical coordinates radial and elevation vectors respectively.

3.2.1 Infinite Conductive Medium (IC)

Starkey et al. in [54] adapted the vacuum infinite plane model to a Infinite Conductive (**IC**) medium by changing the wave-number to $k_{soil} = (1-j)/\delta$. Subsequently, Gibson in [4] extended this approximation to up-link and down-link, being the spherical coordinate equation:

$$\boldsymbol{H} = \frac{m_d}{4\pi r^3} e^{-jT} e^{-T}\{2\cos\theta(1 + (1+j)T)\hat{\boldsymbol{r}} + \sin\theta(1 + (1+j)T + 2jT^2)\hat{\boldsymbol{\theta}}\}, \tag{3.6}$$

in which $T = r/\delta = r\sqrt{\mu\sigma\omega/2}$ denotes a normalized by the skin-depth range that includes the contributions of soil losses. This parameter T may be interpreted as a position spacing normalized by a previously known distance *r*. An accurate representation of this scenario is presented in Figure 3.3, taking into consideration that all boundaries are infinite.

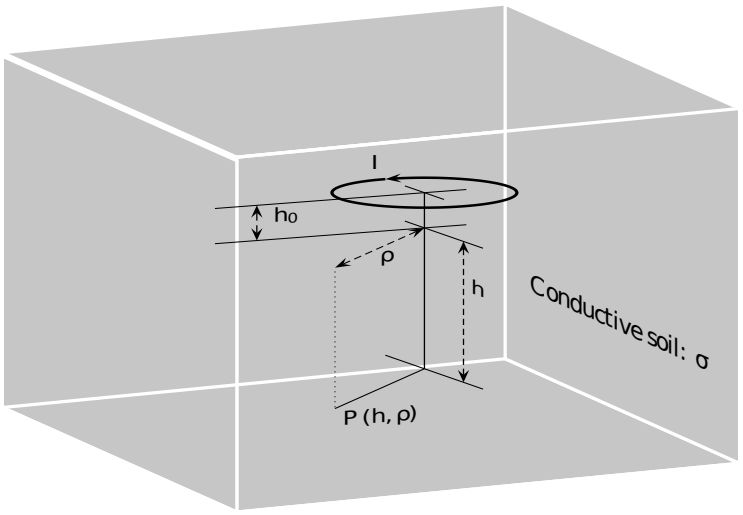

Figure 3.3: Infinite Conductive Medium **IC** with constant σ.

3.2.2 Homogeneous Half-Space model (HHS)

Wait in [8] presents the configuration shown in Figure 3.4, in which a wire loop antenna is positioned over ground at a height h_0 and the magnetic field is sensed at a distance h within the half-space homogeneous soil of conductivity σ. In order to describe the magnetic field, some considerations were made: the cylindrical coordinate system (ρ, ϕ, z) was used, and all distances were consider to be smaller than the free-space wavelength so all displacement currents can be neglected. Thus, the two H-field components for up-link $\boldsymbol{H}_{up}$ and down-link $\boldsymbol{H}_{down}$ are presented in equations (3.7) and (3.8), considering the vertical depth $\hat{\boldsymbol{z}}$ and horizontal distance $\hat{\boldsymbol{\rho}}$.

$$\boldsymbol{H}_{up} = \frac{m_d}{2\pi h^3}\int_0^\infty \beta(x)\{J_0(Dx)\hat{\boldsymbol{z}} - J_1(Dx)\hat{\boldsymbol{\rho}}\}dx, \tag{3.7}$$

$$\boldsymbol{H}_{down} = \frac{m_d}{2\pi h^3}\int_0^\infty \beta(x)\{J_0(Dx)\hat{\boldsymbol{z}} - J_1(Dx)\frac{(x^2 + j2\mathcal{T}^2)^{1/2}}{x}\hat{\boldsymbol{\rho}}\}dx, \tag{3.8}$$

in which

$$\beta(x) = \frac{J_1(Ax)}{Ax/2}\frac{x^3}{(x^2 + j2\mathcal{T}^2)^{1/2} + x}e^{-Zx}e^{-(x^2+j2\mathcal{T}^2)^{1/2}}, \tag{3.9}$$

and $A = a/h$, $D = \rho/h$, $Z = h_0/h$, $\mathcal{T} = h/\delta$, $\delta = \sqrt{\frac{2}{\omega\mu\sigma_a}}$, a is the loop radius, J_0 and J_1 are Bessel functions of the first kind.

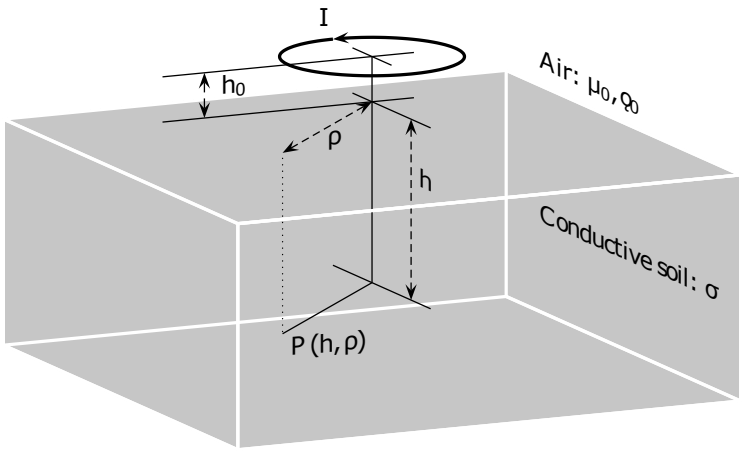

Figure 3.4: Geometry used to estimate the magnetic field at the point $P(h, \rho)$ for a circular loop antenna at h_0 above ground.

It can be seen that there is reciprocity on both vertical up and down link magnetic field; however, this behavior is not present in the horizontal components, that can even be neglected if the transmission and reception antennas are coaxially aligned, it is, when $\rho = 0$ or $\mathcal{T} = T$ which makes $J_1(Dx) = 0$. Similarly, in the **IC** model from (3.6) if $\theta = \pi$, the horizontal components become zero so the only remaining component is the vertical in $\hat{\boldsymbol{r}}$ direction.

Regarding antenna size, the **IC** model requires a small antenna in which the current has spacial uniformity, and the **HHS** model includes a correction factor $J_1(Ax)$ to compensate the antenna's dimension.

3.2.3 Thin sheet model (TS)

Hill and Wait suggested in [9] a modified **HHS** medium, shown in Figure 3.5, in which there is a barrier between soil and air that can be modeled by a thin sheet of material with a higher conductivity than the homogeneous soil below it. They justified the inclusion of this layer as a consequence of the common presence of cables and other equipment on the surface or close to it inside soil.

This model includes the term $\chi = j2\mathcal{T}^2\sigma_m\frac{h_1}{h}$ in the equations (3.7) and (3.8), being h_1 and σ_m the height and the conductivity of the thin interface layer respectively. Thus, the final equations can be restated as:

$$\beta(x) = \frac{J_1(Ax)}{Ax/2}\frac{x^3}{(x^2 + j2\mathcal{T}^2)^{1/2} + x + j2\mathcal{T}^2\sigma_m\frac{h_1}{h}}e^{-Zx}e^{-(x^2+j2\mathcal{T}^2)^{1/2}}, \tag{3.10}$$

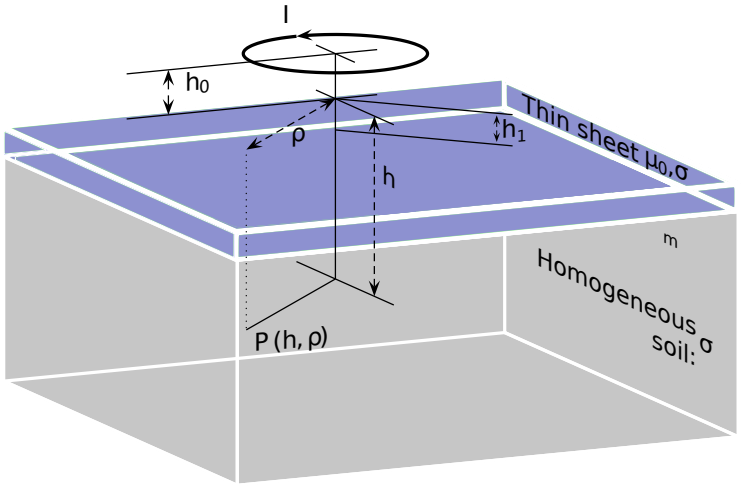

Figure 3.5: Geometry used for estimating the magnetic field at the point $P(h, \rho)$ for a circular loop antenna at h_0 above a thin sheet of conductive material.

3.2.4 Multi-layer model

Lincan on his doctoral thesis from 2014 [5] proposed an intricate model to describe a multi-layered soil used for TTE communication. The author started from a similar **HHS** model with two antennas separated by several conductive soil layers with diverse electric conductivites. Figure 3.6 depicts a similar scenario.

The behavior of both H and E field can be described by the following equations that use the cylindrical coordinates system:

$$\mathbf{E} = j\mu\omega \frac{\partial \Pi^*}{\partial \rho} \widehat{\phi} \tag{3.11}$$

$$\frac{\partial^2 \Pi^*}{\partial \rho \partial z} \widehat{\rho} = (j\mu\omega\sigma - \epsilon\mu\omega^2 - \frac{\partial^2}{\partial z^2}) \Pi^* \widehat{z} \tag{3.12}$$

in which Π^* varies according to every material layer, and depends on the transmitted signal T_i and is reflected R_i as follows:

$$\Pi_0^* = \frac{IA_{wire}}{4\pi} \int_0^\infty T_0(\lambda) e^{-k_0 z} J_0(\lambda\rho) d\lambda \tag{3.13}$$

$$\vdots$$

$$\Pi_i^* = \frac{IA_{wire}}{4\pi} \int_0^\infty (T_i(\lambda) e^{-k_1 z} + R_i(\lambda) e^{k_1 z}) J_0(\lambda\rho) d\lambda \tag{3.14}$$

$$\vdots$$

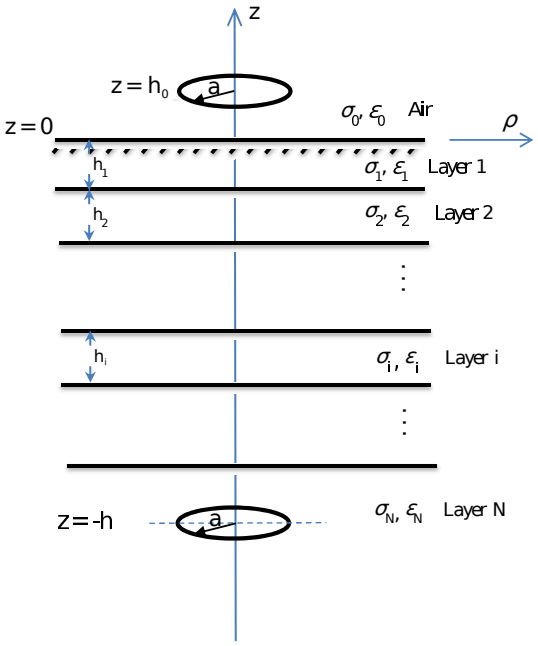

Figure 3.6: Stratified soil for Multi-layer model
Adapted from: Lincan[5]

$$\Pi_N^* = \frac{IA_{wire}}{4\pi} \int_0^\infty J_0(\lambda\rho) \left(\frac{\lambda}{k_N} e^{-k_N|z+h|} + R_N(\lambda) e^{k_N z} \right) d\lambda \tag{3.15}$$

The author establishes specific boundary conditions for each layer which gives $T_0(\lambda)$ as the only parameter to be estimated and is describe by the following equation:

$$T_0(\lambda) = \frac{\lambda 2^N \left(\Pi_{i=0}^{N-1} k_i\right) \left(e^{k_N(h-H'_N) - \sum_{i=1}^{N-1} k_i h_i}\right)}{L_0 + L_1 + L2... + L_{N-1}} \tag{3.16}$$

All terms L_i at denominator have no physical interpretation, whereas they may be seen as electric and magnetic field interactions within an arbitrary combination of m layers. The general equations describing those terms are presented below:

$$L_0 = \prod_{i=0}^{N-1} (k_i + k_{i+1}), \tag{3.17}$$

$$L_1 = \sum_{p=1}^{N-1} \left\{ e^{-2k_p h_p} \prod_{i=0}^{N-1} (k_i + (-1)^{\delta 1} k_{i+1}) \right\}, \tag{3.18}$$

$$L_2 = \sum_{p=1,q=2,p<q}^{N-1} \left\{ e^{(-2k_p h_p - 2k_q h_q)} \prod_{i=0}^{N-1} (k_i + (-1)^{\delta 2} k_{i+1}) \right\}, \tag{3.19}$$

$$\vdots$$

$$L_m = \sum_{\substack{p=1,q=2,r=3,\ldots,t=m,\\ p<q<r<\ldots<t}}^{N-1} \left\{ e^{(-2k_p h_p - 2k_q h_q - 2k_r h_r - \ldots - 2k_t h_t)} \prod_{i=0}^{N-1} (k_i + (-1)^{\delta m} k_{i+1}) \right\}, \tag{3.20}$$

$$\vdots$$

$$L_{N-1} = e^{(-2k_p h_p - 2k_q h_q - 2k_r h_r - \ldots - 2k_{N-1} h_{N-1})} \prod_{i=0}^{N-1} (k_i + (-1)^{\delta(N-1)} k_{i+1}), \tag{3.21}$$

Still, the author states that in general the term δm for L_m in the equation (3.20) may be estimated as the occurrence sum of k_i and k_{i+1} in the exponential term $e^{(-2k_p h_p - 2k_q h_q - 2k_r h_r - \ldots - 2k_t h_t)}$. Due to its complexity, the author used estimation for up to five different layers.

These models are described in the frequency domain since δ varies as a function of ω and they do not consider linear nor nonlinear distortions generated by the transmission circuit.

3.3 CHANNEL MODELING

For systems working at low frequencies it is usual to use voltage and current as quadripole input parameters, so this study uses impedance as reference parameter. In the case of frequencies below 30 kHz it is appropriate to utilize the concept of transfer impedance $Z(\omega)$ to relate both transmission and reception antennas, by the ratio between the transmission current $I_{tx}(\omega)$ and the reception induced voltage $V_{rx}(\omega)$:

$$Z(\omega) = V_{rx}(\omega)/I_{tx}(\omega). \tag{3.22}$$

In consonance with Faraday's law, an incident time variant magnetic field induces a voltage in a closed loop that changes according to the orthogonal flux entering in it [53]. The following equation describes the relation between the magnetic field and the induced voltage:

$$\begin{aligned} V_{rx}(\omega) &= -j\omega N_{rx} \oint_S \mu \boldsymbol{H} \cdot \boldsymbol{dS} \\ &= -j\omega\mu N_{rx} S_{rx} H \cos(\varphi) \end{aligned} \tag{3.23}$$

in which S_{rx} and N_{rx} are the loop area and its number of turns, respectively, and φ is the angle between the arriving magnetic field and the orthogonal loop axis. From (3.23) it is noticeable that higher frequencies attenuate the magnetic field, and at the same time the receiver introduce attenuation at low frequencies. Expressing $\boldsymbol{H}$ in spherical coordinates, $\boldsymbol{H_r}$ at the $\hat{\boldsymbol{r}}$ direction, and $\boldsymbol{H_\theta}$ at the $\hat{\boldsymbol{\theta}}$ direction gives:

$$V_{rx}(\omega) = -j\omega\mu N_{rx} S_{rx} \left[\boldsymbol{H_r} \cos(\theta - \theta_x) \cos(\theta_y) - \boldsymbol{H_\theta} \sin(\theta - \theta_x) \cos(\theta_y) \right], \tag{3.24}$$

in which θ_x e θ_y are rotation angles for the $\hat{\mathbf{x}}'$ and $\hat{\mathbf{y}}'$ axis, that are auxiliary axis created by

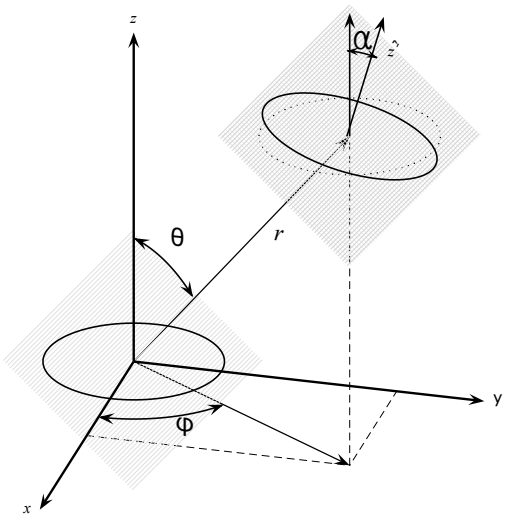

Figure 3.7: Geometry used to calculate the magnetic field between two circular loop antennas. The angle α formed by orthogonal vectors to the planes determined by the two antennas is the result of rotations around the $\hat{\mathbf{x}}'$ e $\hat{\mathbf{y}}'$ axis.

the $\phi - \frac{\pi}{2}$ rotation of the $\hat{\mathbf{z}}$ axis, being ϕ the azimuthal angle. Figure 3.7 illustrates the described geometry.

Performing a coordinate system change into cylindrical, the induced voltage as a function of $\boldsymbol{H_z}$ field in the $\hat{\boldsymbol{z}}$ direction, and $\boldsymbol{H_\rho}$, in the $\hat{\boldsymbol{\rho}}$ direction, gives:

$$V_{rx}(\omega) = -j\omega\mu N_{rx} S_{rx} \left[\boldsymbol{H_z} \cos(\theta_x)\cos(\theta_y) + \boldsymbol{H_\rho} \sin(\theta_x)\cos(\theta_y)\right]. \tag{3.25}$$

For a unique frequency current in the transmitter, the magnetic moment $m_d(\omega)$ expresses the complex power of a transmitting antenna for that specific frequency. Using the concept of transfer impedance in (3.22) and the normalized spatial frequency T, the equivalent equation of the transfer impedance for the **IC** model is:

$$Z_{\text{IC}}(T) = N_{tx} N_{rx} S_{tx} S_{rx} \left[\sqrt{G_r^{tx} G_r^{rx}}\boldsymbol{F_r} + \sqrt{G_\theta^{tx} G_\theta^{rx}}\boldsymbol{F_\theta}\right] \tag{3.26}$$

in which the normalized transmission and reception antennas gain polarized in the directions $\hat{\boldsymbol{r}}$ and $\hat{\boldsymbol{\theta}}$ are:

$$G_r^{tx} = \cos^2(\theta) \tag{3.27}$$

$$G_\theta^{tx} = \sin^2(\theta) \tag{3.28}$$

$$G_r^{rx} = \cos^2(\theta - \theta_x)\cos^2(\theta_y) \tag{3.29}$$

$$G_\theta^{rx} = \sin^2(\theta - \theta_x)\sin^2(\theta_y) \tag{3.30}$$

Similarly, the propagation channel transfer functions are give by:

$$\boldsymbol{F_r} = \frac{T^2}{\pi\sigma r^5} e^{-T}\sqrt{1+2T+2T^2}\, e^{j\{\tan^{-1}(\frac{T}{1+T})-T-\frac{\pi}{2}\}} \quad \text{and} \tag{3.31}$$

$$\boldsymbol{F_\theta} = \frac{T^2}{2\pi\sigma r^5} e^{-T}\sqrt{(1+T)^2+(T+2T^2)^2} \times e^{j\{\tan^{-1}(\frac{T+2T^2}{1+T})-T+\frac{\pi}{2}\}}. \tag{3.32}$$

In the equation $Z_{\text{IC}}(T)$, the linear distortion is included in $\boldsymbol{F}_r$ and $\boldsymbol{F}_\theta$, even the derivative operation carried out by the receiving loop antenna, which simplifies the process of separating the field contributions throughout the network

In addition, the transfer impedance for the homogeneous Half-Space (**HHS**) and Thin Sheet (**TS**) models can be described by the following equations:

$$Z(\mathcal{T}) = N_{tx}N_{rx}S_{tx}S_{rx}\left[\sqrt{G_z^{rx}}\boldsymbol{F_z} + \sqrt{G_\rho^{rx}}\boldsymbol{F}_\rho\right], \tag{3.33}$$

$$\boldsymbol{F}_z = \frac{\mathcal{T}^2}{\pi\sigma r^5} e^{-j\frac{\pi}{2}} \int_0^\infty \beta(x) J_0(Dx)dx, \tag{3.34}$$

$$\boldsymbol{F}_\rho\Big|_{up} = \frac{\mathcal{T}^2}{\pi\sigma r^5} e^{-j\frac{\pi}{2}} \int_0^\infty \beta(x) J_1(Dx)dx, \quad \text{and} \tag{3.35}$$

$$\boldsymbol{F}_\rho\Big|_{down} = \frac{\mathcal{T}^2}{\pi\sigma r^5} e^{-j\frac{\pi}{2}} \int_0^\infty \beta(x) J_1(Dx)\frac{(x^2+j2T^2)^{1/2}}{x}dx, \tag{3.36}$$

in which $G_z^{rx} = \cos^2(\theta_x)\cos^2(\theta_y)$ and $G_\rho^{rx} = \sin^2(\theta_x)\cos^2(\theta_y)$, being β described by equation (3.9) for the **HHS** model and by equation (3.10) for the **TS** model. This model considers part of the antenna normalized gain for estimating the interior channel transfer function and also has dependency on ρ, h, θ_x and θ_y.

Another important parameter that has to be considered is the ratio between the transmitted and received power as a function of the system parameters, which can be described by the following equations:

$$\frac{P_{rx}}{P_{tx}} = \frac{|Z(T)|^2}{R_{tx}R_{rx}}, \tag{3.37}$$

which gives:

$$\sqrt{P_{rx,\text{IC}}} = \sqrt{P_{tx}}\Phi_{tx}\Phi_{rx}\left|\sqrt{G_r^{tx}G_r^{rx}}\boldsymbol{F_r} + \sqrt{G_\theta^{tx}G_\theta^{rx}}\boldsymbol{F_\theta}\right|, \tag{3.38}$$

$$\sqrt{P_{rx,\text{HHS|TS}}} = \sqrt{P_{tx}}\Phi_{tx}\Phi_{rx}\left|\sqrt{G_z^{rx}}\boldsymbol{F_z} + \sqrt{G_\rho^{rx}}\boldsymbol{F_\rho}\right|, \tag{3.39}$$

in which Φ_{tx} and Φ_{rx} are the transmitting and receiving antennas specific apertures, respectively. The specific aperture of a loop antenna is a function of its radius a, mass, M, mass density, ρ_l, and, wire conductivity σ_l, and is given by:

$$\Phi = 0.5a\sqrt{M\sigma_l/\rho_l}. \tag{3.40}$$

In a similar way, the propagation loss for coaxial transmission can be expressed by:

$$L(\omega) = \frac{1}{\left|\boldsymbol{F}_z(\omega)\right|^2}. \tag{3.41}$$

3.4 ANTENNA MODELING FOR TTE COMMUNICATIONS

The antenna features, as type and size, depend on the characteristics of each site. For TTE communication antennas based on magnetic fields as loops are commonly used instead of electric dipoles or monopoles due to the fact of electric field suffers more attenuation while propagating in a conductive medium [4].

The uniqueness of each antenna introduces alteration on the magnetic moment. For instance, in systems using a single loop antenna to reach moderate distances (> 300 m), may need a conductor of tens of meters. On the contrary, for shorter distances, it is usual to use several turn loops, even though this increases the antenna's impedance when compared to a single turn antenna with the same conductor length. Additionally, these antennas must be connected to low noise amplifiers and noise coupling circuits to reduce the impact of atmospheric noise. Some loop antennas for specific use will be described in the following chapters.

In a similar way, there is another antenna type commonly used for TTE communication, as receiving instruments, that uses a ferrite rod as core of a helix antenna [4]. Specifically, it is built with a thin isolated conductive coil with several turns around a solid cylinder made of magnetic material whose magnetic permeability is several times higher than vacuum. The small cross section area is compensated with the high number of turns and the magnetic core, and that small dimension facilitates mobility in underground environments. These antennas usually present variable length from 10 cm up to 2 meters and present more sensibility to atmospheric noise, which make them less useful in above ground implementations. Figure 3.8 represents a ferrite rod antenna.

Figure 3.8: Ferrite rod antenna
Source: Souterweb [55]

It is interesting to compare antennas through magnetic moment capacity. On the one hand, a single turn loop antenna with 200 g of mass and 1 m of diameter produces a magnetic moment of $m_d = 30Am^2$ and dissipates a power of 10 W. On the other hand, a small ferrite rod with 1 cm of radius and 20 cm of length produces the same amount of magnetic moment, but dissipating twice as much power. Nevertheless, a 8.5 kg and 50 meters of diameter loop antenna can produce up to $m_d = 30kAm^2$ consuming 100 W, so depending on the project necessity, one could use a ferrite antenna or a loop antenna.

An important restriction for using ferrite antennas, as receiver in personal worn devices, is weight because a heavy receiver may cause health problems to the user; however, this type of receivers can be used in resistant equipment in the interior of a mine.

3.5 SOIL CONDUCTIVITY

Several conductivity estimation techniques can be found literature both from telecommunications and from geology. For this study, only two of those techniques are going to be used due to their easiness of application, the first utilizes electromagnetic measurements to estimate an apparent electrical conductivity, and the second one uses geophysical methods to estimate the electrical resistivity which can be inverted to calculate the apparent conductivity.

3.5.1 Soil conductivity from electromagnetic estimations.

Soil with high electric conductivity variation introduces difficulties to used the models presented above for estimating field intensity as a function of depth and frequency. This can be mitigated by the means of an apparent electric conductivity, which is a concept present in few studies of propagation in stratified soils in the underground mining context. Specifically, the consulted authors in [5, 4] transform a multi-layer medium into a single homogeneous layer by averaging the electric conductivity. Lincan proposed a weighted arithmetic mean described by:

$$\sigma_{equivalent} = \sum_{i=1}^{n-1} \frac{\sigma_i x_i}{x_t} + \frac{\sigma_i (x_t - \sum_{i=1}^{n-1} x_i)}{x_t} \tag{3.42}$$

in which σ_i and x_i are the electric conductivity and height of the i-th layer, x_t is total distance between surface and underground antenna.

Durkin in [42] and Lincan [5] used magnetic field measurement data to estimate the apparent conductivity using analytic models, with the intent to characterize the average behavior and conductivity variability.

Little [44] in 1980 carried out magnetic field measurements in 94 coal mines in the United States of America, which can be seen in Figure 3.9 for frequency of 630 Hz. Later, Durkin and Lincan processed the magnetic field data to estimate apparent electric conductivity; specifically, Durkin used the model **HHS** and Lincan complemented the study by comparing **HHS** and **TS** models for creating a new estimation model.

He named that model as **Q-factor**, and the process starts with the Q_{thin} estimation using a seed value for σ_0 and σ_a. Then the result is compared to the magnitude of $Q_{homogeneous}$ calculated from the **HHS** model, and the procedure is repeated for a new σd value until both sides of the equation coincide.

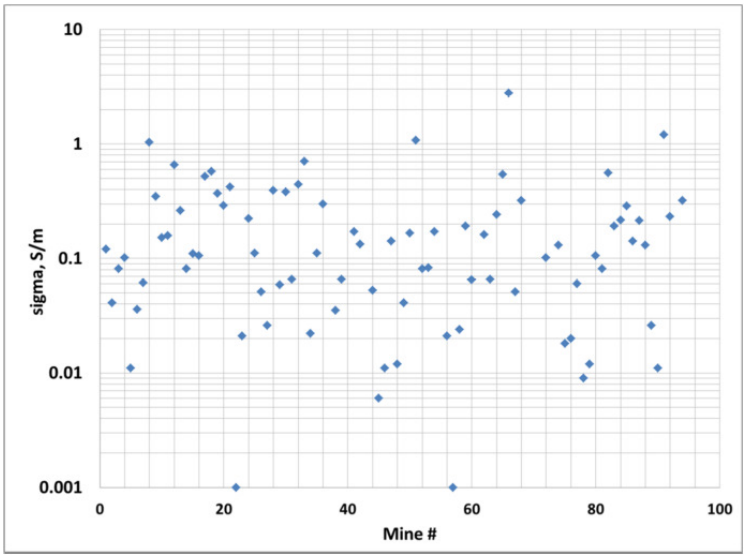

Figure 3.9: Equivalent conductivity for 94 real mines
Source: Lincan [5]

Lincan also used used a logarithmic regression to estimate an apparent conductivity σ_a for the real mine data through equation (3.43). This logarithmic behavior was determined after organizing the data shown in Fig. 3.9 and comparing with different probability distribution models. The author established that σ_a represents a random sample from a normal distribution with a mean that depends on frequency and depth, and a variance that is independent from both magnitudes. Working with that data, the author came up with the regression coefficients a, b and c presented

in Table 3.2.

$$\sigma_{apparent} = a + b * \log(freq) + c * \log(depth) \tag{3.43}$$

From this model it is noticeable that both frequency and depth coefficients have the same order, so the apparent electric conductivity depends on frequency.

Table 3.2: Logarithmic regression model for apparent conductivity (σ_a , S/m) as a function of $\log(depth, m)$ and $\log(frequency, Hz)$

Observations	a	b	c	Standard Error	R Square
238	2.1834	-0.2932	-0.5068	0.1479	0.4674

3.5.2 Soil conductivity from geophysical data.

Among the geophysical techniques to identify soil electrical resistivity is the electroresistivity method, which uses superficial induced currents that penetrate soil and generate a voltage difference between two measurement points. Afterwards, the soil resistivity is estimated as the ratio between the voltage generated and the induced current [56]

4 APPARENT ELECTRIC CONDUCTIVITY, PROPAGATION LOSS AND MAGNETIC FIELD ATTENUATION STATISTICAL MODEL

The apparent electric conductivity is a useful mechanism to simplify complex calculations in difficult underground environments, because it enables the transformation of a multiple conductivity soil into a single σ equivalent soil. Some studies, mentioned by Lincan in [5], consider a variation of apparent conductivity that is inversely proportional to depth due to the presence of metal tubing and other metallic structures in interior of soil in underground mines. Nevertheless, this study does not consider this hypothesis in order to provide a broader database.

So that, this chapter presents a statistical characterization of the apparent electric conductivity and magnetic field attenuation in underground coal mines, specifically for transmission at the optimal frequency for which a model is also proposed. This model might be convenient to establish operation limits in TTE systems taking into consideration the propagation loss variation, whose impact is less prominent in the optimal frequency. This empirical model uses data from electromagnetic simulations built with the finite element method (FEM) [57], which in turn, are based on real measurement data from coal mines obtained by Little in [44].

4.1 EQUIVALENT CONDUCTIVITY DATABASE GENERATION

The simulation campaign was projected to use the Monte Carlo method with 150 different scenarios in which only the transmitting and receiving antennas stayed at the same position and the propagation medium had several horizontal layers with different electric conductivities and heights. Specifically, the conductivity of each layer in each Monte Carlo trial was set using the statistical distribution estimated from the measurements in [44], due to the fact of being the most complete database on H-field measurements in underground TTE communication that can be found in the literature so far. Those measurements represent, in their majority, down-link data which was used to build a apparent conductivity database for frequencies of 630, 1050, 1950 and 3030 Hz by using the **HHS** model. That gross intensity magnetic field data was normalized by the magnetic moment used in each original measurement as in equation (3.4). Additionally, this data had to be adapted to the international measurement system to carry out that normalization.

After analyzing the results through a data fit comparison for several distributions using three tests, Root Mean Square Error (RMSE), Kolmogorov-Smirnov, and Cramer-Von Mises, it was observed that Log-normal was the most suitable distribution to represent the measured equivalent conductivity, with parameters μ_{lg} = -3.8 and σ_{lg} = 1.2. These values were estimated using the distribution parameters for each frequency (630, 1050, 1950 and 3030 Hz), and by employing

a cubic spline interpolation, and subsequent extrapolation with a 3rd degree polynomial. Figure 4.1 shows the distribution of all apparent conductivity estimated for all mines, for all frequencies and depth, without any particular order. Nevertheless, when this data is rearranged to be fit into a probability distribution, it shows the logarithmic behavior as stated before.

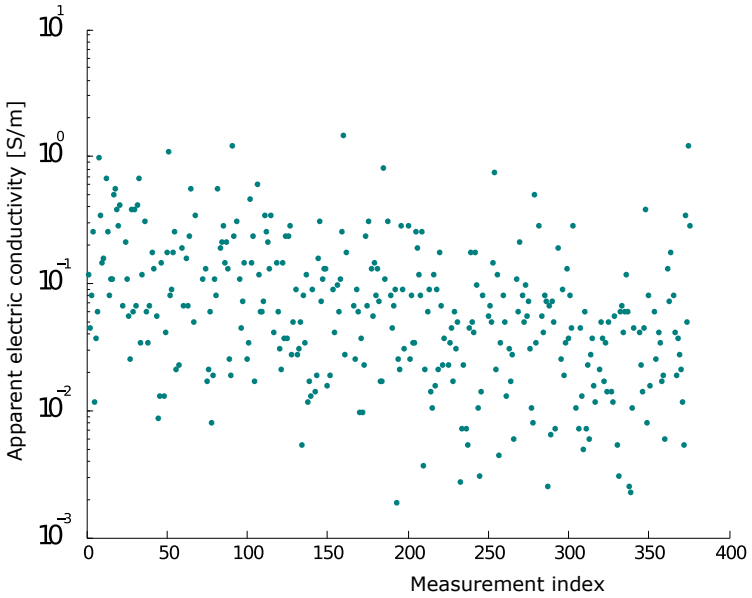

Figure 4.1: Apparent conductivity normalized by magnetic moment at each frequency and depth.

4.2 SIMULATION PARAMETERS

Complex environments are commonly difficult to be analytically described by mathematical equations, so computational simulation becomes a suitable option to emulate diverse scenarios and generate a database for statistical analysis. Works as this and the one presented by Abbas in [58] use real measurement data to feed the simulation campaign in order to provide more accurate models. However, there are very few reports or papers on electromagnetic simulations in TTE communications [59, 5, 2]. Durkin in [59] recommended the finite element method for TTE simulations, thus it is employed in this study with the use the commercial software CST Studio Suite ®. To emulate soil variability, the ground was modeled as homogeneous layers with random physical characteristics. Still, random variables were used to describe the number of layers, their height and their conductivity.

To guarantee the variation of each scenario, an algorithm was implemented, shown in Fig. 4.2, that uses an electromagnetic simulation software to build the physical structures and calculate the H-field intensity throughout the down-link transmitting antenna axis. The Monte Carlo method is employed through a supporting VBA macro that generates all random values, sets the geometrical structures along with their soil electromagnetic characteristics, sets each trial boundary conditions, and restarts the simulation software.

With the parameters estimated in Section 4.1, a set of trials was created to study the H-field

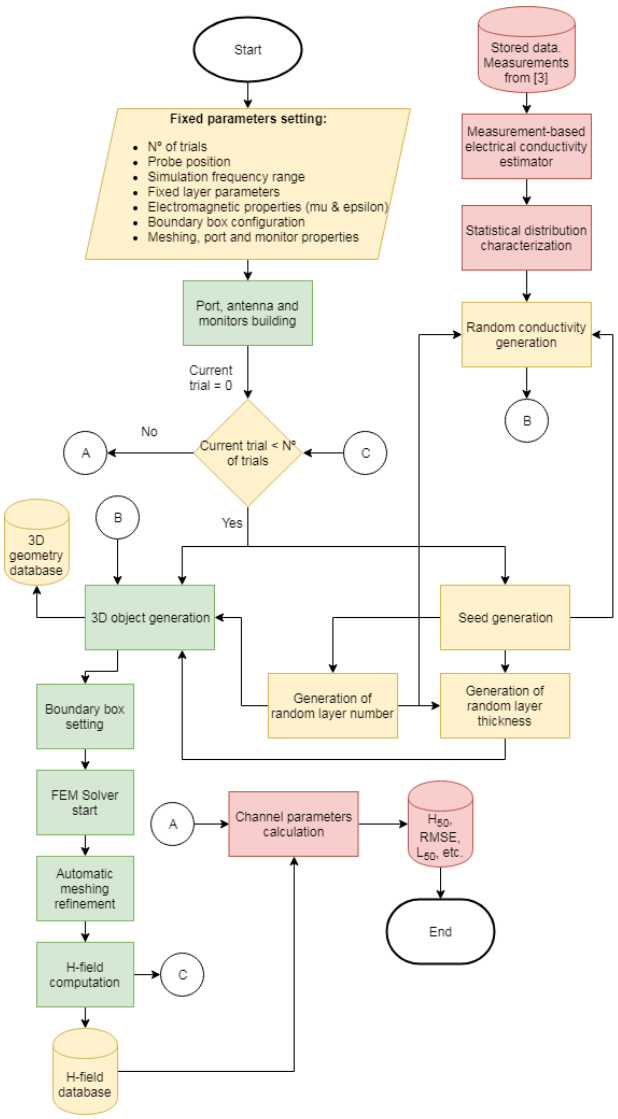

Figure 4.2: Simulation process algorithm where the red boxes are MATLAB routines, the orange boxes are VBA routines, and the green boxes are CST routines.

behavior in scenarios that mimic real-world conditions. The scenario used for this simulation is described as follows and shown in Fig. 4.3.

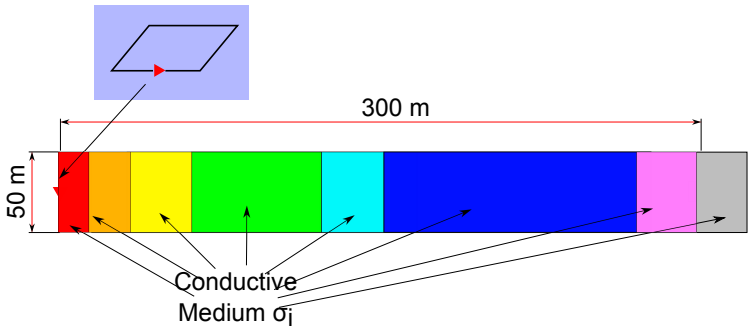

Figure 4.3: Multi-layer TTE scenario for simulations using FEM method.

In detail, the transmitting antenna is a one-turn square loop with $\sqrt{\pi}$ m sides. Such size is

small enough to approximate a punctual antenna with constant electric current. It is located 50 cm above the ground and surrounded by air. Magnetic field probes are placed underground to measure the H-field. They are evenly distributed along the loop axis with a step of 10 m, in order to obtain a smooth variation of field.

Horizontal layers are modeled in such a way so as to represent the sedimentary sequences of rocks found in coal mines [60]. They are modeled by square-base parallelepipeds with 50 m sides, whose large width was considered to avoid boundary problems for conductive media and determined after simulation tests. Their heights were uniformly distributed from 1 to 300 m, and the sum of all heights was limited to 300 m. Such a large span of heights tries to factor in contributions from more stratified profiles along with those of lesser stratification. The latter configuration was considered since the conductivity values used in the simulations were based on the **HSS** model. A random number of rock layers was selected from a uniform distribution, with a minimum of 3 and maximum of 25 layers for each trial. The lack of studies about sedimentary structures in coal mines made us choose the uniform distribution, which is the simplest arrangement for the layer profile.

Regarding the electromagnetic characteristics of soil, the magnetic permeability was set as vacuum condition $\mu_0 = 4\pi 10^{-7}$[H/m], which is common in the overburden of coal mines. Electric conductivity was programmed to be a random variable with log-normal distribution according to the extrapolated parameters given in the last section by $\mu_{lg} = -3.8$ and $\sigma_{lg} = 1.2$. None of the structure parameters was tuned to achieve any expected result.

Using a FEM solver with tetrahedral meshing and absorptive boundary walls, 150 independent and random trials were carried out resulting in more than 200 thousand measurements of field intensity. Such quantity was selected to surpass the number of scenarios considered in [44] (94 mines) and used in [42] and [5] to achieve their models. In fact, not many trials are necessary to achieve acceptable coefficients for equation (4.1), shown later, that fits well to the median of measured data in [44]. The model in (4.1) and its coefficients computed using 150 trials attained a RMSE of 3.7 dB, and when any combination of only 10 trials was randomly chosen, the RMSE was always below 5 dB. However, when fewer trials are used to generate the coefficients, the discreet CDF of propagation loss might be compromised.

Since the optimum frequency in TTE transmission is usually below 10 kHz for moderate and great depths, the frequency span was set to vary uniformly in logarithmic steps from 0.1 to 10 kHz, and the H-field was normalized according to (3.4).

For each trial, a different seed was generated, by CST ®, to guarantee the randomness of each scenario. The post-processing data analysis was realized by the use of MATLAB ®.

4.3 REGRESSION MODEL FOR THE PROPAGATION LOSS

Using the H-field data from simulations and equation (3.41) a propagation loss database was generated, which in turn, was used to estimate the median as a function of frequency *f* and depth *h* and then it was fitted to the following equation:

$$L_{50}(h,f) = 20[a_1 + a_2 \times \log(\omega) + a_3 \times \log(h) + a_4 \times \log(e^{-\tilde{T}})] \ \text{[dB]}, \tag{4.1}$$

in which $\omega = 2\pi f$, $\tilde{T} = h\sqrt{\frac{\omega\mu\tilde{\sigma}}{2}}$, $\mu = \mu_0$. $\tilde{\sigma} = e^{-3.8} = 0.022$ is the equivalent value of median conductivity used in all simulations based on measurements from [44], and a_1, a_2, a_3, a_4 are given in Table 4.1. This equation, when converted to linear scale, becomes a multiplication of terms as follows:

$$L_{50}(f,h) = 10^{a_1}\omega^{a_2}h^{a_3}e^{-a_4\tilde{T}}. \tag{4.2}$$

As the majority of propagation models are based on multiplication of terms raised to some power [61, 62], this study follows this trend. Specifically, the term $e^{-\tilde{T}}$ represents the skin depth impact on the attenuation and a_1 adjusts its offset on decibel scale.

For the coefficients presented in Table 4.1, the fitting has a coefficient of determination (R-squared) of 0.998 and a root mean square error (RMSE) of 1.144 dB. Other less complex equations of lower order are easily computed bringing simplicity to the model at the cost of increasing the RMSE. For example, excluding the term associated with a_4, the RMS error increases to 8 dB and R-squared drops from 0.988 to 0.91.

Table 4.1: Propagation loss model coefficients.

Coefficient	Value
a_1	8.7348
a_2	-1.222
a_3	2.316
a_4	-1.115

To compare this model to the measured and synthetic data, Fig. 4.4 shows the median of propagation loss calculated from (4.1) and computed from data in [44] only for the four frequencies employed in the measurements and the simulated data median. Fig. 4.4 also shows the simulation trial data density expressed as a function of the number of trials per dB per kHz, and comprehends curves from the deterministic models **HHS** and **IC** as a reference that use the apparent conductivity of 0.022 S/m.

Observing the curves, it can be noted that for shallow depths there is a quasi linear dependency of attenuation as a function of frequency, because the observation point is in a quasi-static zone with respect to the transmitting antenna, while larger attenuation for higher frequencies is

observed for medium and greater depths. The RMSE error between (4.1) and the median of measured loss is 3.7 dB, and the R-squared is 0.98, considering the four frequencies for all depths. It was not necessary to adapt or adjust parameters of any specific layer to achieve such results. Thus, it is possible to suggest that the simulated model is valid, including the choice of layer and conductivity distributions and their parameters.

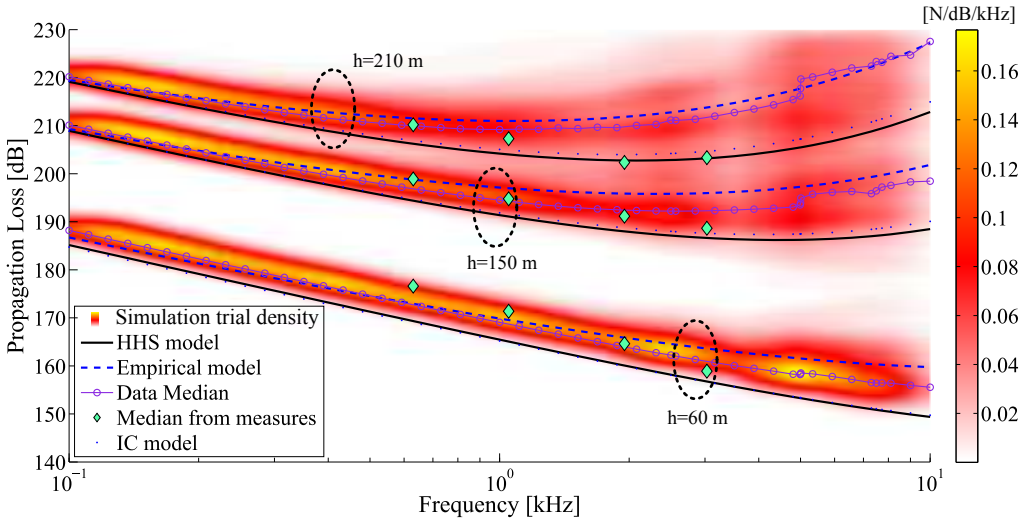

Figure 4.4: Comparison of different models and propagation loss measurements for depths of 150, 220 and 300 meters.

Additionally in Fig. 4.4, the deterministic models **HHS** and **IC** for $\sigma = \tilde{\sigma}$ are more optimistic when compared to the median of simulated data and the empirical model. This means that multi-layer scenarios provide an extra loss for higher frequencies compared to models with one or two layers, even when the median conductivity of the multiple layers equals the conductivity of the homogeneous overburden. Such behavior, suggesting that there will be higher losses at higher frequencies for models with more layers, is observed in [5] and confirmed here with a different multi-layer method.

4.4 REGRESSION MODEL FOR THE APPARENT CONDUCTIVITY

The apparent conductivity estimated through the simulated H-Field using the **HHS** model is computed as in [42, 43, 6]. Field curves are computed from the integrals in (3.8) for a variety of conductivity values. Such curves are used as reference maps to select the most adequate apparent conductivity and must consider the field intensity, depth, and operating frequency.

Durkin proposed a regression model in [42] where the log of the apparent conductivity is linearly related to frequency and depth. He selected measurements from only 26 coal mines and neglected depths less than 100 meters. Also, Yan in [43] proposed a linear regression model for the apparent conductivity, neglecting depths shallower than 50 meters. He also used specific rules to select some data from among all measurements to fit his model.

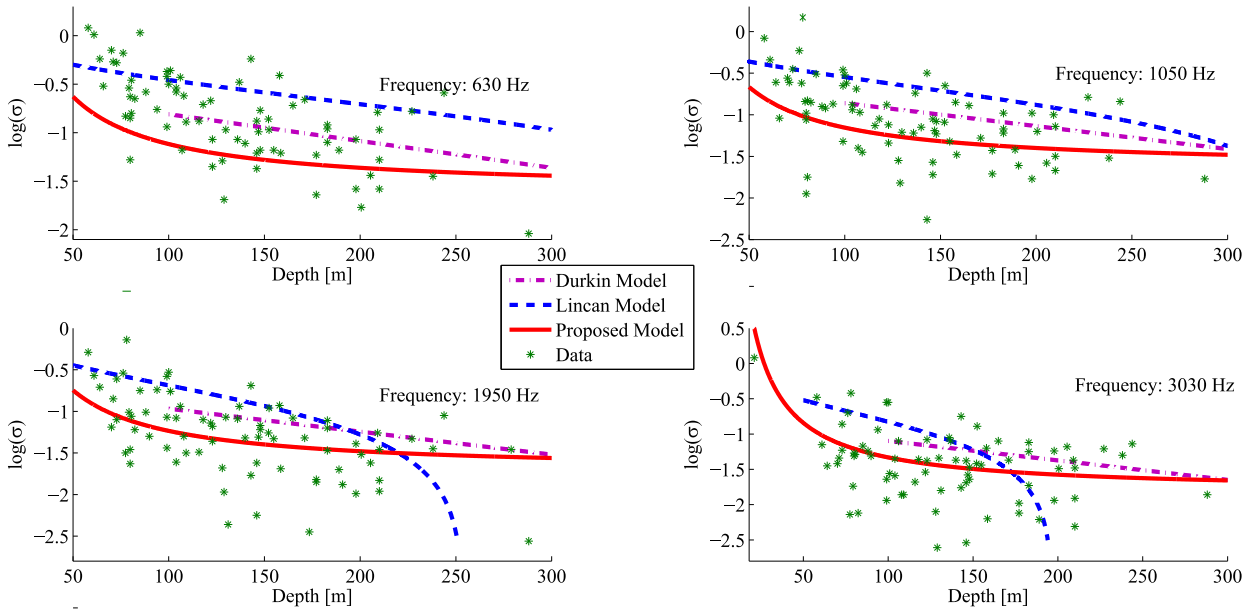

Figure 4.5: Comparison of apparent conductivity models as function of depth and frequency.

In this section is proposed a model for estimating the apparent conductivity fitted through the simulated data and not by using the measurements or part of them. Differently from the linear model in [42], the term associated to depth is inversely proportional to conductivity. The models from Durkin, Yan, and the one proposed here are respectively given as follows:

$$\log \sigma_{50}(h, f)_{\text{Durkin}} = \alpha + \beta_1 f + \beta_2 h \tag{4.3}$$

$$\log \sigma_{50}(h, f)_{\text{Yan}} = \log(a + b\log(f) + c\log(h)) \tag{4.4}$$

$$\log \sigma_{50}(h, f)_{\text{Proposed}} = b_1 + 2\pi b_2 f + b_3/h, \tag{4.5}$$

in which the coefficients for the best fit to the median of simulated data are given in Table 4.2.

The three models were fitted using different methodologies; particularly, the proposed model is based on an empirical analysis of the data, which showed a better fit with an inverse behavior of depth h Although none of the models used all measurements to carry out the fitting, it seems fair to compare them in view of all data for the four frequencies (630, 1050, 1950 and 3030 Hz), as may be seen in Fig. 4.5. Table 4.3 presents the RMS error in $\log(\mathrm{S/m})$ and the R^2 for all models. The proposed model presented adequate statistics for the first two frequencies, with the best fitting for the last two. The greater error for 630 Hz was due to the fitting being performed for up to 10 kHz, but was limited to 3030 Hz for the other two models.

It is possible to confirm through modeled and measured data that higher apparent conductivity was found closer to the surface. However, statements in [43], claiming that this may be due to the presence of metal structures such as cables, pipes, cased bore holes, etc. as well as the presence of more dissolved salt and mineral substances, may possibly be mistaken. This is demonstrated by

Table 4.2: Comparison of different model coefficients for apparent conductivity.

	Durkin Model ($\log \sigma$)	**Yan Model** (σ)	**Proposed Model** ($\log \sigma$)
Intercept	α = -0.45818	a = 2.1834	b_1 = -1.55
Frequency coeff.	β_1 = -0.00012	b = -0.2932	b_2 = -1.421e^{-5}
Depth coeff.	β_2 = -0.00276	c = -0.5068	b_3 = 48.91

Table 4.3: Comparison of RMS error of different conductivity models.

Frequency [Hz]	**Durkin Model** (RMSE)	**Yan Model** (RMSE)	**Proposed Model** (RMSE)
630	0.3683	0.4893	0.4767
1050	0.4053	0.5936	0.4059
1950	0.4705	0.5715	0.4288
3030	0.5098	0.6411	0.4510

the simulations carried out in this study, which did not employ any high conductive layer close to the surface, nevertheless showed that there were higher equivalent conductivities even for shallow depths.

4.5 CHANNEL VARIABILITY AT OPTIMAL FREQUENCY

Given that the channel transfer function has band-pass filter behavior, it is possible to seek the optimal frequency with the lowest propagation loss. From (4.1), the derivative of the empirical model of propagation loss is given by:

$$\frac{\mathrm{d}}{\mathrm{d}\omega} L_{50}(h,\omega) = 20\left[a_2 \log(e)\frac{1}{\omega} - a_4 T \log(e)\frac{1}{2\sqrt{\omega}}\right], \tag{4.6}$$

and equating (4.6) to zero, the median of optimal frequency as a function of depth in Hz can be calculated via:

$$f_{opt\_50}(h) = \frac{8(a_2)^2}{2\pi(a_4)^2 h^2 \mu\tilde{\sigma}}. \tag{4.7}$$

The median behaviour of the channel may or may not answer the questions related to the operating limits of a TTE system. Despite the utility of (4.7), the optimal transmission frequency in a coal mine may vary from a few hundred Hertz for great depths (h > 400 m) to hundreds of kHz for shallow depths (h < 30 m). The cumulative distribution function (CDF) is used to

explain this variation of the optimal frequency and also to calculate the propagation loss for the worst-case propagation channel.

If the optimal frequency F_{opt} is a random variable with possible value f_{opt}^i, and the probability of occurrence of i is given by $p_i = Pr[F_{opt} = f_{opt}^i] = p(f_{opt}^i)$, the discrete CDF of F_{opt} can be given by:

$$\begin{aligned} F(f_{opt}) &= Pr[F_{opt} \leq f_{opt}] \\ &= \sum_{f_{opt}^i \leq f_{opt}} p(f_{opt}^i). \end{aligned} \tag{4.8}$$

Fig. 4.6 presents the CDF of the optimal frequency for depths of 150, 220 and 300 meters considering the simulated data. The f_{opt} for 50% and 95% are indicated along with the median values from the empirical model (4.7) in round brackets. Although distances between 20 and 300 meters were used in the simulation parameters, it is more complicated to analyze the variability of the optimal frequency for shallow depths. The estimation of the optimal frequency for all trials can exponentially increase the number of frequencies to be tested in the simulation with increases in depth. The choice for depths between 150 and 300 meters seems reasonable in terms of processing cost and representativeness of the most important scenarios for frequencies up to 10 kHz. This is because at a depth of 150 meters almost all the optimal frequencies lie between 500 Hz and 10 kHz. For depths greater than 300 meters, the optimal frequency is confined to frequencies of 2 kHz or below.

Fig. 4.7 tries to provide a different perspective of the channel variability. The propagation loss samples for all simulation trials and measurements are plotted with blue markers as a function of depth, separately for each of the four frequencies (630, 1050, 1950 and 3030 Hz). For some of these trials, the optimal frequency is also one of these four frequencies. When this occurs, the trial is shown with green markers.

Firstly, a larger propagation loss variability can be observed for higher frequencies and depths. This is because a heterogeneous environment causes more channel variability for smaller wavelengths. Also, the larger number of independent layers for greater depths contributes to field strength variation. This is not necessarily true when considering only samples at the optimal frequency. A higher concentration of samples is observed around 300 meters for the optimal frequency of 630 Hz. However, with increases in the optimal frequency, the samples become less concentrated with regard to depth. In a certain way, that behavior is similar to the one in Fig. 4.6, where there is less concentration of optimal samples in frequency domain for shallower depths. The bandpass channel behaviour in which bandwidth decreases with depths and increases with frequency is present in deterministic models [4], and confirmed here for multilayer simulations.

If the depths with the highest occurrence of each frequency are chosen, it is obtained the following: 300 meters for 630 Hz, 250 meters for 1050 Hz, 180 meters for 1950 Hz, and 140

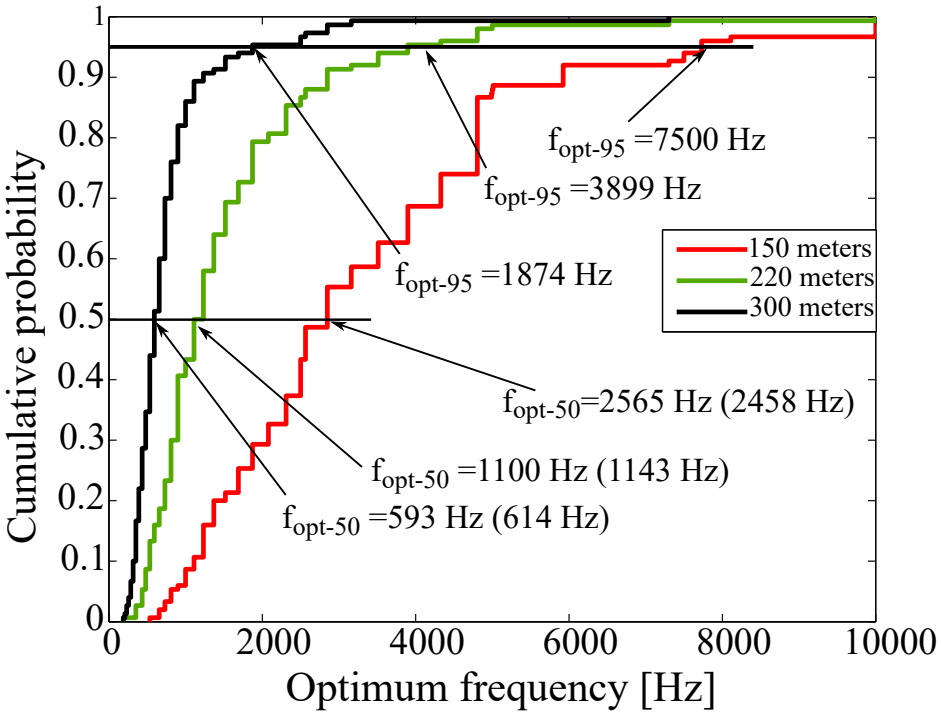

Figure 4.6: CDF of optimal frequency for depths of 150, 220 and 300 meters.

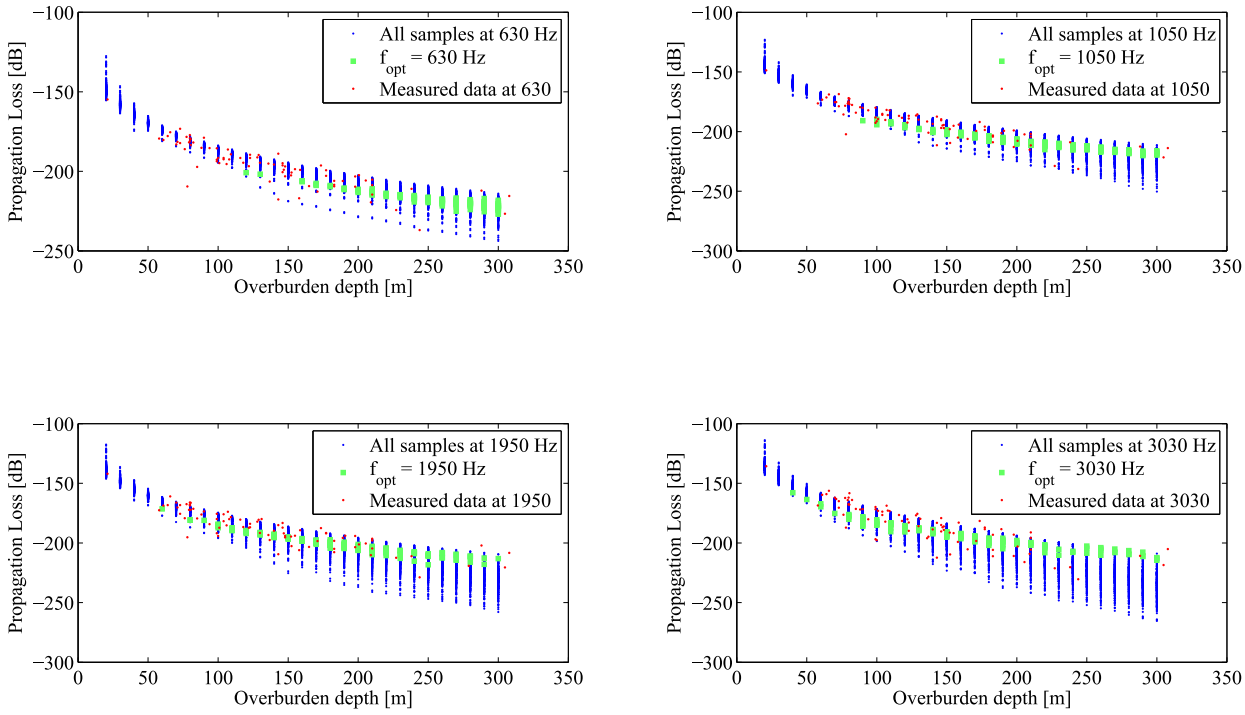

Figure 4.7: Propagation loss variability in an optimal frequency scenario compared to non-optimal frequency scenarios.

meters for 3030 Hz. Table 4.4 compares the channel variability at these depth/frequency pairs considering all samples and only optimal samples, through the prediction interval of 90%, i.e. the maximum additional loss between the 5% best scenarios and the scenario with 95% of cu-

Table 4.4: Reference interval of 90 % of propagation loss samples.

	Measurement-based model [44]	**All samples**	**Samples at the optimal frequency**
630 Hz / 300 m	21.5 dB	16.5 dB	6.5 dB
1050 Hz / 250 m	21.5 dB	19 dB	4.5 dB
1950 Hz / 180 m	23.5 dB	20 dB	4 dB
3030 Hz / 140 m	29 dB	22.5 dB	5 dB

mulative probability. Using all measurement data, Little [44] proposed a normal distribution of field intensity (in dB) dividing depth into sectors of 76 meters. The prediction interval using this model is also presented in Table 4.4. We observe that, at least for those frequencies and depths, the prediction interval differs from 2.5 to 6.5 dB between the simulations (all samples) and the measurements-based model, and that the channel variability is substantially smaller when considering only samples at the optimal frequency. This type of analysis, that considers the optimal frequencies, is important because, in some cases, transmission is only possible using those frequencies.

5 ANTENNAS FOR TTE COMMUNICATION

In the context of Through-The-Earth communication, magnetic antennas are the most efficient instruments to overcome the difficult medium of conductive soil. Another fact of these systems is that they use low frequencies to overcome the attenuation inside the underground environment which in turn implies the use of big radiant antennas to guarantee high radiation efficiency. For instance, a half-wave dipole at $150\ kHz$ would be 950.98 m long, which would be extremely useless for portable applications.

One solution for this situation is to use smaller antennas at low frequencies, even if this makes them less efficient in terms of radiation, because for short distances, i.e. near field, the coupling for magnetic dipole antennas is inductive and for electric dipoles is electrostatic. Reducing the antenna size alters the resonance frequency and its impedance, so it is necessary to use a coupling circuit to change the resonance to the needed frequency.

As a general fact presented by Gibson in [4], electrostatic sources produce electric fields that cannot penetrate a conductive medium, on the contrary, magnetic fields from magnetostatic sources can easily pass through a conductor. Moreover, electric fields generated at low frequencies suffer more attenuation while propagating in a conductive medium than their magnetic counterpart. Regarding time varying sources, electric component of electromagnetic fields induces Eddy currents in the interior of a conductive medium while the magnetic part might propagate in the interior up to hundred of meters depending on the frequency used.

On the point of view of speleology and mining, it is necessary that the equipment used is portable, easy to deploy and lightweight, so inductive loop antennas are a suitable option. In this chapter different types of magnetic loop antennas for TTE communication are presented, specifying their physical characteristics and their operation range.

SPECIFIC APERTURE

It is defined as the ratio between the provided power and the generated magnetic moment. This concept provides useful results to project a magnetic induction antenna: the number of antenna turns does not impact its performance; the antenna's Q factor is not expressed as a function of number of turns, and the field intensity is affected by other external parameters.

SKIN DEPTH EFFECT ON CONDUCTORS FOR TTE COMMUNICATION

As stated in the previous chapters, when the electric field enters a conductive medium it decays with an exponential rate and this fact is called skin depth effect. In the case of a wide conductive wire, the current passing through it stays in the surface up to a distance of one skin depth (δ). As the example in [4], a $2\ mm$ wide copper wire would have a $0.2\ mm$ skin depth at 100 kHz which augments the wire resistance to 2.5 times it DC resistance.

This effect considers that the current flux in the cable core opposes the Eddy currents induced by the field created from the current itself. In similar way, parallel wires conducting current in the same direction would create a proximity repulsion effect to each other, and, in twisted wires, the current would tend to be closer to the surface of the whole group of cables.

Thus, the distance between conductive wires becomes an important parameter to include in the project of an antenna, and was studied by several authors [63, 64, 65, 66, 67, 68, 69]; however, non of them considers losses related to self capacitance, which is the effect created by a segment of wire over another due to their small separation distance.

5.1 ANTENNA PARAMETERS

In this study, the designed antennas should keep their shape to be more easily transported, so the best way to guarantee more structural resistance was to wind the wires tightly around a non-conductive structure, which creates losses due to the self capacitance effect.

As this effect is unavoidable, it has to be included in the design as a parasitic capacitance in parallel to the antenna resistance and inductance as shown in Figure 5.1

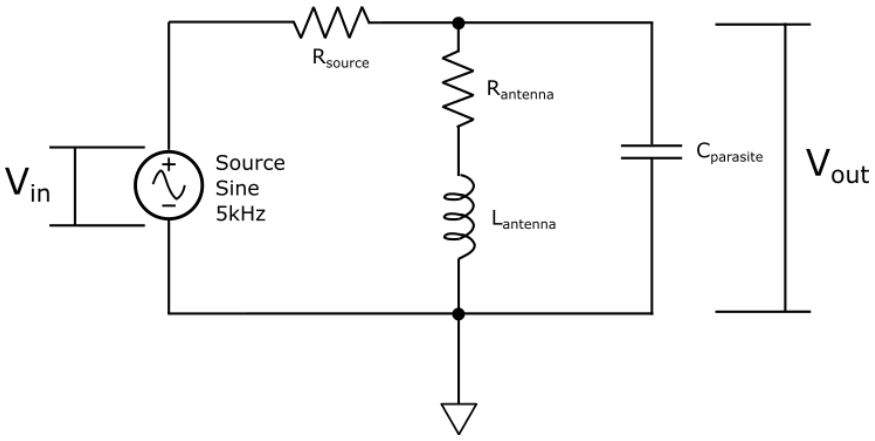

Figure 5.1: Loop antenna schematic model showing the self capacitance effect.

Then, the transfer function considers: $R_{source} = R_s$, $R_{antenna} = R_a$, $C_{parasitic} = C_p$ e $L_{antenna} = L_a$, and is described in the Laplace domain by:

$$H(s) = \frac{V_{out}(s)}{V_{in}(s)} = \frac{1}{R_s C_p} \frac{s + R_a/L_a}{s^2 + (\frac{(L_a + C_p R_a R_s)s}{C_p L_a R_s}) + (\frac{R_a + R_s}{C_p L_a R_s})}. \tag{5.1}$$

As the transient response is the one needed for this study, the denominator from equation (5.1)

$$d(s) = s^2 + \frac{(L_a + C_p R_a R_s)s}{C_p L_a R_s} + \frac{R_a + R_s}{C_p L_a R_s}. \tag{5.2}$$

Then $d(s)$ expressed in the form $s^2 + 2\alpha s + w_o^2 = 0$, being $2\alpha = \Delta w$ (Antenna bandwidth), gives:

$$\alpha = \frac{(L_a + C_p R_a R_s)}{2 C_p L_a R_s} \quad e \quad w_0 = \sqrt{\frac{R_a + R_s}{C_p L_a R_s}}, \tag{5.3}$$

this formulation considers the source resistance R_s as part of the bandwidth and resonance frequency impacting directly the estimations of R_a and C_p. Additionally, w_0 is defined as the antenna resonance angular frequency.

If a high series resistance is connected to the source, i.e. $R_s \longrightarrow \infty$, gives:

$$d(s) \approx s^2 + \frac{R_a}{L_a} s + \frac{1}{C_p L_a}, \tag{5.4}$$

so $\alpha = R_a/2L_a$ and $w_0 = 1/\sqrt{C_p L_a}$, and finding the L_a value by the use of a LCR meter, R_a and C_p can be found through the transient response.

The circuit poles are $s = -\alpha_-^+ \sqrt{\alpha^2 - w_0^2}$, as the underdamped response occurs when the poles are negative, is given:

$$S_1 = -\alpha + j\sqrt{\alpha^2 - w_0^2} = -\alpha + j w_0 \sqrt{1 - \zeta^2}, \tag{5.5}$$

$$S_2 = -\alpha - j\sqrt{\alpha^2 - w_0^2} = -\alpha - j w_0 \sqrt{1 - \zeta^2}, \tag{5.6}$$

in which $\zeta = \frac{\alpha}{w_0} = \frac{1}{2Q}$. Then, the transient signal can be found via Laplace transform.

$$v(t) = A_1 e^{S_1 t} + A_2 e^{S_2 t}, \tag{5.7}$$

which gives:

$$v(t) \approx 2Ae^{-\alpha t} cos(w_0 t) + \varphi, \tag{5.8}$$

then the parasitic capacitance C_p is estimated with L_a, oscillation period measurements in the oscilloscope and w_0 equation. Similarly, R_a is estimated using (5.4) and measuring the exponential decay $e^{-\alpha t}$, which is calculated by:

$$\Delta w = 2\alpha, \tag{5.9}$$

$$\Delta f = \frac{\alpha}{\pi} = \frac{R_a}{2\pi L_a}, \tag{5.10}$$

considering $T_{50\%}$ as the time when $e^{-\alpha t}$ reduces by 50% from its value at $t = 0$

$$t = 0 \Rightarrow e^{-\alpha 0} = 1 \tag{5.11}$$

$$t = T_{50\%} \Rightarrow \frac{1}{2} = e^{-\alpha T_{50\%}} \Rightarrow -\pi \Delta f T_{50\%} = \ln 0.5 \tag{5.12}$$

$$\Delta f \approx \frac{1}{4,5T_{50\%}} \approx \frac{f_0}{4,5N} \qquad \alpha \approx \frac{0,7}{T_{50\%}} \approx \frac{0,7F_0}{N} \tag{5.13}$$

being N the cycle number and F_0 the natural resonance frequency. This gives:

$$Q \approx \frac{f_0}{\Delta f} \approx 4.5N, \tag{5.14}$$

and the antenna resistance is:

$$R_a = \frac{1.4 f_0 L}{N} \approx 4.5N. \tag{5.15}$$

It is noticeable that the antenna resistance changes along with the frequency in virtue of the parasitic resistance R_p. Then, the parasitic capacitance at the required frequency ω_i might be estimated with:

$$C_p = \frac{1}{L_a \omega_0^2}, \tag{5.16}$$

making $C_{total} = C_p + C_{correction}$:

$$C_p + C_{correction} = \frac{1}{L_a \omega_i^2} \Rightarrow C_{correction} = \frac{1}{L_a \omega_i^2} - \frac{1}{L_a \omega_0^2} \tag{5.17}$$

$$C_{correction} = \frac{1}{L_a} \frac{\omega_0^2 - \omega_i^2}{(\omega_0 \omega_i)^2} \tag{5.18}$$

In order to obtain a positive capacitance, ω_0 must be higher than ω_i, which limits the maximum correction capacitance to the natural resonance frequency.

5.2 TRANSMISSION FEEDING

As the magnetic moment is the most important parameter for transmission with these antennas, the use of an equipment similar to a current source is recommended. The most suitable gadget available is the power amplifier because the output current can be estimated from the output voltage and, for some equipment, the current can be directly measured.

In practical situations, it is possible to use tuned and untuned antennas. For the first case, to feed a tuned antenna the tuning capacitor must be connected in series with the transmission antenna to provide a mostly resistive load seen from the power amplifier. For the second case, the antenna is fed directly from the amplifier so the feeding voltage must be augmented as the frequency augments to guarantee the same current level in the antenna.

5.2.1 Power Amplifiers used for transmission

For preliminary tests both in the laboratory and in outdoors, a robust power amplifier was used. This equipment was an Accel Instruments **TS 250** with output voltage limit of 20 V peak and output current of 3 A as shown in Figure 5.2.

Figure 5.2: Power amplifier used for transmission on some tests.

Afterwards, the electronic team of the project designed a portable power amplifier to simplify outdoor measurements and from now on will be referred as **integrated Power Amplifier (PA)**. They developed the circuit that accomplished the specifications on Table 5.1, resulting on the schematics on Figure 5.3 and the final product is shown in Figure 5.4. Details related to the

construction of this circuit are going to be presented on an upcoming joint article to be published in 2021 by author and other members of the research project.

Table 5.1: Integrated PA Project specifications.

Parameter	**Value**
R_L	14,791 Ω
Desired Output Power	3 W
I_{out}	500 mA(rms)
Frequency range	20 Hz to 10 kHz

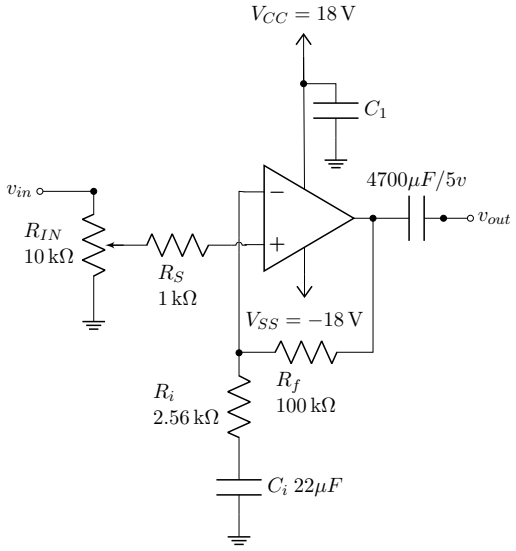

Figure 5.3: Overall structure of the Integrated PA.

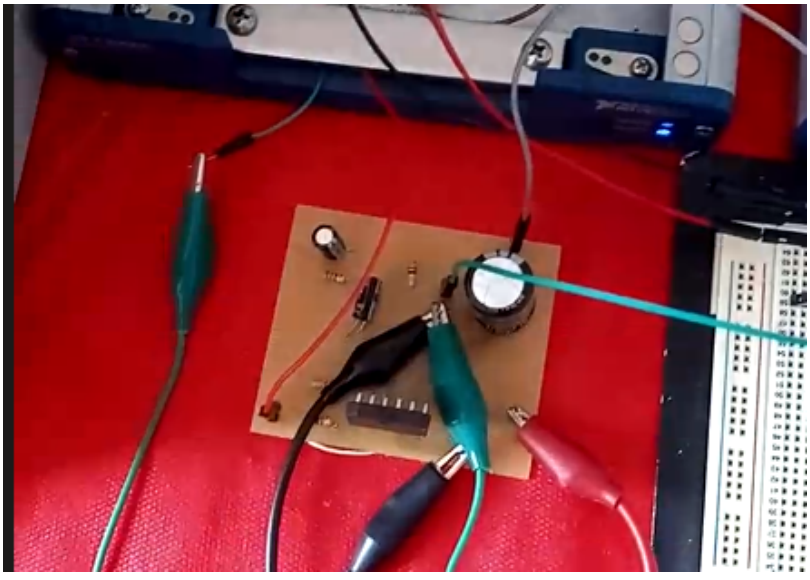

Figure 5.4: Power amplifier designed and build by the electronic team used for transmission on some tests.

5.3 DESIGNED ANTENNAS

In order to accomplish the necessity of antennas for short distances and with a important scale of portability, several antennas were designed, built and characterized. In this section five antennas are outlined.

5.3.1 Square antenna # 1

Figure 5.5 presents the square antenna made of a single copper wire AWG 11 winded around a wooden 186 cm branch x-shape support.

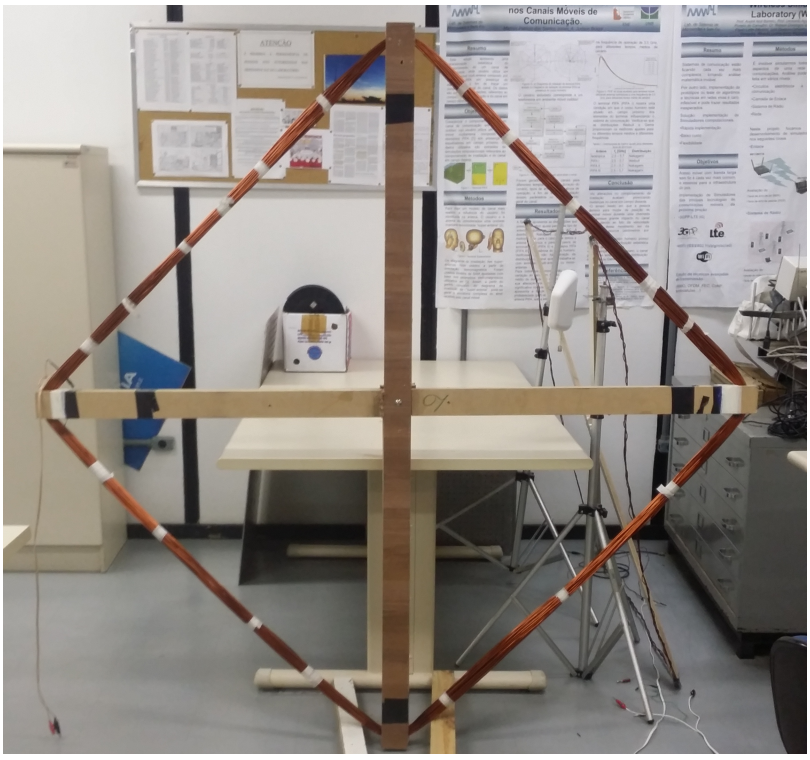

Figure 5.5: Square antenna for TTE communication with 12 Kg of AWG 11 copper and transverse area of 1.72 m^2

This antenna became the flagship of this study because of its reception capability based on its larger copper mass compared to other antennas. It was used for noise measurements and as reception antenna in almost all tests. As the available power amplifier had current limitations, this antenna could not be used to its full potential.

Additionally, a parasitic resistance analysis was carried out to verify its variation as a function of frequency and its shown in Figure 5.6.

5.3.2 Square antenna # 2

This antenna was designed to be the transmission antenna in several experiments as the one in section 6.3.3. In order to provide symmetry, its dimensions are the same as the square antenna #

Table 5.2: Parameter characterization for square antenna # 1

Characteristics	
Shape	Square
Side	131 cm
Number of turns	63
Wire diameter	2.305 mm
Area	1.72 m^2
DC Resistance - Theoretical	1.36 Ω
DC Resistance - Experimental	1.54 Ω
Inductance- Theoretical	17.1 mH
Inductance - Experimental	17.1 mH
Parasitic capacitance	797.4 pF
Natural resonance frequency	43.1 kHz
Maximal current	13 A

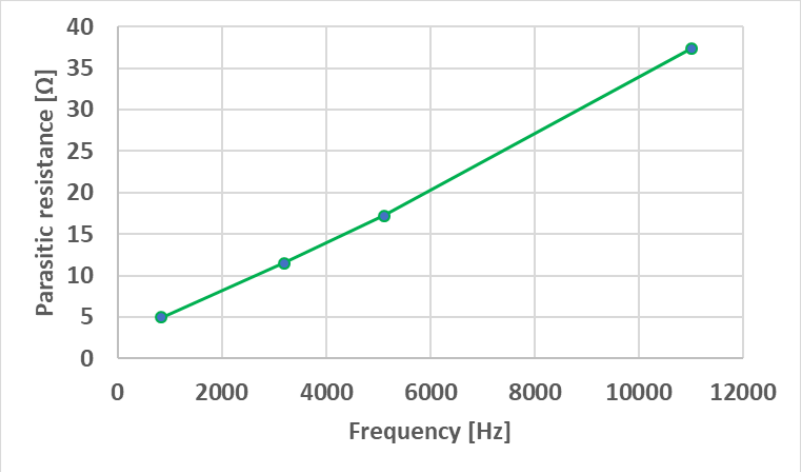

Figure 5.6: Parasitic resistance as a function of frequency - Square antenna # 1.

1 with only a different amount of copper wire used 4.9 kg. This smaller amount of copper obeyed the lack of material at the time of production. Its characterization is presented in Table 5.3

Figure 5.7: Square antenna for TTE communication with 4.9 Kg of AWG 11 copper and transverse area of 1.72 m^2.

Table 5.3: Parameter characterization for square antenna # 2.

Characteristics	
Shape	Square
Side	131 cm
Number of turns	25
Wire diameter	2.305 mm
Area	1.72 m^2
DC Resistance - Theoretical	0.54 Ω
DC Resistance - Experimental	0.64 Ω
Inductance - Theoretical	2.968 mH
Inductance - Experimental	2.887 mH
Maximal current	13 A

5.3.3 Octagonal antenna

The objective of this antenna was to provide a more efficient option to square antenna # 2 and that be easier to transport in difficult access underground environments. To accomplish this prerequisite, an octagonal PVC structure was used with a 2.43 m^2 increased area and 2.97 kg AWG 11 wire copper as shown in Figure 5.8.

Figure 5.8: Octagonal antenna for TTE communication with 2.79 Kg of AWG 11 copper and transverse area of 2.43 m^2.

Additionally, a parasitic resistance analysis was carried out to verify its variation as a function of frequency and its shown in Figure 5.9.

Table 5.4: Parameter characterization for octagonal antenna

Characteristics	
Shape	Octagonal
Side	71 cm
Number of turns	14
Wire diameter	2.305 mm
Area	2.42 m^2
DC Resistance - Theoretical	0.33 Ω
DC Resistance - Experimental	0.42 Ω
Inductance - Theoretical	1.12 mH
Inductance - Experimental	1.258 mH
Parasitic capacitance	497.84 pF
Natural resonance frequency	200 kHz
Maximal current	13 A

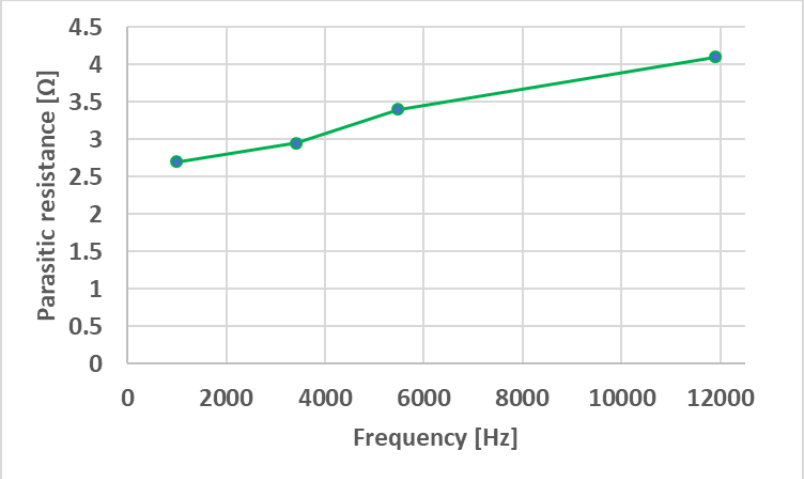

Figure 5.9: Parasitic resistance as a function of frequency - Octagonal antenna.

5.3.4 Tag antenna # 0

This antenna was designed to provide an option for localization applications and is based on a Texas Instruments (TI) transponder model RI-TRP-R9QL-30 of 30 mm diameter in compliance with ISO/IEC 11784/11785. Specifically, the antenna uses a plastic reel to support the AWG 32 copper wire as seen in Figure 5.10.

As carried out with the other antennas, the characterization of this one is shown in Table 5.5.

5.3.5 Tag antennas # 1 and # 2

Two small wire antennas were designed and built. Figure 5.12 shows the design of the antennas, with the largest diameter being 8 cm and the smallest being 4 cm and the height 1.5 cm. The wire used was AWG 18 enamelled copper to produce a magnetic moment of approximately 52 A cm^2, due to the maximum current (3.3 A) that can be supplied by the amplifier **TS 250**.

Figure 5.10: Tag antenna # 0 for TTE communication with 11 g of AWG 32 copper and transverse area of $1,76x10^{-6}\ m^2$.

Table 5.5: Parameter characterization for Tag antenna # 1.

Characteristics	
Shape	Circular
Diameter	28 mm
Length	20 mm
Number of turns	443
Wire diameter	0.202 mm
Area	$1.76x10^{-6}$ m^2
DC Resistance - Theoretical	20.94 Ω
DC Resistance - Experimental	24.46 Ω
Inductance - Theoretical	3.86 mH
Inductance - Experimental	3.87 mH
Parasitic capacitance	202.02 pF
Natural resonance frequency	180 kHz
Maximal current	90 mA

Figure 5.11 shows the sketch design, and a built antenna to which a PVC case was added in order to provide mechanical and environmental protection.

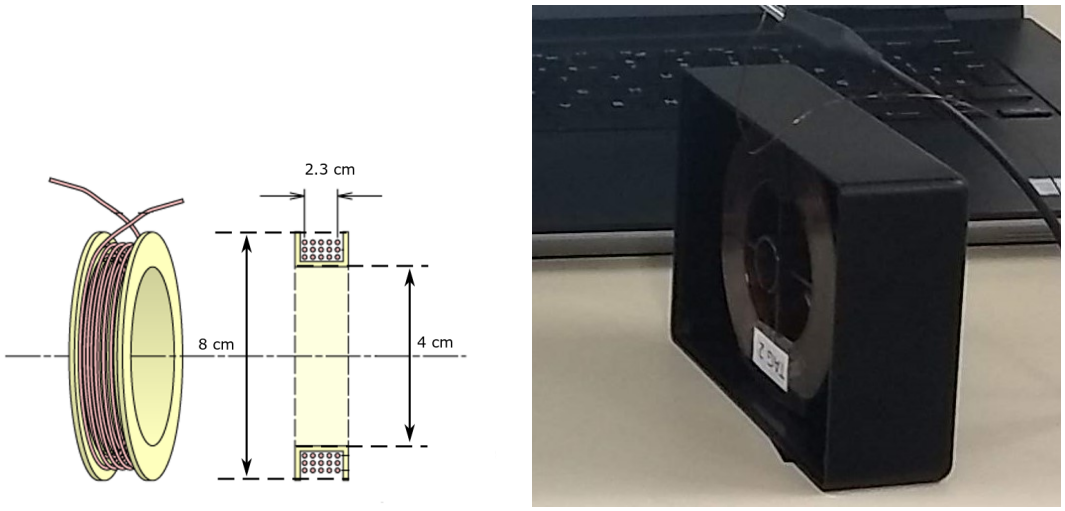

(a) Tag antenna project.

(b) Detailed view of Tag antenna # 1.

Figure 5.11: Tag antennas design and built details.

The resulting antennas were then tested to identify their electrical characteristics by the means of a RLC circuit meter and those values are shown in Table 5.6.

Table 5.6: Electrical characteristics of Tags # 1 and # 2.

Antenna	Number of turns	Resistance [Ω]	Inductance [mH]	Capacitance [nF]
Tag # 1	2786	10,9	15,9	62,13
Tag # 2	2761	10,8	15,0	65,80

Figure 5.12 shows both antennas after been enclosed by the protective case and ready for the tests.

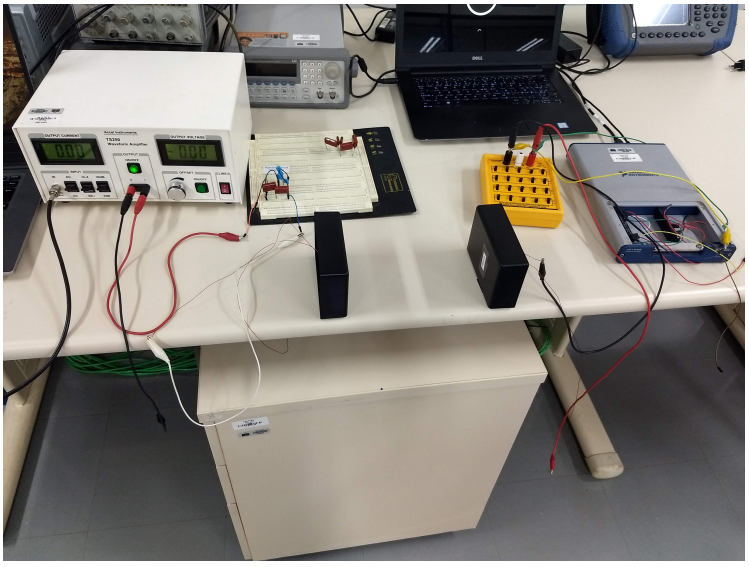

Figure 5.12: Tag antennas # 1 and # 2.

5.3.6 Flexible wire antenna

This antenna was designed to provide a reliable option in case of low transmission power in external experiments and to respect the power amplifier limitations. Its flexibility allows an less voluminous storage and easier transportation. It is made by a 6 mm^2 cross-section multiple wire flexible cable, being characterized for the largest possible configuration as seen in Figure 5.13.

Figure 5.13: Flexible wire antenna for TTE communication with a 6 mm^2 cross-section 240 m copper flexible wire with transverse area of 19.63 m^2

A simpler characterization has been made on this antenna, as can be seen in Table 5.7. It is designed exclusively to be a transmitter antenna that best optimizes all parameters of the power amplifier and is of a size that matches the proposed tests for this study.

Table 5.7: Parameter characterization for flexible wire antenna.

Characteristics	
Shape	Circular
Diameter	5 m
Number of turns	15
Wire diameter	2.7 mm
Area	16.635 m^2
DC Resistance - Theoretical	0.71 Ω
DC Resistance - Experimental	0.75 Ω
Inductance - Theoretical	2.397 mH
Inductance - Experimental	3.107 mH
Maximal current	36 A

5.3.7 Maximum antenna length for maximum magnetic moment.

Due to limitations of the power amplifier used in the study, certain parameters were set to better harness its transmission power. The amplifier used, the $TS250-1$, has a voltage limitation range of $\pm 20\ V_p$ and the current its limited to $3.3\ A\ RMS$. These parameters and the antenna material, it was possible to find the maximum optimization threshold of the antenna materials, which means that if more material is used, part of that conductor will be underutilized, as the wire resistance augments with length and makes voltage decrease. Thus, there is no improvement in antenna performance as the number of turns increases because what limits the transmission power is the power amplifier capabilities.

By using MATLAB, it was possible to carry out the estimations of magnetic moment as a function of wire dimensions:

$$m_d = \frac{A}{p}\frac{M}{\sqrt{\rho_v \rho_{Cu}}}\sqrt{\min(V, IR)\min(I, V/R)}, \tag{5.19}$$

in which $A = \pi r^2$ is the antenna area and $p = 2\pi r$ its perimeter, $NP = \frac{R\alpha}{\rho_{Cu}}$ is the total wire length, $M = NP\alpha\rho_v$ its mass and $\alpha = 6 * 10^{-6}\ m^2$ its thickness, $\rho_{Cu} = 1.7210^{-8}\ \Omega/m$ is copper resistivity and $\rho_v = 8960\ kg/m^3$ its volume density, $V = \frac{20}{\sqrt{2}}\ V$ is the RMS maximum voltage, $I = 3.3\ A$ the maximum current, $r = 1\ m$ the antenna radius, and $R = 2V/I\ \Omega$ the wire resistance.

Comparing antennas of the same area with radius of $1\ m$, Figure 5.14 shows that the magnetic momentum stabilizes around a wire length of $1500\ m$, that is, if a longer winding is done, there will not be improvement in the antenna as transmitter, because the power amplifier is limiting the transmission.

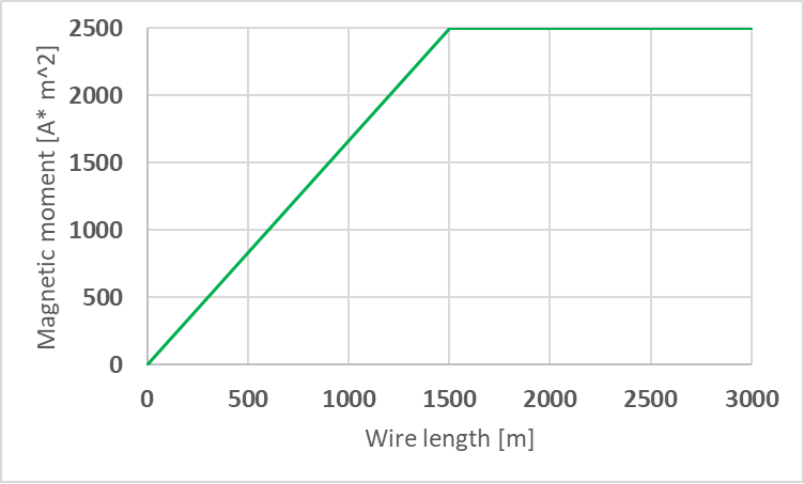

Figure 5.14: Relationship between wire size and magnetic moment from a fixed area antenna using a voltage limited amplifier.

In Figure 5.15 is easy to see that the best resistance for a transmitting antenna, in the aforementioned conditions, is around 4.3Ω because this value represents the best voltage-current ratio

the amplifier can provide.

Figure 5.15: Relationship between the resistance and the magnetic moment of the antenna to obtain the maximum voltage-current ratio from the power amplifier.

To improve power transmission, the characteristics of the antenna or amplifier can be altered up to a certain extend. Thus, if the antenna number of turns is increased the current will decrease proportionally, so when it is necessary to improve the performance, the antenna area can be change obtaining a second order gain, which consequently improves the magnetic moment.

6 PLATFORM FOR SIMULATIONS AND MEASUREMENTS

In order to supplement the channel modeling presented in the previous chapters, it is necessary to present results of measured data. To carry out such measurements, the ideal scenario would be several underground mines; however, due to governmental regulations it is quite bureaucratic to have access to a mine and even more to several. Thus, it was decided to carry out tests in different environments as the telecommunications laboratory, an underground tunnel in the subway Central Station and in a underground cave.

Due to the nature of the TTE communication systems, few gadgets were available in the Brazilian market, and to uphold the spirit of research, it was decided to project and build the communication system for short distances (up to 100 m) which includes: antennas, transmission, reception and tuning circuits. Therefore, in this chapter is first described the communication system and then the measurement results.

These platforms were built during 5 years by several different students including the author.

6.1 RESONANCE CAPACITANCE CIRCUIT CHARACTERIZATION AND CHANNEL TRANSFER FUNCTION ESTIMATION.

A natural following step was to carry out transmission tests between the TTE antennas presented in the previous chapter. To do so, codes were implemented in MATLAB to interact with the equipment described in section 6.3.3. This platform provides transmission and reception capabilities by changing the configuration.

This application establishes a link between the MATLAB GUI and the antenna and provides an interface to introduce the following parameters:

- **Mode:** the user has to choose from three modes: transmission, reception or synchronized. The first two are self explanatory and the last one is for in-lab tests.
- **Type:** this code has two options related to antenna and channel characterization. The first one provides the antenna frequency response to identify its resonance and adjust the tuning circuit. The second mode provides the channel transfer function.
- **Direction:** there are three options: coaxial, co-planar and diagonal, depending on the antennas relative position.
- **Transmission resonance:** it is possible to carry out measurements with and without the transmission tuning circuit. In its absence, the code performs a voltage compensation to

keep the output current stable.

- **Signal amplitude:** the user can set the maximum peak amplitude respecting the amplifier limit in current and voltage.
- **Central frequency:** this code provides up to 250 kHz of bandwidth with a central frequency set by the user. In practice, the upper limit depends on the self ressonance frequency of the antennas.
- **Geometrical characteristics:** dimensions related to vertical and horizontal distances between the antennas can be set with this parameter to compare with theoretical models so it is not mandatory for measurements.

Subsequently, for transmission the main code generates a sequence of Carrier Wave signals and sends them to the DAC board (NIDAQ), which in turn delivers the signals to the power amplifier. This device elevates the voltage in ten times and delivers it to the tuning circuit and finally to the antenna. The amplifier is also connected to the NIDAQ and sends output current information to the MATLAB platform, which plots the output current vs time or the antenna frequency response according to the option selected. Figure 6.1 shows an approximation of the sequence of activities carried out in the transmission side.

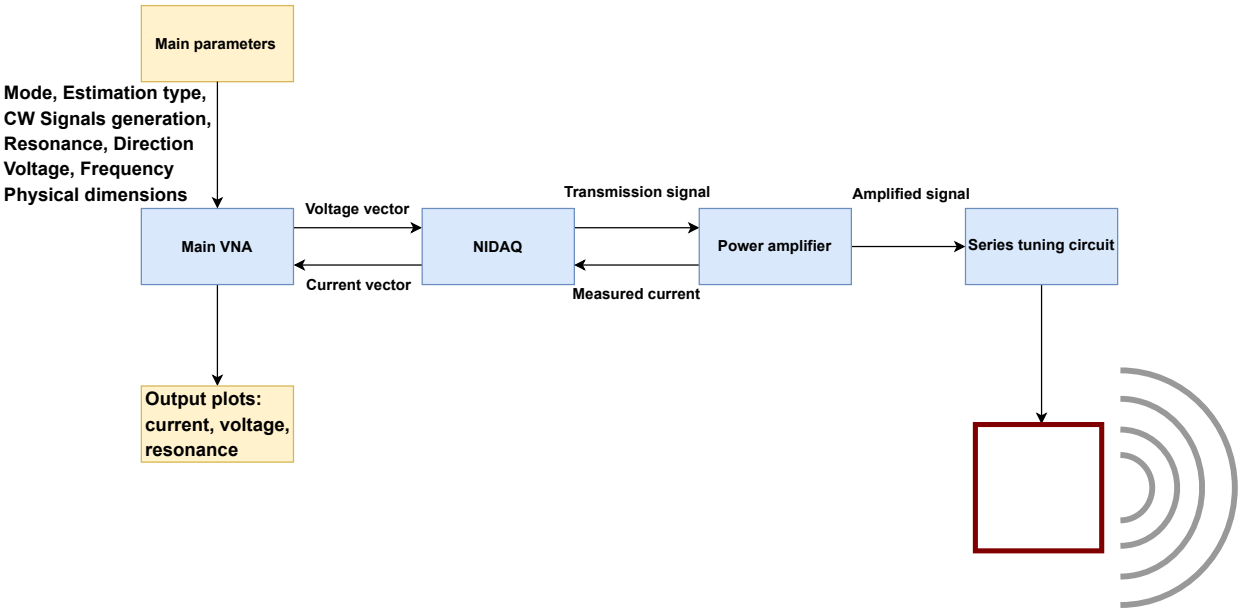

Figure 6.1: Transmission chain for TTE communication tests.

Similarly for the reception, the platform can be set to receive information or to characterize the antenna resonance. When it works as a receiving antenna, the platform must be triggered before the transmission is initiated, as the received wave gets a value above a threshold, the NIDAQ performs an analog to digital conversion.

After all CW signals are processed, both transmitted and received signals are mapped to the frequency domain by applying the Fast Fourier Transform and the system transfer function is

computed. Regarding the synchronized mode, in which the same clock is used to control both NIDAQs, the transfer function phase and amplitude are computed. In opposition to this, the external measurements considered only amplitude data. Figure 6.2 shows an approximation of the sequence of activities carried out in the reception side.

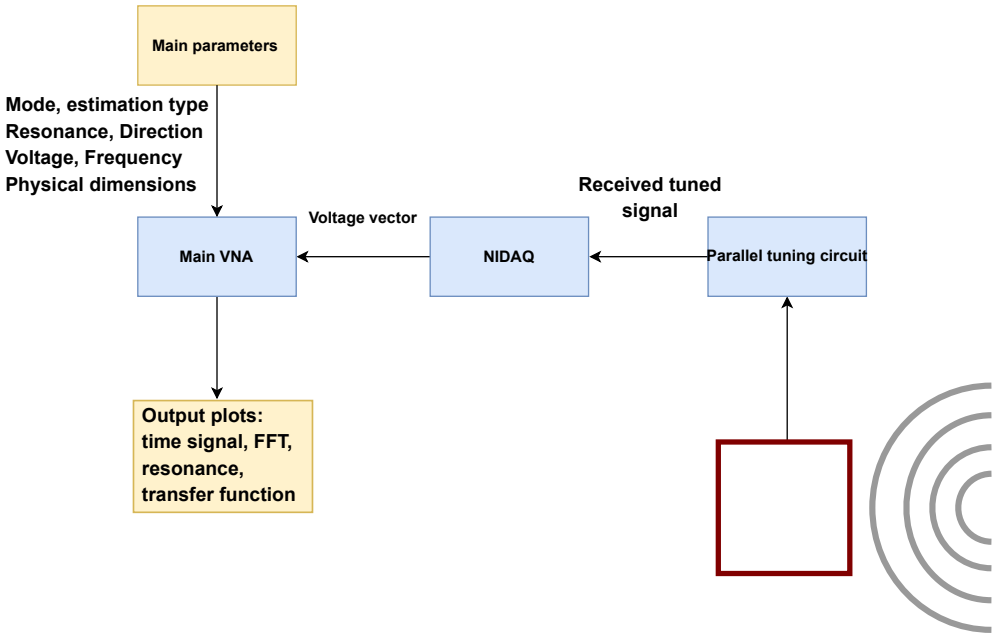

Figure 6.2: Reception chain for TTE communication tests.

In order to extract the propagation channel parameters, it is necessary to perform separate measurements with the resonant circuit in each end, in both ends, and a measurement with no resonant circuit. Afterwards, data with resonance in both ends is normalized by the individual data, antenna admitances, number of turns and their transverse area to estimate the channel transfer function (induced voltage/ transmission current), the received magnetic field, the channel gain (induced voltage/ transmission voltage), and medium apparent conductivity.

6.2 BIT ERROR RATE ESTIMATION PLATFORM.

In a similar way, a software application platform was developed in MATLAB to carry out Bit Error Rate (BER) estimations. Figure 6.3 shows the block diagram associated and each part is explained as follows:

Main parameters

- **Method:** *transmission* or simulation. The second option allows the use of a seed to replicate a previous simulation; two different types of channel a TTE model or a flat channel; and the type of noise AWGN or a previously measured one.
- **Mode:** there are three modes: transmission, reception or synchronized. The first two are self explanatory and the last one is for in-lab tests.
- **Signal type:** *raised cosine* or duobinary pulse.
- **Channel coding:** this feature defines the Galois Field in which the code operates, and the number of symbol errors the code can correct.
- **Modulation band:** two options are set baseband or passband.
- **Modulation Scheme:** *BPSK* or QPSK.
- **Equalization:** three options are given zero-forcing, Viterbi algorithm or *none*.

Digital Signal parameters

- Roll-off factor.
- Transmission rate.
- Number of bits per loop and number of loops.
- Transmission power or array with Eb/No values for simulations.
- Number of samples per symbol.
- Impulse response filter duration.
- Carrier Frequency.

With these data, the application preprocesses other parameters and performs the following processes:

- Sampling rate.
- Symbol rate.

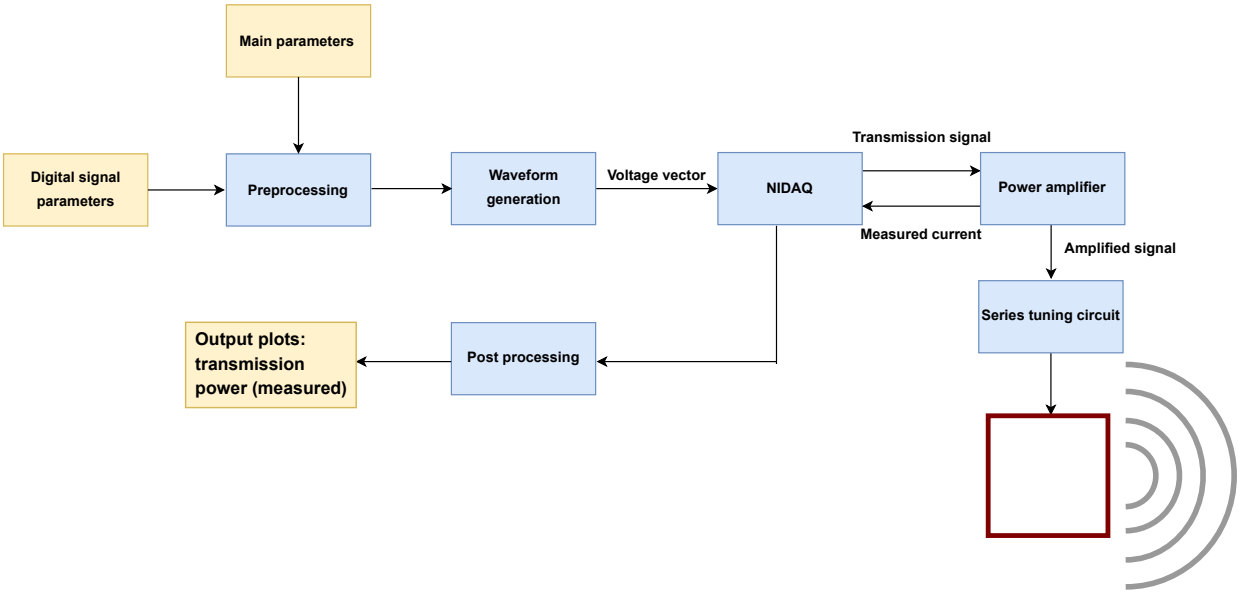

(a) Transmission circuit.

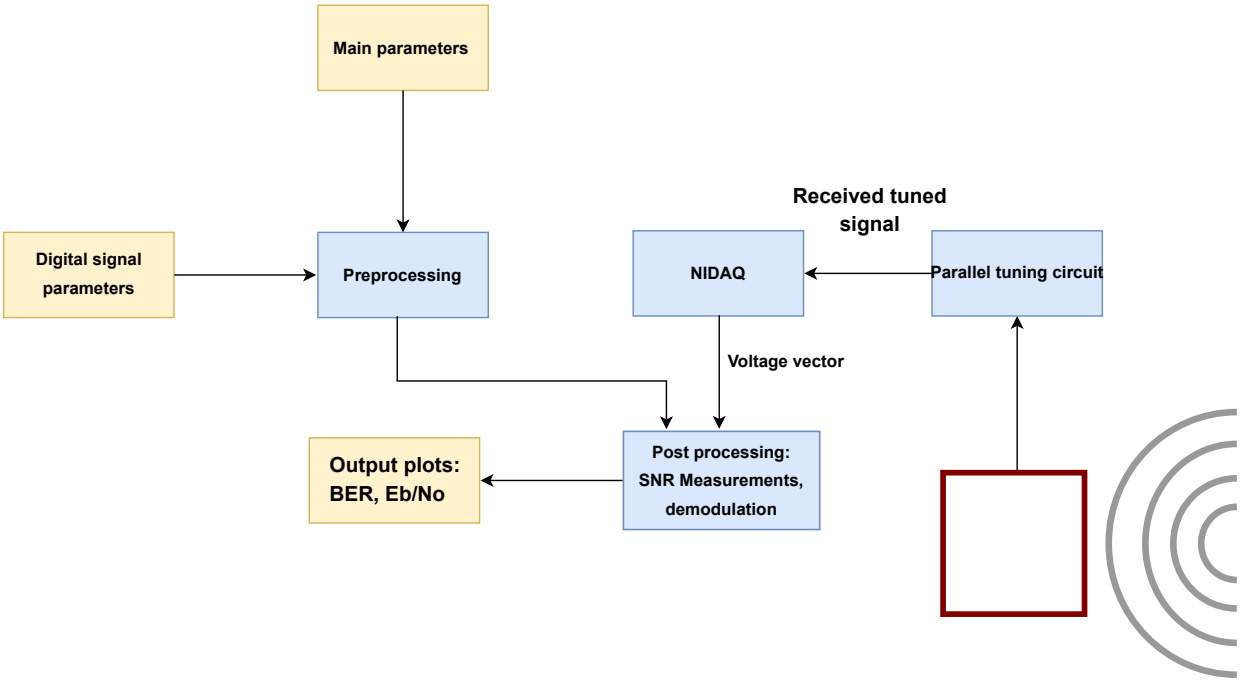

(b) Reception circuit.

Figure 6.3: Bit Error Rate estimation platform block diagram.

- Transmission bandwidth.
- CW waveform generation which provides a high SNR to trigger the receiver.
- Modulation/demodulation function preparation.
- Bits sequence generation (message).
- Channel codification parameters calculation.
- Message codification.
- Channel impulse response generation (simulation mode only).
- Noise model loading (simulation mode only).
- Channel equalization parameter estimation.
- Carrier signal generation.
- Baseband waveform generation.
- Transposition to passband (optional).

These processes are repeated according to the loop number defined by the user.

6.3 NOISE MEASUREMENTS

Noise received by a magnetic antenna at low frequencies is usually from atmospheric discharges and from power line harmonics [70]. In the same manner, noise from electric equipment and radio transmission might impact TTE communication. This section presents these concepts in detail.

With regard to techniques for estimating and mitigating harmonic noise, Alhaj in [71] proposes a Least Mean Squares algorithm to calculate continuously the amplitude and phase from each harmonic. Similarly, Neves in [72] developed a communication simulator based on TTE channel models, atmospheric noise, power line harmonic estimation and mitigation. However, this work considers real noise measurements in diverse interference conditions to provide a more realistic performance.

6.3.1 Atmospheric noise

This noise is generated mainly by atmospheric discharges propagates over the Earth surface to distant places, as TTE signal propagates into the soil, it is easy to realize that the down-link communication is affected more significantly than the up-link, due to the high attenuation suffered

by the noise within soil. Moreover, according to Schlegel et at in [73], Eddy currents are induced in the conductive medium as a result of horizontal E-field component, which reduces the overall E-field penetrating the soil and attenuates the noise rapidly. This fact conditions the antenna orientation that has to be placed in parallel to the ground to guarantee the field orthogonality getting to the underground antenna.

Regarding noise modeling, Raab in [20] considers this type of noise as a pulse combination that depends on the arrival direction and soil slope. A more complete study is presented by Field in [74] showing atmospheric noise as the sum of an impulsive and a Gaussian components. Specifically, the impulsive component is created by close atmospheric discharges and the Gaussian is the addition of distant atmospheric discharges along with other electromagnetic sources as electrical equipment.

Considering the atmospheric noise as the main source of noise-floor sensed at the receiver it can be related to the noise temperature using the following equations presented by Gibson in [4]:

$$F_a = 10 \log \left(T_a / T_0 \right) \tag{6.1}$$

that gives in dB:

$$F_a = PSD_a - 20 \log \left(N_R S_R \right) - 40 \log \left(f \right) + 492 \ \text{[dB]}, \tag{6.2}$$

6.3.2 Anthropic noise

This type of noise is generated by human action, mostly created by power line harmonics at low frequencies and that might be sensed miles away from the source depending on the transmission voltage. Similarly, electrical equipment connected to the power network can generate noise indoors. Additionally, according to Skomal in [75], magnetic and electric antennas can sense 60 Hz harmonics up to the Very Low Frequency band.

6.3.3 Noise-floor measurements

The magnetic antenna used for noise floor detection is 131 cm square in shape, covering an area of 1.17 m ^{2}. It was mounted around wooden supports, maintaining the square shape before and after the winding process. The antenna is build with 63 turns of cooper wire , 1.32 Ω resistance and 17 mH inductance. These values were measured in the laboratory and are in agreement with the theoretical models. The resistance and inductance information of a loop antenna is important as it defines the amount of power dissipated and the input impedance at the receiver. Figure 6.4 illustrates the reception scheme used.

The antenna is connected directly to a data acquisition board from National Instruments, NI USD-6341, that has amplifiers and low-pass filters that precede the analog digital converter, configured to sample the noise at a rate of 500 thousand samples per second. In practice, only the

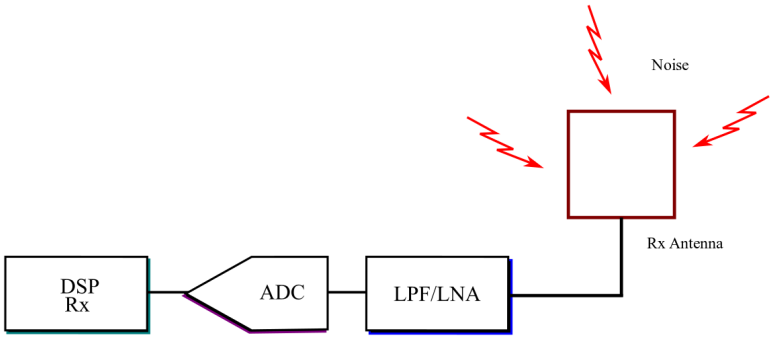

Figure 6.4: Reception system block diagram used for measurements.

band between 0 and 10 kHz is of interest in this work, bringing us to reprocess the signal with filters and subsampling. When added to the simulated signal for performance analysis on a TTE channel, the demodulation is done without orthogonal channels, as the transmitted (simulated) signal is BPSK. In this way, the analysis of noise envelope distribution considers simply its absolute value normalized by its mean deviation, for comparison between the different measurements and the AWGN channel.

Various field measurements were realized in the city of Brasilia, Brazil, between the months of October 2017 and March 2018, a period considered as one of great incidence of rain the central region of Brazil. The measurements were realized in the center of the University of Brasılia (UnB), next to the University Restaurant (RU); in the Olympic Center (CO) of the university, which is close to the university and next to the lake Paranoa, of Brasilia; and in a semi-rural region of Brasilia named "Núcleo Rural Olhos D'água" (NR). The following figure shows a map of those locations:

The vertical component of the magnetic field was measured by placing the antenna horizontally on the ground. The most representative measurements were chosen from each of the 3 measurement spots, those that had a statistical mode that better represented the noise in those places. It is important to note the local conditions of terrain and electromagnetic interference. The terrain curvature can influence in the perception of the horizontal component of the magnetic field, which is not desirable, but commonly observed [70].

Regarding the measurement environment in RU, it can be highlight the moderate terrain slope of the whole university itself, and the high number of machines, such as boilers and generators around the antenna (up to 10 meters), besides the machinery in the industrial restaurant. The electromagnetic emissions of their large equipment can increase the detected background noise. The terran in CO in more even, as it is closer to the lake, and there is no machinery close to the antenna.

Figure 6.5: Map of testing sites University Restaurant (RU), Olympic Center (CO) and Núcleo Rural Olhos D'água (NR).

However, a 138 kV transmission line is found a few hundreds of meters from the measurement point, certainly raising the local power line harmonic interference. The NR measurement spot is quite remote, and with a relatively low human presence. However, a transmission line was present at a distance of just below 1 km from the antenna. In the measurement spot, a high slope is observed. Em NR other polarizations were carried out besides the vertical, by positioning the antenna perpendicularly to the ground on the north-south and east-west directions. As a reference, the closest transmission line, which has a voltage of 138 kV, was at a an angle of -31° in relation to the north direction. Therefore, we expect a higher contribution to the horizontal magnetic field in the north-south direction than in the east-west direction.

6.3.4 Measurement based simulator

The simulated system utilized BPSK (Binary Phase Shift Keying) and a root raised cosine (RRC) with a roll-off factor of 0.5, and two different scenarios were tested. The first considers the transmission of a modulated signal with a carrier frequency of f_c =5 kHz, bandwidth of 3 kHz a symbol rate of 2 kbauds. In the second scenario, the transmitted signal possesses the same carrier frequency but a bandwidth of 9.6 kHz and 6.4 kbauds of symbol rate. The optimal frequency of the TTE channel is maintained constant at f_c, which demanded an electrical conductivity of 0.01 S/m, a magnetic permeability of $4\pi \times 10^{-}7$m and a transmitting loop at a depth

of 200 meters, coaxially aligned with the receiving antenna at the surface. In practice, usually the optimum frequency is estimated first, and after that the carrier frequency is chosen. No channel estimation or equalization technique was used, nor was channel codification used to lower the bit error rate. The main objective was to see the effect of communication performance degradation in the presence of the TTE passband channel and of the measured noise, in relation to a AWGN channel.

For the bit error rate estimation, the noise for each experiment was normalized so that they had the same equivalent power, integrated on the passband of the root raised cosine filter. This way, the performance comparison of different noise measurements did not depend on the absolute value of the noise power, but instead on their distribution. The same occurs for the probability density function (PDF) of the noise for the different sources, as the noise is passed through the root raised cosine filter, its power is normalized, and the PDF calculated.

6.3.5 Results and discussion

Figure 6.6 presents the power spectral density (PSD) of the measured noise in "Núcleo Rural Olhos D'água" (NR), with the antenna placed in three orthogonal directions, to obtain all magnetic field components (vertical, horizontal north-south and horizontal east-west), in the frequency range from 3.5 to 6.5 kHz. The observed noise floor is considered to have the atmospheric noise as dominant. An unexpected higher value of the DSP noise floor can be observed on the vertical component than in the horizontal directions. This can be attributed to the slope of the terrain around the measurement spot, which can lead to a lack of a reliable reference to determine if the field vector is actually perpendicular to the ground. Regarding the harmonics of the power line, we can note higher values for the north-south horizontal component. As mentioned above, a 138 kV power line was tangent to the measurement spot at a few hundreds of meters, at an angle of -31° in the north-south direction, which explains the higher noise value of this component in this direction.

Figure 6.7 presents the comparison between the measured noise of the vertical field in RU, CO and NR, in a frequency range of 3 kHz bandwidth around 5 kHz. We can note higher levels of harmonic noise in NR, even though there is a lower noise floor. In RU, the noise floor is pretty high, and it is likely that the atmospheric noise is not dominant, and instead the noise is composed primarily of interference generated by the close machinery. The harmonic noise is practically overlaid by the background noise, at least in the considered band. Even though it is not shown in the figure, the harmonic components are important below 1 kHz. Regarding the observed noise levels in CO in the same band, at first we observe a behavior similar do the one in RU, with a noise floor dominating over the harmonics. Even if it is not clear from the spectra, we see in the following results a behavior more impulsive in the noise in CO compared to the one in RU, even if such behavior is moderate, arising from the harmonic and/or impulse atmospheric noise. It is also important to remember the existence of the 138 kV transmission line close to the measurement spot in CO.

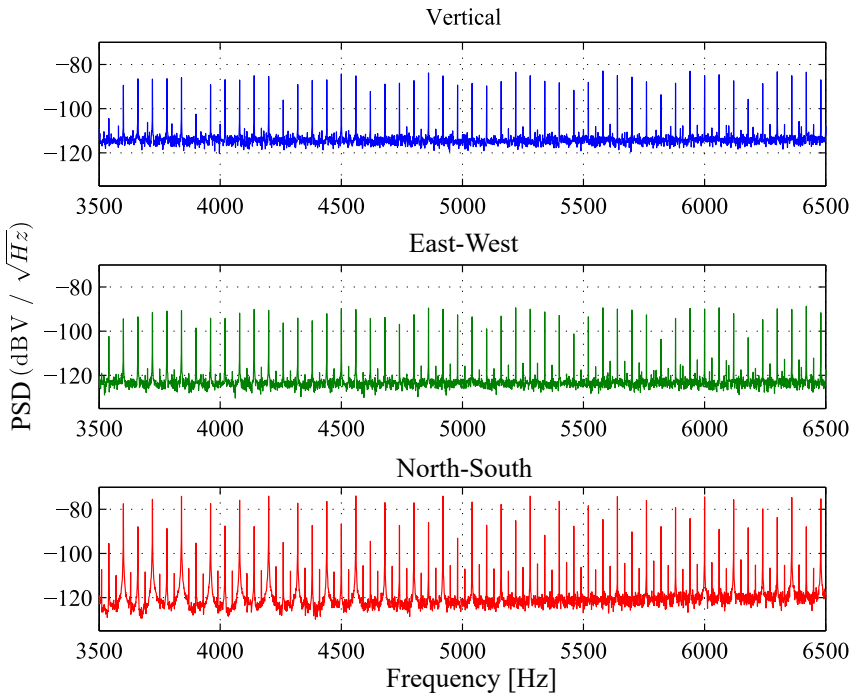

Figure 6.6: Noise power spectral density measured for three orthogonal components of the magnetic field vector.

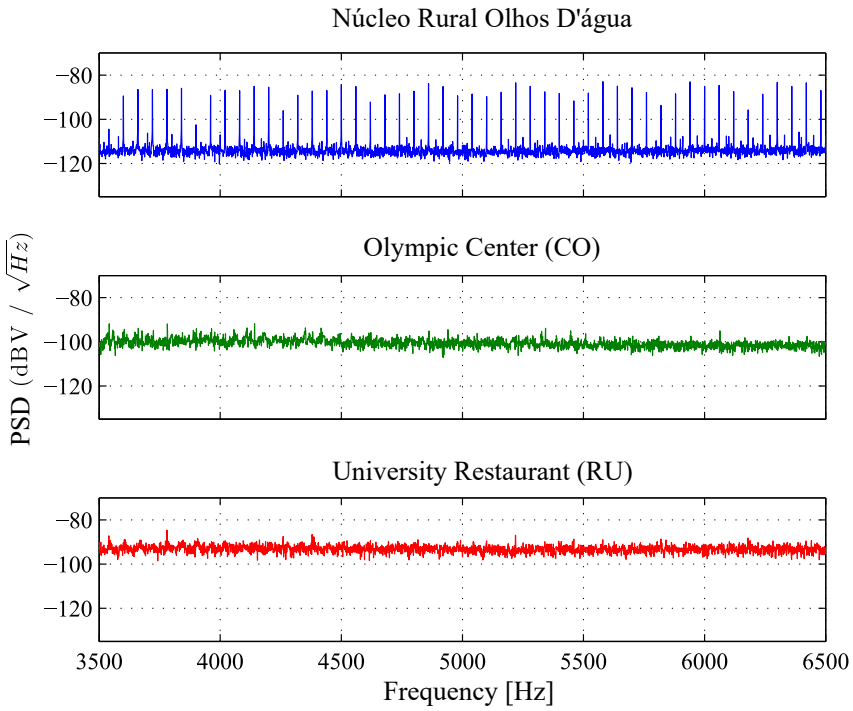

Figure 6.7: Noise power spectral density measured with respect to the vertical magnetic field in NR, CO and RU.

Figures 6.8 and 6.9 present the probability distributions of the noise absolute value in NR, CO and RU in the bandwidths of the 3 kHz and the 9.6 kHz signals filtered by the root raised cosine filter in passband. For comparison, the white gaussian noise with zero mean and 1 variance was

included.

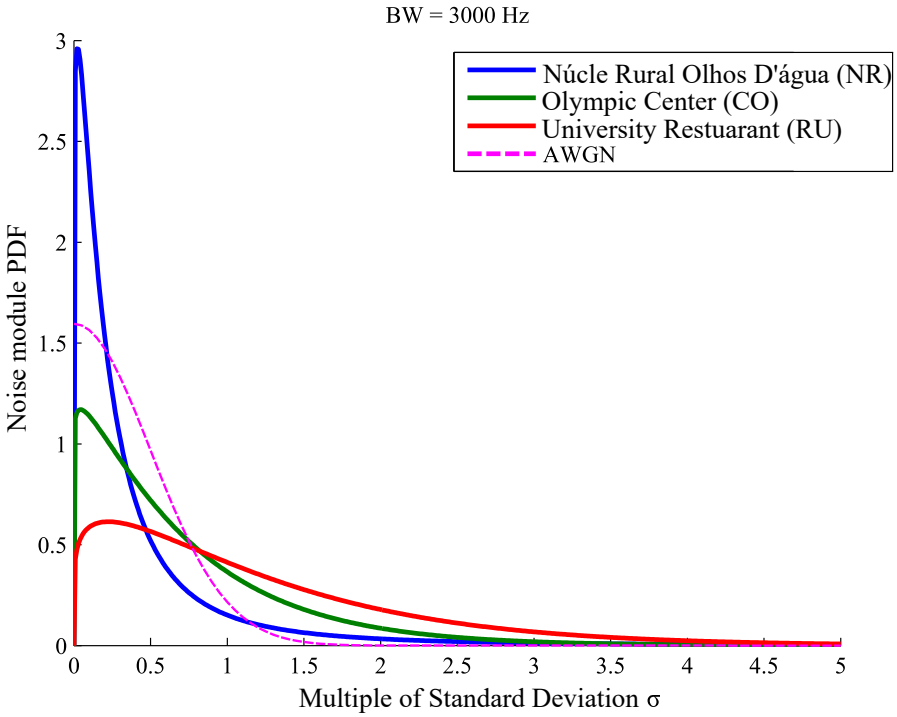

Figure 6.8: Noise probability density function measured at 3 kHz in NR, CO and RU.

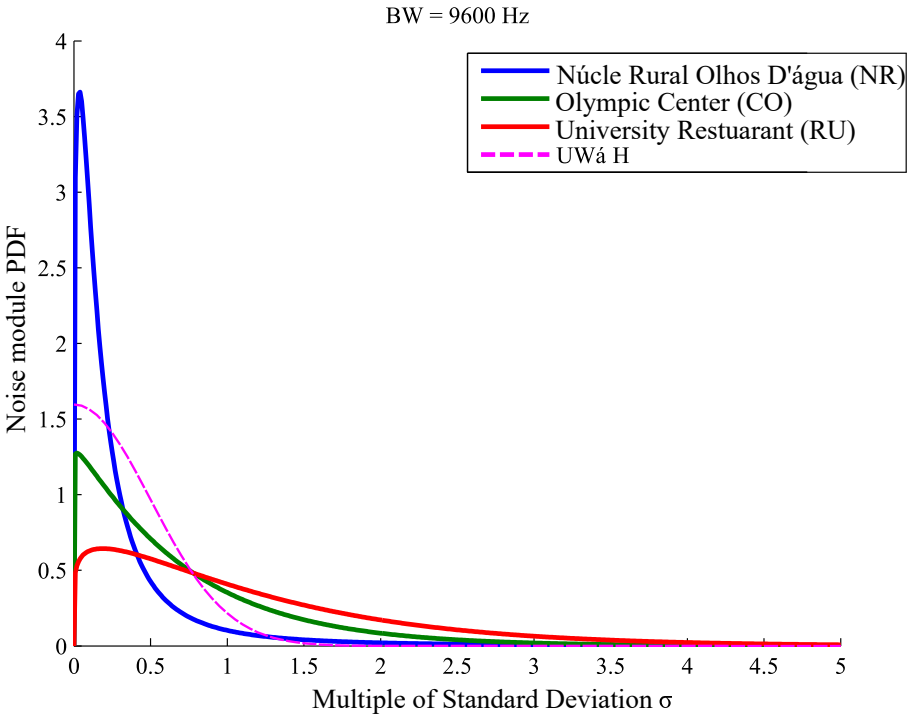

Figure 6.9: Noise probability density function measured to 9 kHz in NR, CO and RU.

Little difference can be noted in terms of distribution, in the 3 kHz or 9.6 kHz bandwidth signals in any scenario. This indifference to the bandwidth is also seen in Fig. 6.10, in which

the transmission quality is assessed from the measurement of bit error rate (BER) in terms of the energy per bit divided by the power spectral density of noise (Eb/No). It is noticeable the fact that the strong harmonics present in frequencies up to 1 kHz are excluded from the signal of 3 kHz bandwidth, while these are not excluded in the 9.6 kHz bandwidth signal. In the same fashion, it is important to note that the bandwidth of the channel is quite large for average and high depths, reaching 11 kHz (non-symmetric) in the tested configuration, and therefore there is a low linear distortion. Regarding the strong harmonics up to 1 kHz, the fact that they occupy a marginal and thin band in the spectra of the signal can answer for the low influence of the bandwidth in the communication link quality. Here, the noise is normalized so that they all have the same power, with a mean DSP equivalent to AWGN noise. In this way, we can compare the performance among all scenarios in relation to an equivalent EbNo.

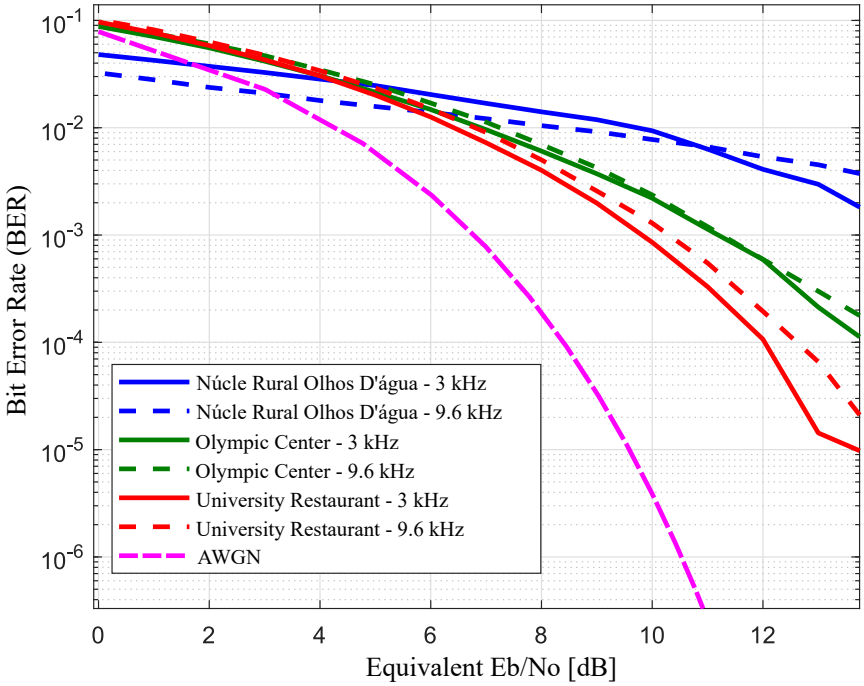

Figure 6.10: Comparison of BER in NR, CO and RU for the 3 kHz and 9.6 kHz bands

A strong connection can be noted between the noise distribution in Figures 6.8 and 6.9 and the degradation of the transmission quality in Figure 6.10. The more dispersive the PDF of the noise, such as in RU, the more efficient the transmission, and closer we are to an AWGN behavior. The worst result in NR points to a high concentration of noise values. In this case, such a profile is likely due to the high concentration of harmonics in the power lines that generate period pulses of low peak value. In CO, it is interesting to note that, even though it has a distribution closer to AWGN noise, its performance in terms of BER was inferior to that in RU, which possesses a more disperse distribution of noise. Although covered by background noise, the harmonic components of the power lines are evidently present in a higher proportion than in RU, contributing to a higher degradation of BER, since a 138 kV transmission line close to the CO measuring spot.

6.4 UNDERGROUND TRANSMISSION AT THE UNIVERSITY RESTAURANT

For this test the Square antennas # 1 (inside the tunnel) and # 2 (in the surface) were used to estimate: channel transfer function, channel transfer impedance and BER estimation. The diagram represented in Figure 6.11 summarizes the communication system, either for channel sounding or for digital signal transmission in the SDR based platform. Both roles of source and load/acquisition system are performed by two independent National Instruments NI USB 6341 boards, and the entire modulation/demodulation and signal processing process are realized in real time with the help of one (or two) computers.

The measurements were carried out in an underground tunnel that connects the student restaurant of the University of Brasilia (RU/UNB) to its steam boiler place. The medium is composed of layers of air (250 cm), concrete (20 cm), soil (165 cm formed of earth and stones), and asphalt (15 cm). It was performed a comparison between that data and the theoretical propagation curves in non-conductive medium (air) at 1 m and 4.5 m in a quasi-static field zone. Also, it was compared with a reference measurement carried out at a distance of 1 m within air. The direction of transmission is from surface to underground.

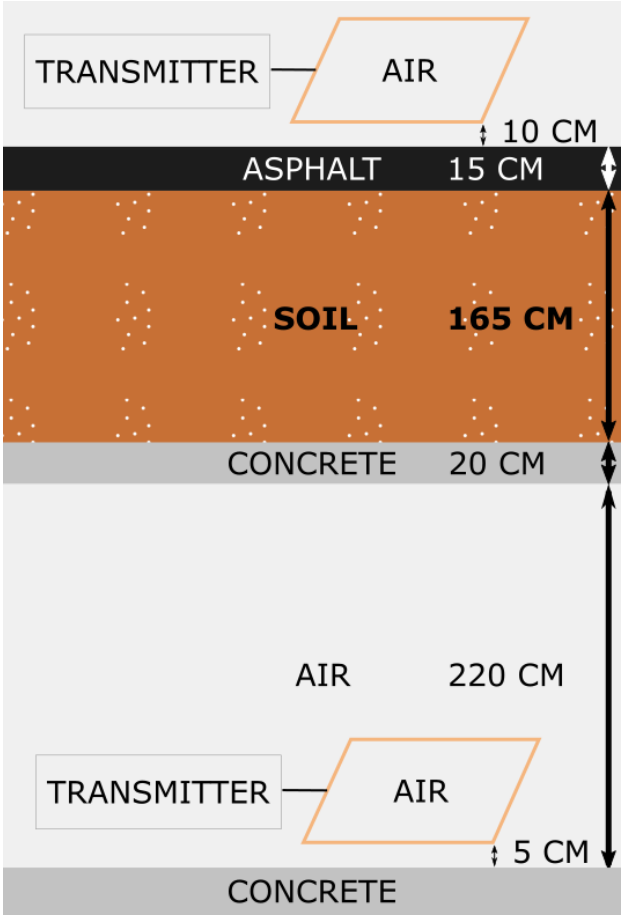

Figure 6.11: Scenario for TTE communication. Representation of the environment between underground tunnel and car parking at the RU/UNB.

6.4.1 Characterization of the Resonant Antenna

To obtain resonance, it is important to calculate the corresponding capacitance, which is given by:

$$C_r = \frac{1}{4\pi^2 L f_r^2} \quad \text{[F]}, \tag{6.3}$$

where C_r is the capacitance required to produce a maximum gain at the resonance frequency f_r and L is the antenna's inductance.

The capacitor is positioned in parallel with the antenna both for the transmitter and receiver to drain maximum current to the transmitting antenna and maximum voltage to the load. For an inductance of 2.9 mH on the transmitting antenna, it is computed a resonance capacitance of 341.7 nF, at the frequency of 5 kHz. Similarly, for the receiving antenna, which presents an inductance of 17 mH, it was found a capacitance of 59.6 nF at the same frequency.

6.4.2 Characterization of the Propagation Channel

For characterizing the propagation channel the frequency method is used, where N tonal signals sweep the desired band. The complex division between the received and transmitted signal spectra allows us to estimate the channel transfer function. To reduce interference effects by secondary lobes of consecutive tones, the Hanning windowing is employed on time domain.

6.4.3 Characterization of the Digital Communication System

For the communication test it is chosen the use of BPSK signals with a symbol rate of 200 symbols/s at a 5 kHz carrier. This narrowband is usual in TTE communication specially because of the preferred resonant circuits with high gain and Q-factor. Other configurations with dumping resistance may be tested in future works to increase the bandwidth at the cost of reducing the power spectrum density of signal.

The baseband signal is raised cosine filtered with 50% roll-off factor with the purpose of reducing the effects of linear distortion out of the transmission band and filter the noise more efficiently. Channel estimation in frequency domain and zero-forcing (ZF) equalization are implemented for each frame of twenty thousand bits, using 50 pilots per frame, each with a duration equivalent to 16 symbols. Signals are filtered, mixed, summed, up and downconverted, etc. using digital signal processing techniques in a regular SDR platform. No Channel coding is used in this test.

6.4.4 Results and Discussion

In Figure 6.12, the channel sounding results are shown through the the TTE channel transfer function, comparing the CTF between surface and underground with the CTF for the QS model at 1 meter and 4.5 meters, and with the CTF measured in air at the reference distance. Analyzing the two upper curves, it can be seen that the reference measurement fits the QS model with a -2.7 dB offset. This difference may be justified by losses at the receiver and its lack of isolation at the measurement environment. This offset is used to calibrate the propagation loss in excess of TTE measurements in comparison to the QS model. By observing the two curves at the bottom of the graph, there is a difference of approximately 4.86 dB of excess loss in addition to the quasi-static model at the frequency of 5 kHz. Subtracting the 2.7 dB from the reference, there is 2.16 dB of excess loss considering the measurement inaccuracies. Comparing measurements for different short ranges to the equivalent QS model may be useful in channel modeling.

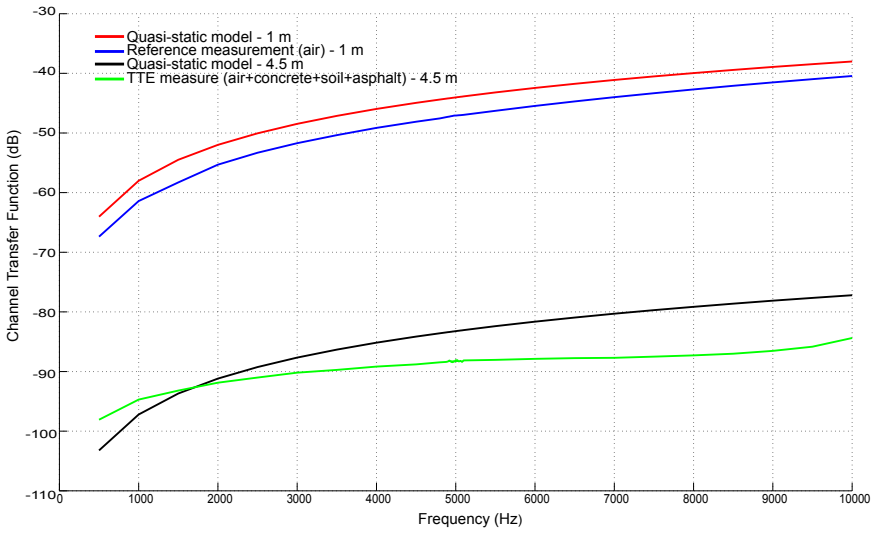

Figure 6.12: Channel's Transfer Function (CTF) comparison.

Figure 6.13 displays the channel impedance, taking into account the measured voltage at the receiver and the current passing through the transmitter. This calculation considers the characteristics of the transmit and receive antennas, such as their area and number of turns. When the resonance is used, the gain at each end is computed in the total impedance. It is observed that the gains in transmission and reception are similar, of around 28 dB, and bandwidth of 200 Hz. The consolidated system gain, for the TTE channel, is approximately 35 dB with a bandwidth of around 150 Hz. At the resonant frequency (5 kHz) it is observed that the total gain equals the sum of the non-resonant channel gain (-21.5 dB), the transmission gain (28 dB), and the reception gain (29 dB). Such addition presents an error of less than 1 dB.

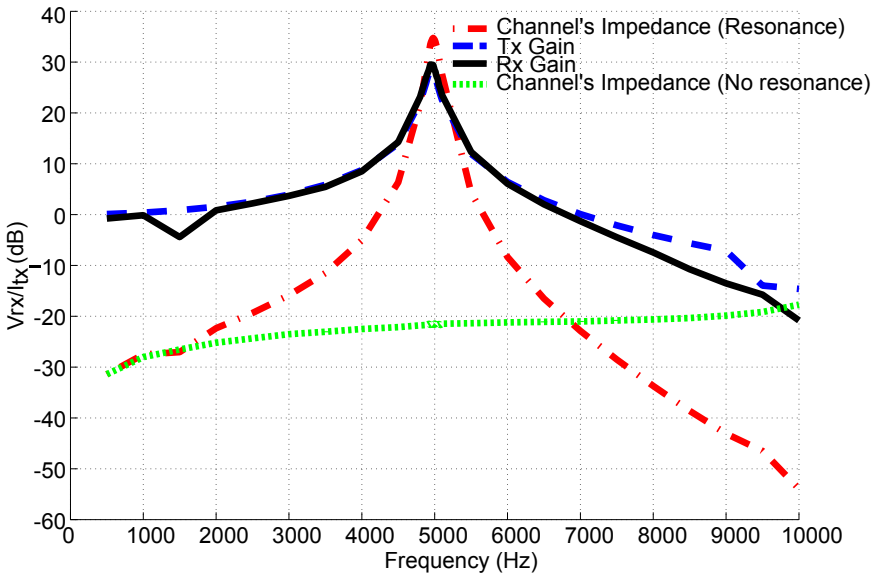

Figure 6.13: Experimental Channel's Transfer Impedance, measured according to the setup described at section IV.

Figure 6.14 presents the power spectral density of the internal and external noise with and without resonant circuit at the receiving antenna. Ignoring the resonant circuit and harmonic components, the atmospheric noise component in external noise is over 10 dB stronger than internal noise, which is expected for very low frequencies. The strong harmonic components may be explained by the presence of a diesel power generator and industrial steam boilers close to the measurement site. The curve corresponding to the resonant receiver presents higher noise levels with average power spectrum density (PSD) of about -70 $dBV/\sqrt{Hz}$ for some harmonics and -87 $dBV/\sqrt{Hz}$ for the background noise at 5 kHz. This amplification of noise could discourage the use of the tuning circuit at the receiver, but the use of untuned antenna causes a high-impedance inductive source to the receiver amplifier, which can lead to a high noise voltage if the receiver has a significant input bias current. In other words, the internal noise could become not so irrelevant as presented in Figure 6.14

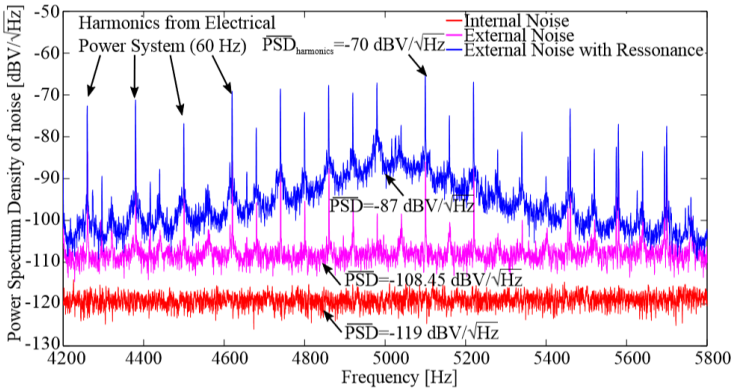

Figure 6.14: Experimental Characterization of Noise. Measurements of Power Spectral Density PSD of Receiver's Internal Noise, and External noise for tuned and untuned antennas.

Observing the middle curve and PSD for 5 kHz the temperature of atmospheric noise can be

calculated above that of thermal noise using (6.2). The obtained result of 198 dB is in accordance with the literature, but several measurements with different weather conditions and times are needed.

Figure 6.15 shows the bit error rate as a function of transmit power. It is observed that the transmission power values are low for this scenario. At the BER of 10^{-3}, the current is no more than 260 μA_{RMS}, which is 38 dB below the amplifier's operating limit within its linear zone. This margin guarantees the use of the platform for other short-range scenarios with similar performance.

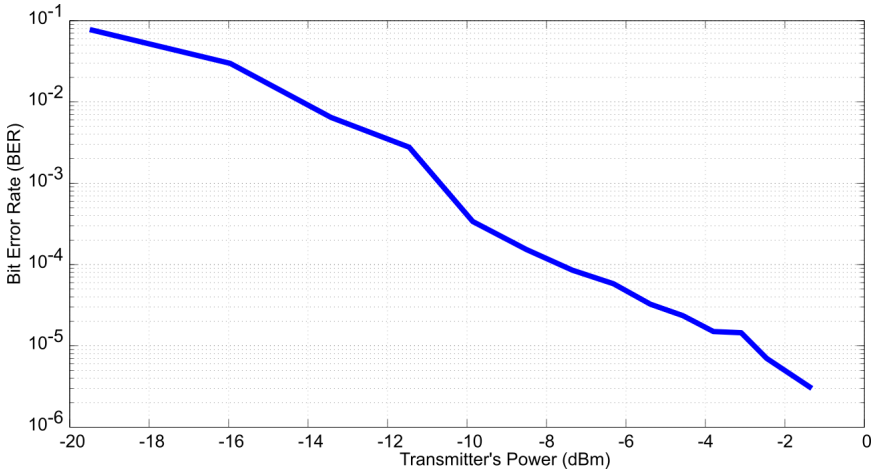

Figure 6.15: Bit Error Rate (BER) as a function of transmitter power, measured at the receiver's output and without channel coding.

6.5 DUMPING RESISTANCE

In some cases it is important to reduce the quality factor (Q) of a resonant circuit to transmit signals of larger bandwidth at the expense of reducing gain. To test the impact of Q-factor, a variable dumping resistance is added in series with the tuning circuit.

For this experiment the octagonal antenna was used as transmitter without resonant circuit coupled, and the square antenna # 1 was used at the reception end with resonance circuit tuned at 5040 Hz. In Figure 6.16 can be seen the impact on gain of adding a dumping resistance. Particularly, the use of no resistance keeps the gain around 14 dB and a bandwidth of ≈145 Hz, and on the opposite direction, when a 125 Ω is added, the gain is reduced in almost 10 dB and the bandwidth increases in 33%.

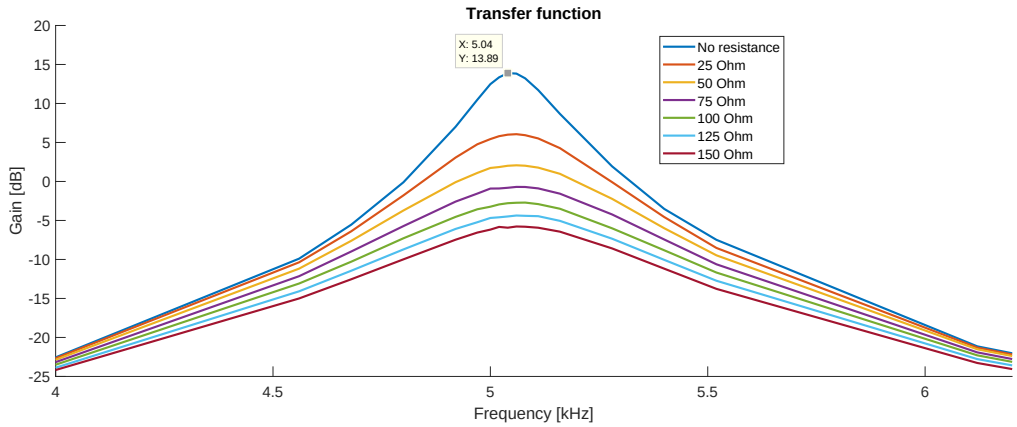

Figure 6.16: Variation of gain of square antenna # 1 as dumping resistance increases.

Similarly, Figure 6.17 shows the variation of gain and bandwidth as a function of dumping resistance.

Though the bandwidth can be increased with this addition, the use of such circuit will depend on the application. For instance, if the transmission is carried out at mid-range distances, the reception could suffer the impact of noise generated by harmonics of 60 Hz, so a larger bandwidth would be counterproductive. Nevertheless, this experiment evinces the feasibility of introducing larger bands in TTE systems.

6.6 TRANSMISSION TESTS

6.6.1 Subway expedition

In June 28th 2019 a set of measurements were carried out in the Brasilia Subway Central Station (Figure 6.18) from 00:30 to 04:30. This period was selected because it was during the maintenance shift and the electric power on rails was cut off to guarantee safety. The outdoors spot on which the tests were performed was an open grassy field above the underground station.

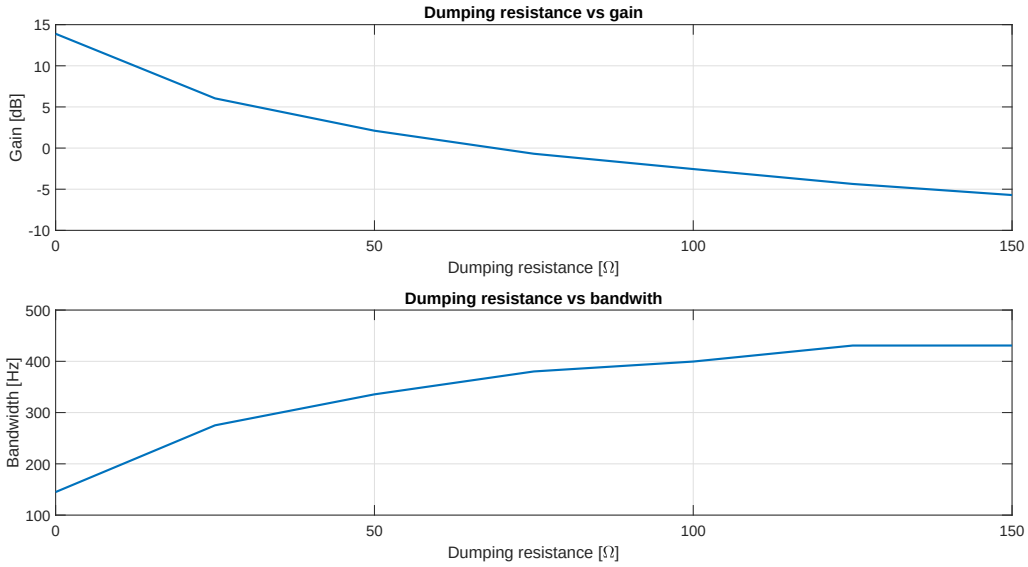

Figure 6.17: Variation of gain of square antenna # 1 as dumping resistance increases.

Figure 6.18: Geographical position of Brasilia Subway Central Station. Source: Google Maps.

Two teams were formed to execute the activities in the surface and inside the subway tunnel. The surface team was composed of one doctoral student and a master student, the underground team was composed of two professors, a master student and the subway chief technician.

Regarding the used equipment, the Square antenna # 1 was used for reception and the octagonal antenna for transmission. In addtion to the power amplifier described previously, two 12 V car batteries were used to provide the energy, to both sides independently, by using power inverters to deliver alternate voltage to all equipment.

The experiments started with a calibration test to adjust resonant circuits before carrying out

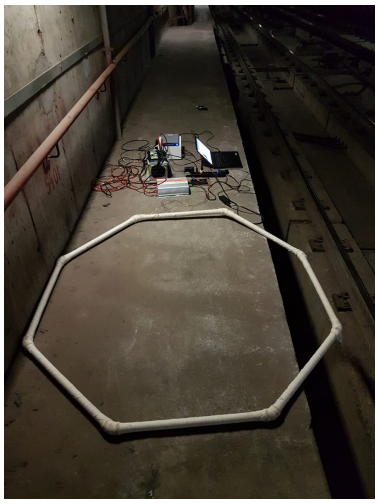

(a) Octagonal antenna used for up-link transmission.

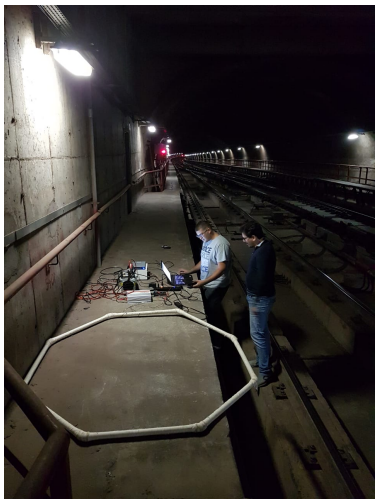

(b) Team members working on transmission.

Figure 6.19: Subway expedition photographic record.

(a) Square antenna # 1 used for up-link reception.

(b) Team members working on reception.

Figure 6.20: Subway expedition photographic record.

a BER test. Using the application presented in section 6.1, the antennas were connected properly with the following parameters:

- **Mode:** transmission and reception respectively
- **Type:** channel
- **Direction:** coaxial
- **Transmission resonance:** yes.
- **Signal amplitude:** 0.23 V.
- **Central frequency:** 5040 Hz
- **Number of CW Signals:** 24.
- **Sampling frequency:** 20 kHz.

Then, the system transfer function was estimated by transmitting a sequence of known CW signals and comparing it in FFT domain with the received signals.Figure 6.21 shows that the bandwidth available is about 114.5 Hz which could provide a transfer rate up to 229 bps. However, that available bandwidth is limited to less than 60 Hz due to the harmonics from the power lines close to the measurement site.

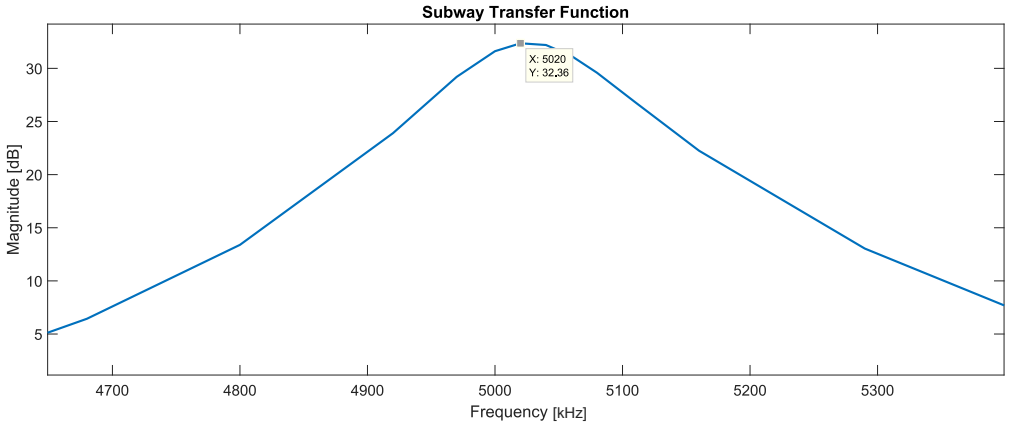

Figure 6.21: Subway System Transfer Function.

Having this information, it was decided to perform a Energy per Bit (Eb) to the Spectral Noise Density (No) Eb/No test using a bit rate of 40 bps. This low rate makes the calculations significantly slow, so only 30000 bits per amplitude are transmitted for this test. Other parameters set are: roll-off factor = 0.35, the transmission was in passband, the modulation BPSK was used, and there were no channel coding nor equalization. Figure 6.22 shows the power spectrum density of received signals for a sequence of 1000 bits, in which it is possible to realize that the system is working as a passband filter for every Eb/No value.

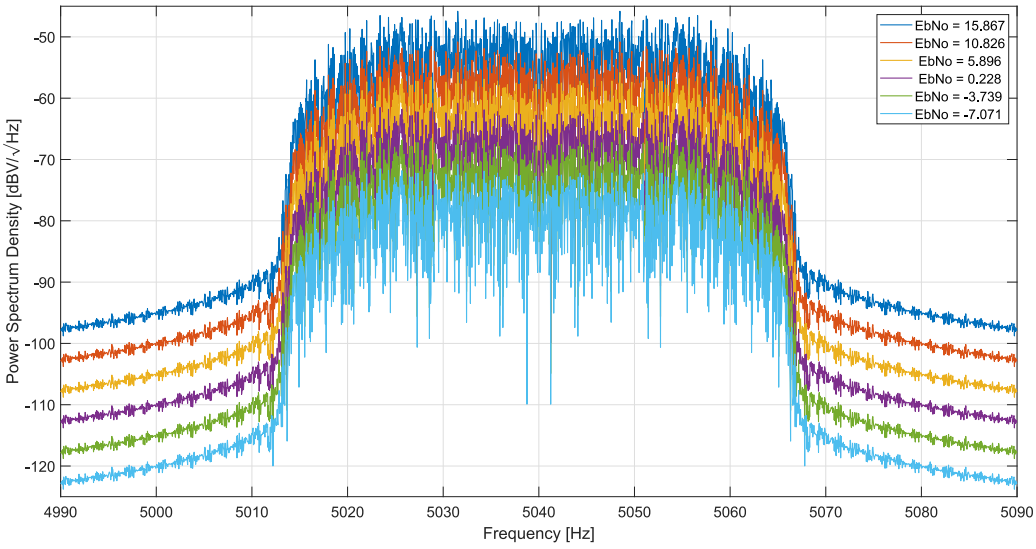

Figure 6.22: Received signal during Eb/No measurements.

The following table summarizes the relationship between the transmission power and the average measured Eb/No for every input voltage and the transmission power. It is noticeable that the Eb/No has a direct proportionality with the input voltage and consequently with the transmission power in dBm. This proves the channel and system linear behavior, which is shown Figure 6.23 for each loop of 1000 bits. Moreover, it is noticeable that the lower the SNR the bigger the Eb/No variance due to the lower precision on measurements.

Table 6.1: Relationship of energy per bit to noise power spectral density ratio with Transmission Power and input voltage (at the antenna) in the Subway Station.

Transmission Power [dBm]	**Eb/No [dB]**	**Input voltage [V]**
28.778	15.867	2.375
23.943	10.826	1.335
18.862	5.896	0.751
13.979	0.228	0.422
8.862	-3.739	0.237
3.984	-7.071	0.133

These results show that for a transmission power of about 29 dBm or 0.79 W can provide acceptable Eb/No

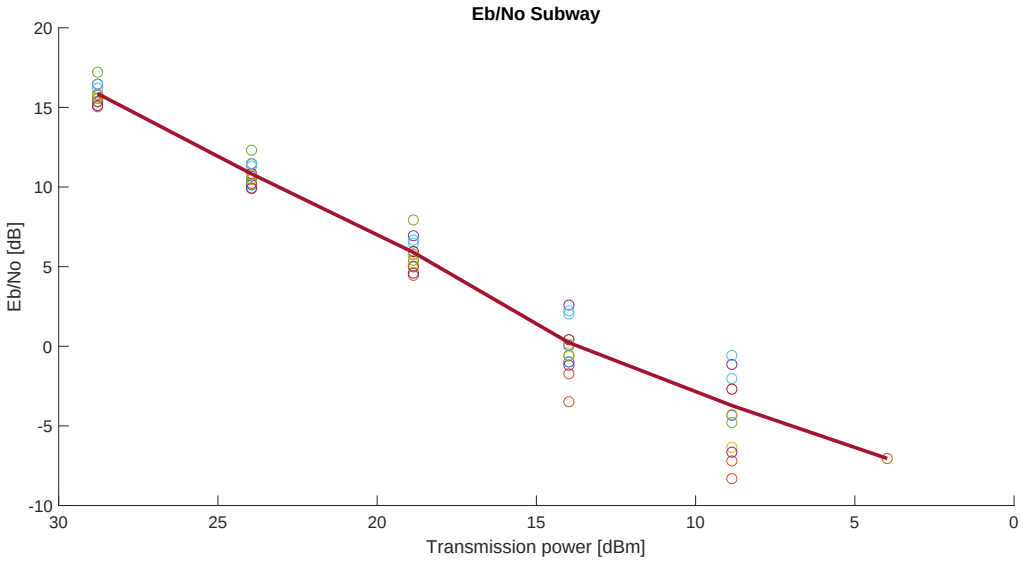

Figure 6.23: Eb/No vs Power consumption.

6.6.2 Cave expedition

In June 29th 2019 a set of measurements were carried out in the Echos Cave in Cocalzinho de Goias, Goias, Brazil (Figure 6.24) about 1.5 h by car from Brasilia, capital of Brazil. This place was chosen due to its proximity to the University of Brasilia and because it has been previously mapped by the "Espeleo Grupo de Brasilia"[1], which supported the entire expedition by taking the underground team to the measurement test area and bringing them back in safety.

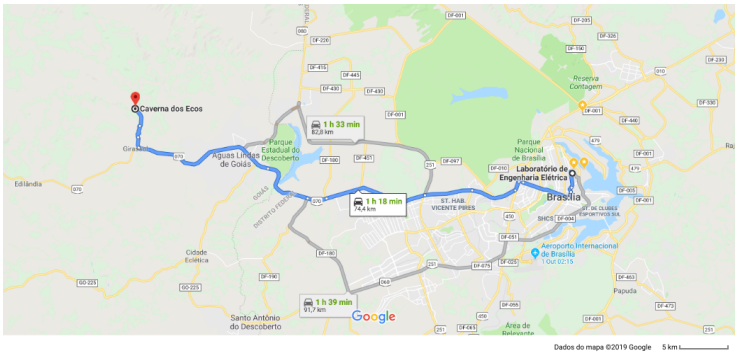

Figure 6.24: Geographical position of Echos Cave - Cocalzinho de Goias, Goias, Brazil. Source: Google Maps

Three teams were formed to execute the activities in the surface, at the cave's entrance and inside the cave. Such distribution was necessary because the alternate communication system (i.e. walkie-talkies) could not overcome the channel attenuation from the interior to the top of the cave, so a person had to provide the link between the outside and the interior. Specifically, one professor stayed at the entrance with a handheld transceiver passing the setting information between the other two teams.

[1]The "Espeleo Grupo de Brasilia" is a non-profit association formed by speleologists, geologists, biologists, paleontologist, archaeologists and other enthusiastic on speleology, that carry out expeditions to caves and other geological sites in the Federal District and its vicinity.

(a) Team members working on transmission.

(b) Octagonal antenna used for up-link transmission.

Figure 6.25: Echos Cave expedition photographic record.

(a) Square antenna # 1 used for up-link reception.

(b) Team member working on reception.

Figure 6.26: Echos Cave expedition photographic record.

The surface team was composed of one doctoral student, a graduation student and a professor and the underground team was composed of two master students and three professional speleologists.

Regarding the used equipment, the same configuration from section 6.6.1 was used, and the experiments started with a calibration test to sound the medium before carrying out a BER test. Using the FFT based spectrum analyzer built for this study, it was easier to conduct a preliminary test that transmitted a Carrier Wave at 5040 Hz to visually verify that the system was ready to perform other tests. The received sine wave is shown in Figure 6.27

Using the application presented in section 6.1, the antennas were connected properly with the following parameters:

- **Mode:** transmission and reception respectively
- **Type:** channel

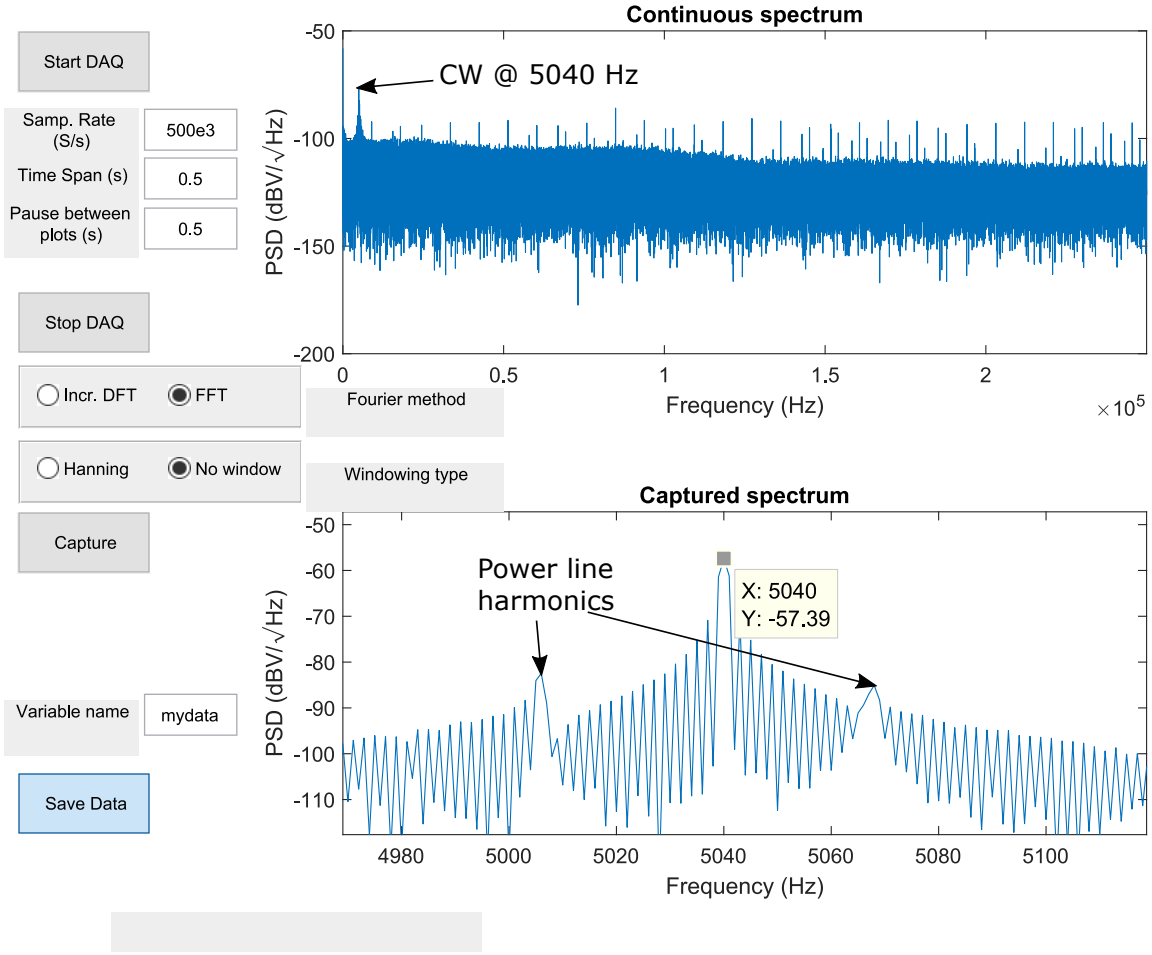

Figure 6.27: Sine wave at 5040 Hz received on the surface.

- **Direction:** coaxial
- **Transmission resonance:** yes.
- **Signal amplitude:** 0.95 V.
- **Central frequency:** 5040 Hz
- **Number of CW Signals:** 24.
- **Sampling frequency:** 20 kHz.

Then, the system transfer function was estimated. Figure 6.28 shows that the bandwidth available is about 94.70 Hz which could provide a transfer rate up to 189.41 bps. The difference on bandwidth compared to the subway expedition is probably due to mismatches of frequency resonance between transmission and reception circuits. In addition, it can be also noticed that signals suffer 82 dB extra attenuation in the cave scenario than in the subway, which shows how

near field transmission is strongly affected by the increasing of distance. In the case of quasi-static transmission it is necessary to add 18 dB of power to double the distance range.

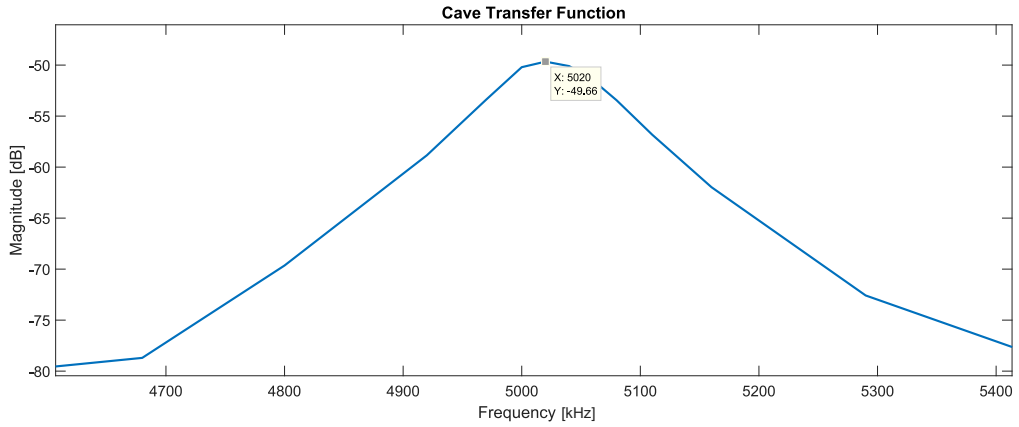

Figure 6.28: Echos cave System Transfer Function.

After getting this information, it was decided to perform a Bit Error Rate test using the same bit rate of 40 bps used in the subway tests. This low rate makes the calculations significantly slow, so it was impossible to transmit the usual 10^6 bits as made in laboratory tests. Figure 6.29 shows the power spectrum density of received signals for a sequence of 1000 bits and Figure 6.30 presents the results of BER measurements.

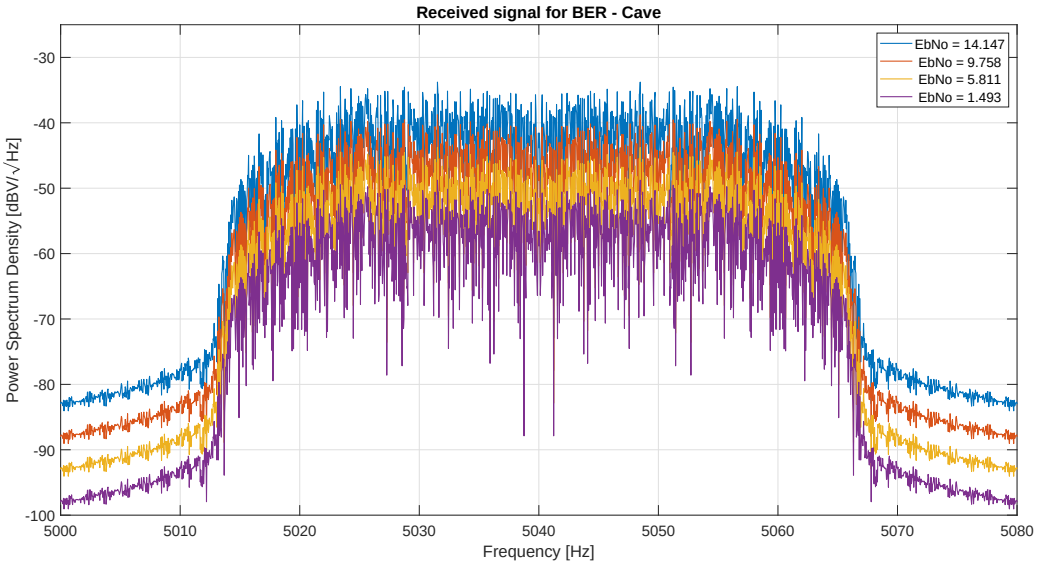

Figure 6.29: Received signal during BER measurements.

Some considerations must be added to this result: first, as the the reception end was under sunlight the car battery discharged rapidly, so the starting battery from the car was used and the motor was kept running, which might have generated extra noise. Second, the anthropic noise presented 60 Hz even and odd harmonics, which do not happened in the subway measurements where only odd harmonics were present. Third, it is clear that 30000 bits is an insufficient number of bits for an accurate BER test of 10^{-5}. Fourth, three passband filters are used in the process that

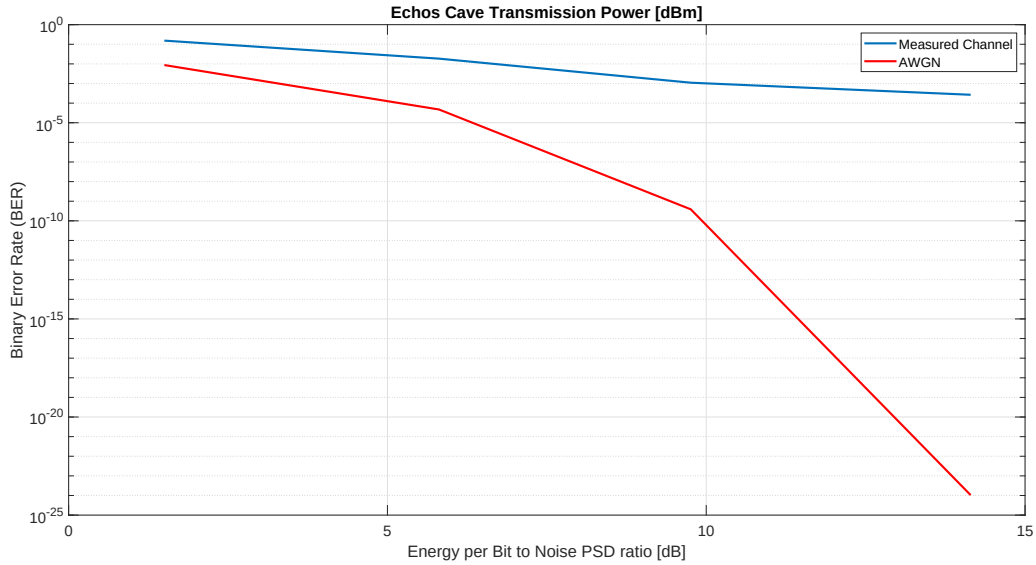

Figure 6.30: BER versus power delivered.

Table 6.2: Relationship of energy per bit to noise power spectral density ratio with Transmission Power and input voltage (at the antenna) in the Echos Cave.

Transmission Power [dBm]	**Eb/No [dB]**	**Input voltage [mV]**
42.024	14.147	9.500
37.464	9.758	5.342
32.368	5.811	3.004
27.406	1.493	1.689

may insert selective gain in frequency domain, specifically the two tuning circuits and a digital filter used at the receiver before post processing. Finally, the noise itself is not perfectly Gaussian.

Additionally, Figure 6.31 shows the relationship of Eb/No and the power consumption and the input voltage feeding the antenna, in which it is noticeable that to get an Eb/No a BER of 10^{-3} the transmission power needed is around 37.7 dBm or 5.88 W, value that is easily cover by a car battery. In theory, a 12 Volts car battery and 40 Ampere-Hour capacity could support transmission for 80 hours, assuming power transmission efficiency of 100%, and considering only 5.88 W delivered by the power amplifier. In practice, the computers used much more power than the power amplifier, but an eventual prototype with dedicated processing and ADC/DAC converters the power consumption will tend to be sustainable.

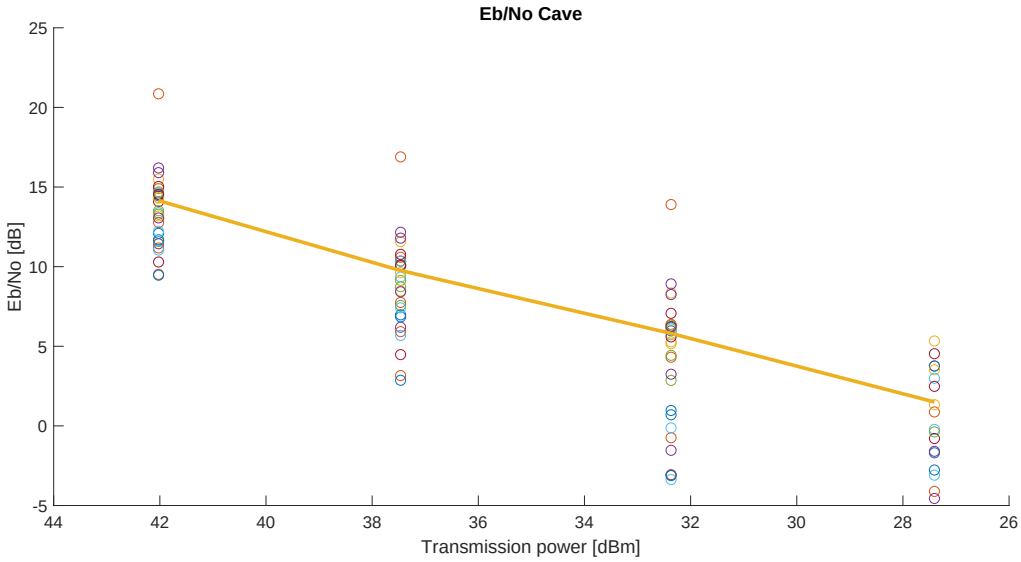

Figure 6.31: Eb/No vs Power consumption.

6.6.3 Comparison of measured and theoretical H-field intensity for Echo's cave and metro tunnel campaigns.

In order to validate the measurements at the cave and tunnel, a comparison with theoretical models was carried out. Specifically, that information from both places was compared to the following models: Quasi-Static (eq. 3.5), Wait (eq. 3.7), and Geometric Quasi-Static [76]. The latter is the Biot-Savart model for an arbitrary loop, while (3.5) is its derivation for a point source.

To build the associated plots, it was necessary to have some physical dimensions as the relative distance between the transmission and reception loops. In the case of the Echos cave, an altitude meter was used inside and outside the cave, so the result distance was the subtraction of both values, given $\approx$ 99 m and less than 1 m in the horizontal component. This measurement was accurate due to the presence of georeferenced points both inside and outside the cave as seen in Figure 6.32. In the second site, the distance estimation was carried out in a similar matter by the means of the altimeter obtaining an approximate value of 9 m for the vertical separation and 3 m in the horizontal. Beside these values, the apparent electric conductivity measured in both sites was of 10^{-3} S/m and 10^{-5} respectively, which were determined empirically, using the Homogeneous Half-Space model **HHS** from Section 3.2.2, equation (3.7)

Firstly, Figure 6.33 shows the normalized magnetic field (per volt at the transmitter) for the subway scenario, in which is possible to verify that the measured field has no considerable difference to the Geometric and Wait models and there is almost 3 dB difference to the theoretical QS model. Such dissimilarity is due to the fact that the QS theoretical model considers the source as a point and for the nominal distance of $3\sqrt{10}$ m the antenna dimensions are not negligible.

(a) Inner georeferenced point.

(b) Outside georeferenced point.

Figure 6.32: Echos Cave expedition georeferenced points.

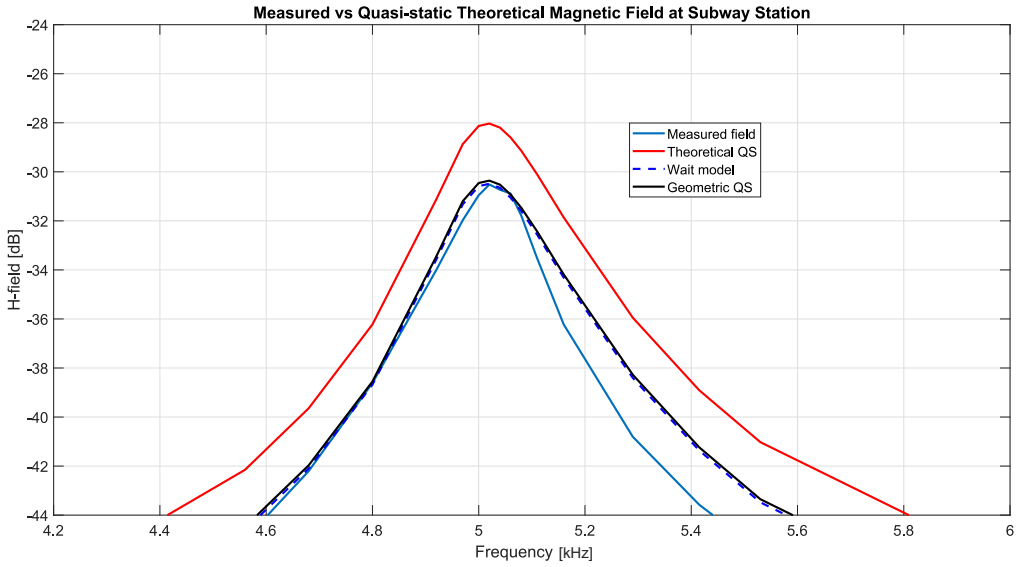

Figure 6.33: H-field intensity measured in the subway expedition compared to theoretical models.

Secondly, Figure 6.34 presents the normalized magnetic field (per volt at the transmitter) for the cave scenario, and in it is shown a close relation of the measured H-field and all models. As the distance between the antennas is much bigger than their dimensions, the effect of their sizes is mitigated. Nevertheless, the measured field presents a narrow maximum close to 5 kHz and a narrower bandwidth, attributable to mismatches in the tuning circuit associated to each antenna.

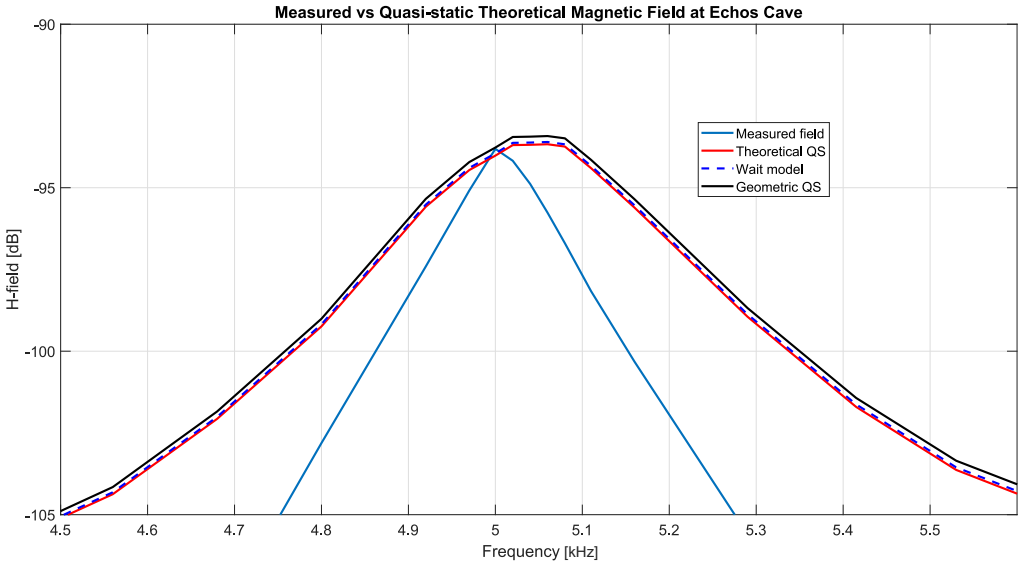

Figure 6.34: H-field intensity measured in the cave expedition compared to theoretical models.

The electric conductivity for the Wait model curves were adjusted to match the measured curves. As stated previously, the apparent conductivity values were set as 10^{-3} S/m for the cave and 10^{-5} for the subway. Such values are quite small and prove that the field attenuation is not significantly affected by soil composition as can be reinforced by the proximity of the Wait model and a free space based model such Geometric QS. Additionally, this result shows the feasibility of using magnetic fields at low frequencies to go through almost 100 meters of soil and rock as if it were air.

6.6.4 Tag to tag transmission

A testbed was planned in order to test transmission between the antennas Tag # 1 and Tag # 2, for which a 3D simulation was carried out on CST to have reference values.

6.6.4.1 Tag to tag 3D transmission simulation

First, a 3D simulation was carried out on CST considering the real sizes of the building and similar materials. Due to the global crisis generated by the Covid-19, all measurements had to be done in a adapted home laboratory, so the simulated scenario was an apartment with a long corridor in which the antennas were situated and repositioned at distances from one to 9 meters. Without losing accuracy, one antenna was simulated as a small torus with similar dimensions as the Tag # 1 and Tag # 2 (Figure 6.35). H-field probes were positioned in different position every 1 m from the antenna, in coaxial alignment, up to 9 m. The scenario around them emulates an apartment recently build out of concrete in its floor, walls and ceiling, so a concrete (one year old) material was selected from the material library on CST and can be seen in Figure 6.36. The physical characteristics are listed below on Table 6.3.

Table 6.3: Physical characteristics of one year concrete used for the tag to tag transmission.

Parameter	**Value**
Dispersive eps	1st order model (fit)
μ_r	1
Rho	2400 [kg/m^3]
Thermal cond.	1.7 [W/K/m]
Specific heat	800 [J/K/kg]
Diffusivity	8.85417e-007 [m^2/s]
Young's modulus	30 [kN/mm^2]
Poisson's ratio	0.2
Thermal expan.	13 [1e-6/K]

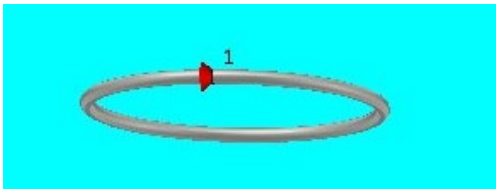

Figure 6.35: Tag antenna representation for transmission simulation.

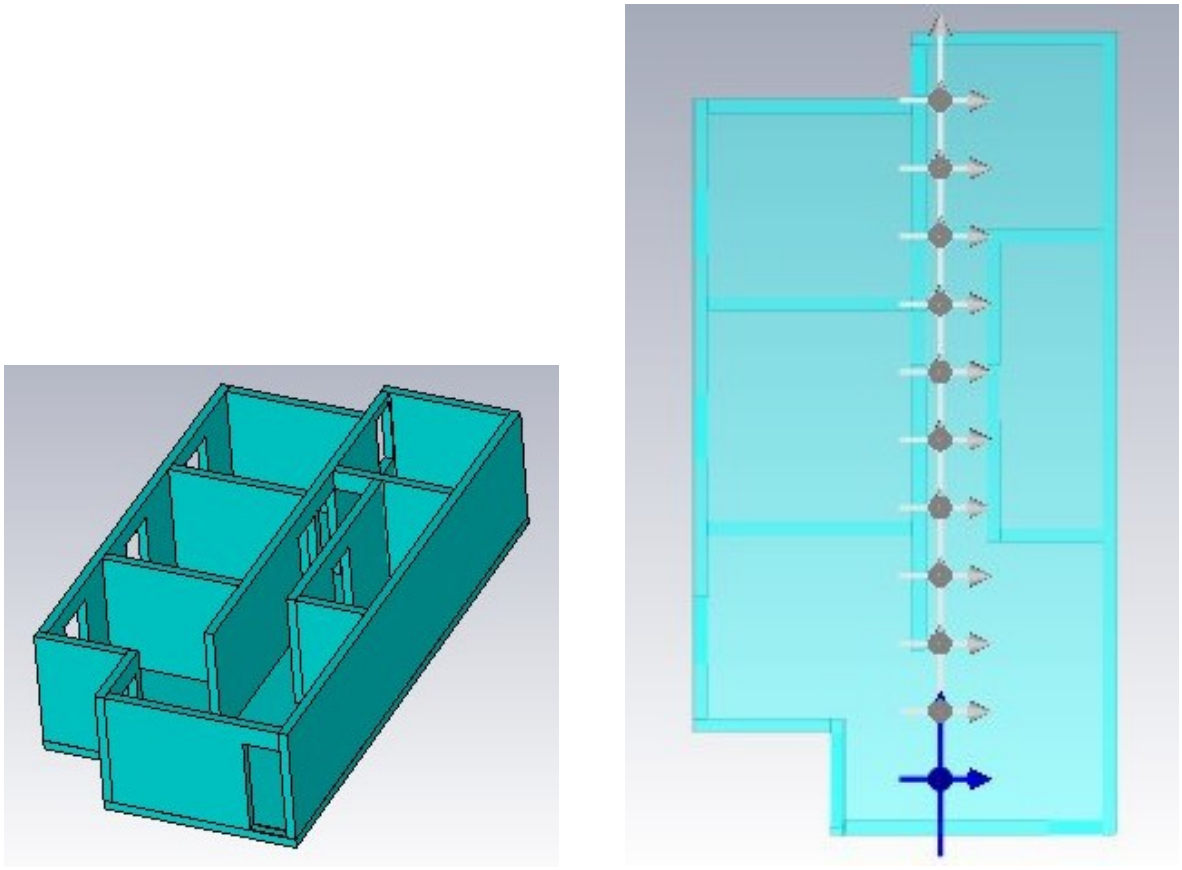

(a) 3D view of the simulated space.

(b) Probes within the simulated space.

Figure 6.36: 3D representation of the scenario in which tag to tag transmission was tested.

The magnetic field values from each measurement is shown in Figure 6.37. On that plot it is possible to observe a non-linear behavior on the magnetic field magnitude, when the double of each distance is considered, as expected for this kind of transmission.

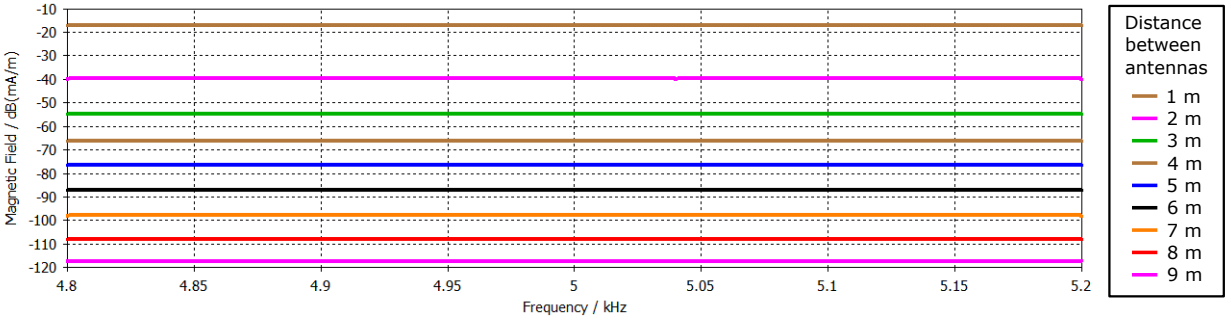

Figure 6.37: Tag antenna representation for transmission simulation.

6.6.4.2 Tag to tag transmission in situ.

Second, several measurements with both antennas were carried out with distances from 0.5 to 4 meters between them. Such smaller distance was used because there was a significant amount of noise allegedly from a construction site and three high-voltage transmission lines close to the apartment. Figure 6.38 shows a representation of the setup that uses the integrated PA, 15 m long cables to feed the signal to the transmitting antenna and to sense the received data at the receiver. These cables slightly altered the feeding and receiving circuits, so minor changes on the tuning capacitors were necessary. Such alterations were carried out using the system presented in Section 6.1.

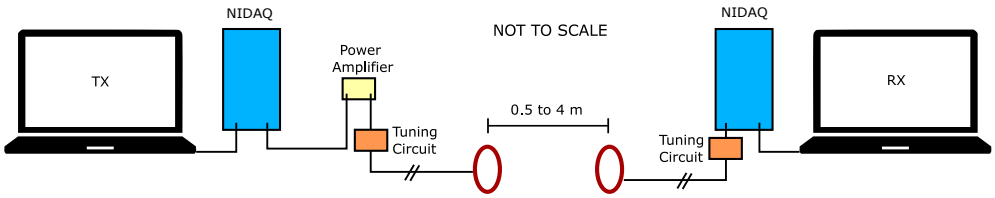

Figure 6.38: Tag to tag transmission schematic.

Multiple measurements were carried out for 0.5, 1, 2, and 4 m as shown in Figure 6.39 and 6.40 which present the FFT of the sequence of tones and the channel transfer function (magnitude). As expected, the received signal strength was reduced as distance increased.

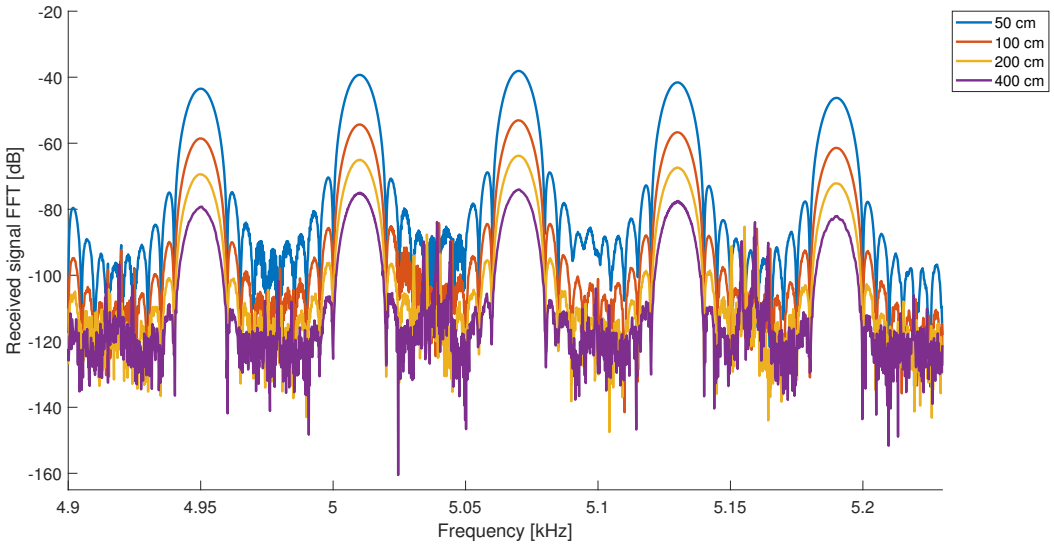

Figure 6.39: Tag to tag received signal FFT.

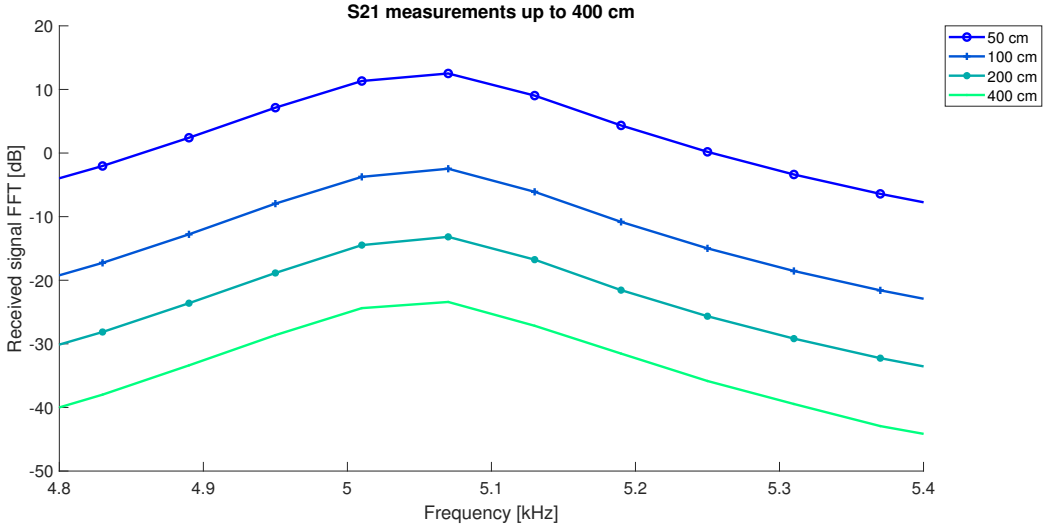

Figure 6.40: Tag to tag received signal S21.

6.6.4.3 Simulation of transmission within loamy soil.

As stated in Section 2.2, simulations for a soil similar to tailing dams were carried out using CST. This software provides a variety of materials that emulates real electrical, mechanical and thermal properties, so the loamy soil option was selected and its properties are shown in the following Table:

The simulated structure was a cube of 10 x 14 x 10 m made of loamy soil in which a small antenna, identical to the one described on Section 6.6.4.2, was positioned in the center of the structure as seen in Figure 6.41. Similarly, a H-field probe was positioned 4 m from the antenna in its axis to emulate a receiving antenna.

Table 6.4: Physical characteristics of wet loamy soil from CST.

Parameter	**Value**
ϵ_r	13.8
μ_r	1
Electric tand	0.18 (Const. fit)
Rho	1400 [kg/m^3]
Thermal conductivity	0.65 [W/L/m]

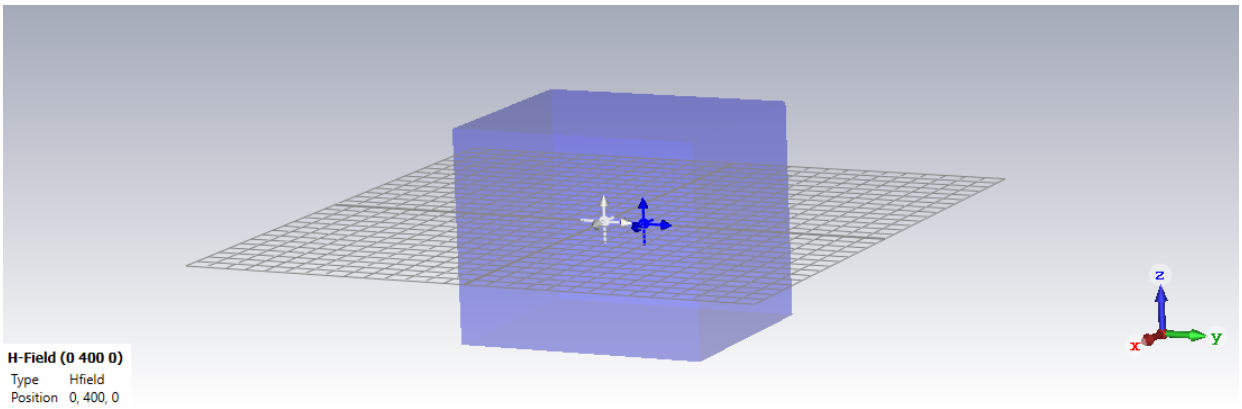

Figure 6.41: Tag to tag simulation within loamy soil.

In order to compare with a known condition, two additional scenarios were simulated one with air and other with water, whose characteristics are listed on the Tables 6.5 and 6.6.

Table 6.5: Physical characteristics of air from CST.

Parameter	**Value**
ϵ_r	1.00059
μ_r	1
Specific heat	1005 [J/K/Kg]
Rho	1.204 [kg/m^3]
Thermal conductivity	0.026 [W/K/m]
Diffusivity	2.14872 x 10^{-5} [m^2/s]

Table 6.6: Physical characteristics of water from CST.

Parameter	**Value**
ϵ_r	78
μ_r	1
Electric conductivity	1.59 [S/m]
Rho	1000 [kg/m^3]
Thermal conductivity	0.6 [W/K/m]
Specific heat	4200 [J/K/kg]
Diffusivity	1.42857 x 10^{-7} [W/K/m]

Subsequently, the magnetic field data obtain from all those simulations are presented in Figure 6.42 from which is possible to realize that the air and loamy soil scenarios are virtually identical so a soil with those characteristics do not affect the magnetic field in a significant manner.

This fact might support more research and tests on real conditions.

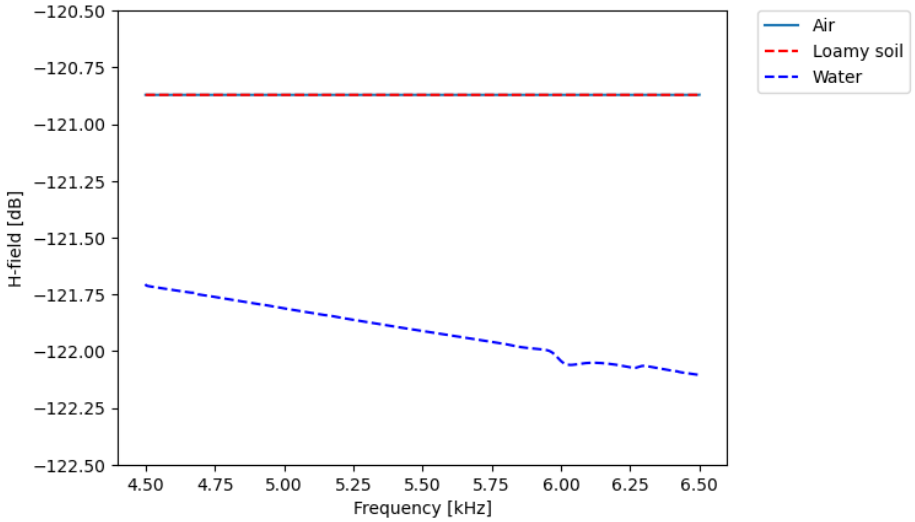

Figure 6.42: Received magnetic field within different scenarios.

Another information obtained from these results is that the same scenario changed into a watery configuration has a supplementary small loss of less than 2 dB for the entire studied frequency band. This result might be specially interesting for underwater applications such as data collection from sensors in the oil industry.

6.6.4.4 Best antenna position estimation for loamy soil transmission.

In order to identify the best depth to install the antennas for transmitting within a loamy soil, an addition simulation was carried out with a structure composed by a two layers scenario, the upper layer made of air and the lower layer made of loamy soil. Their combined dimensions are 10 m width, 14 m long and 40 m high, being the upper layer of 10 m high, and a lateral view of this structure can be seen in Figure 6.43.

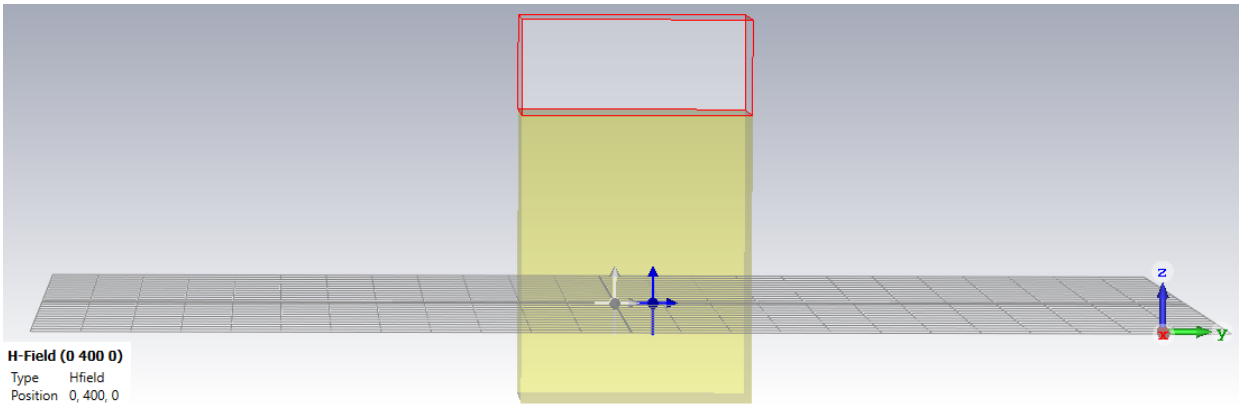

Figure 6.43: Tag to tag simulation within loamy soil (bottom) and air (top) with sweeping tag position depth.

Similarly to the previous simulation, a tag antenna and a probe were set 4 m apart from each other and positioned in a horizontal plane in such a way that both the antenna and the probe are

on the y-axis and on the origin of the x-axis, being their z position the variable parameter that was swept from zero downto -20 m with a pace of 50 cm. The following Figure 6.44 shows the antenna and probe initial positions.

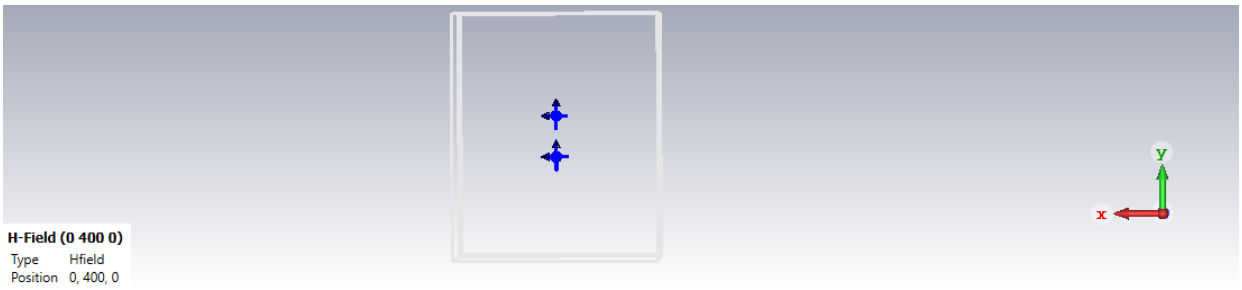

(a) X-Y view

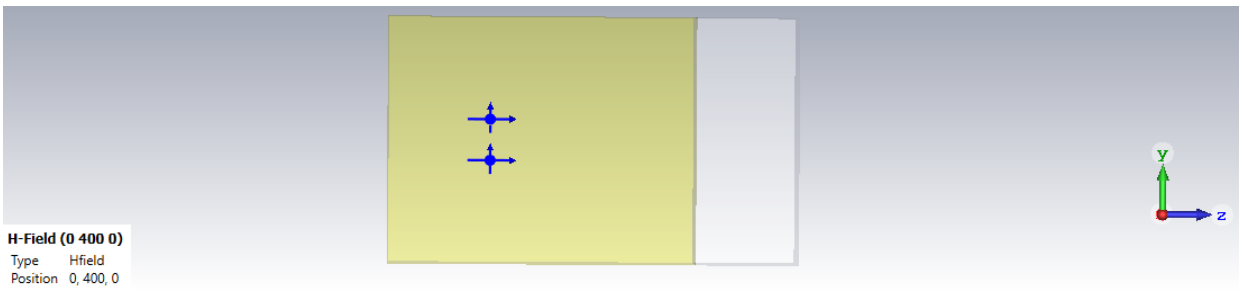

(b) Z-Y view

Figure 6.44: Detailed view on antenna and probe position within the loamy soil.

Thus, in order to determine the most suitable antenna depth, the H-field results of these simulations were compared to those from the loamy soil from Section 6.46, and the difference of them in dB are shown in Figure 6.46.

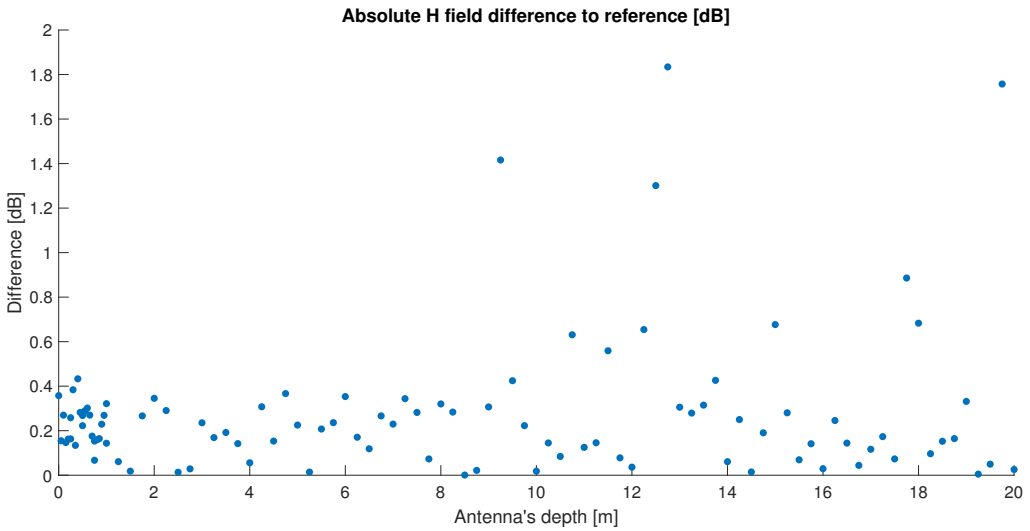

Figure 6.45: Absolute H-field difference to reference scenario.

From these results is noticeable that all measurements are below 2 dB, which gives a flexible range of positions within the soil. herefore, it is possible to infer that a sensor in the interior of

a tailing dam could transmit information without significant losses up to 20 m away. Regarding the selection of a position that is feasible to accomplish in a laboratory ambiance, a ranking of the first 45 smallest H-field differences, ordered from the smallest to the highest, is presented in Table 6.7.

Table 6.7: Absolute H-field differences for transmission within a loamy soil by antenna depth position.

Rank	**Depth [cm]**	**Absolute difference [%]**
1	850	0.0007
2	1925	0.0049
3	250	0.0135
4	525	0.0141
5	1450	0.0146
6	150	0.0183
7	1000	0.0183
8	875	0.0216
9	2000	0.0256
10	275	0.0285
11	1600	0.0291
12	1200	0.0363
13	1675	0.0443
14	1950	0.0497
15	400	0.0559
16	1400	0.0608
17	125	0.0609
18	75	0.0672
19	1550	0.0693
20	775	0.0731
21	1750	0.0732
22	1175	0.0780
23	1050	0.0844
24	1825	0.0966
25	1700	0.1166
26	650	0.1187
27	1100	0.1252
28	35	0.1341
29	1575	0.1413
30	375	0.1420
31	100	0.1438
32	1650	0.1443
33	1025	0.1449
34	1125	0.1458
35	15	0.1468
36	1850	0.1526
37	450	0.1534
38	75	0.1535
39	5	0.1547
40	80	0.1592
41	20	0.1622
42	25	0.1632
43	85	0.1644
44	1875	0.1645
45	325	0.1691

From Table 6.7 it is possible to infer that the best depth, within those tested, is 8 m; however, such depth is not feasible in the Campus due to the lack of machinery to dig a hole deep enough to position the antennas and carry out the tests. Nevertheless, depths of 150, 125 and 75 cm present small differences and are small enough to be reached with simple tools that are available and accessible. Thus, in the event of a future test, those depths are the ones suggested to be used.

6.6.4.5 Tag to tag underwater transmission

After collecting the results from the simulations on a loamy soil, it was decided to test a more challenging scenario by changing the conductive medium from a loamy soil to an underwater configuration. Due to Covid-19 restrictions, it was impossible to carry out such tests inside the campus, so it was necessary to find a place to carry out them. Professor Braga arranged a place in his family's croft in Brazlandia, a rural town not far from the University, as can be seen in the following figure:

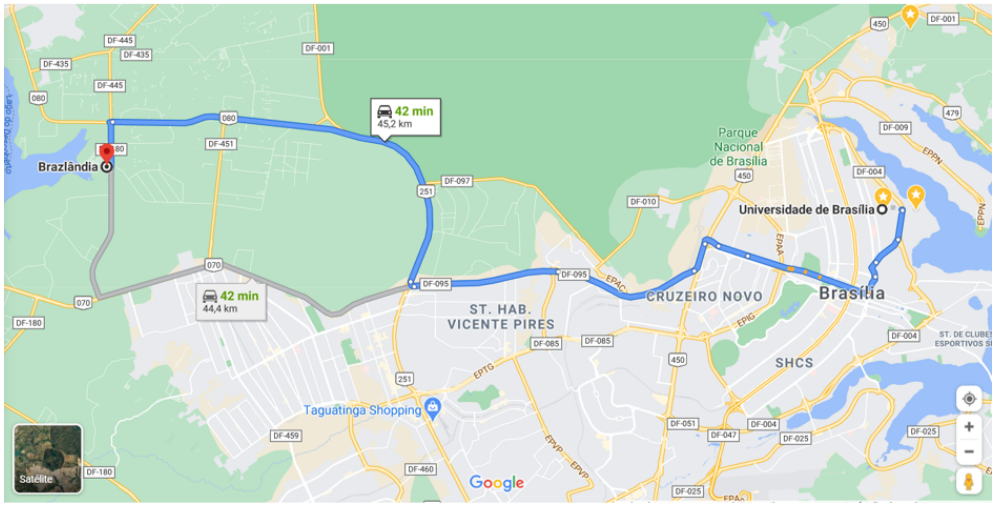

Figure 6.46: Croft's location related to the University of Brasilia.

In order to accomplish this task, a portable setup was planned as is shown in Figure 6.47. This setup is composed of two data acquisition units, two laptops, a voltage generator, the integrated PA, two resonance circuits and the two antennas. Additionally, as this setup must be portable, a power inverter and a 12 V car battery was included to power-up the entire system, along with an extra emergency backup battery.

Following the simulation results, a trench shaped as a parallelepiped with dimensions of 1 m wide by 4 m length and 1 m depth was dug and filled with water up to 90 cm to avoid collapse. Then, the antennas were placed inside it at 65 cm from the water surface and protected from moist by PVC pipes of 1.5 m length and a diameter of 100 mm, which was wide enough to house the antennas within their cases, and with one of its ends closed by a drain cap. The distance between the antennas was set to four different separations: 50 cm, 1 m, 2 m and 4 m and Figures 6.48 to 6.49 show the testing process being performed.

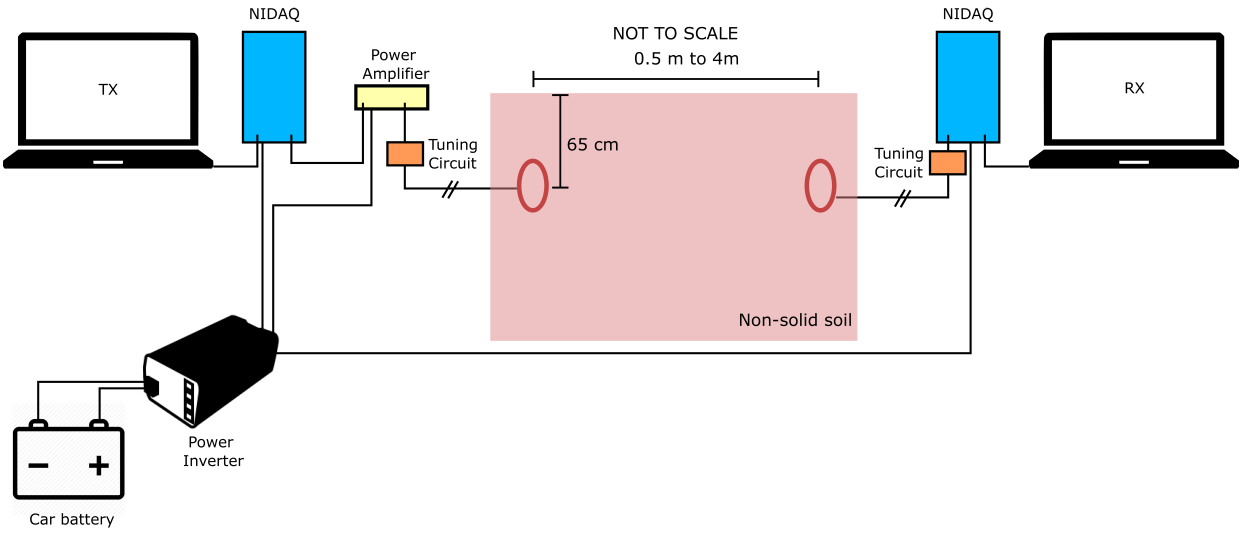

Figure 6.47: Tag to tag equipment configuration for transmission within non-solid environments.

(a) Trench filling up with water.

(b) Trench prepared for testing.

Figure 6.48: Underwater measurements - Scenario setting.

(a) Open space test configuration.

(b) Underwater test configuration.

Figure 6.49: Underwater measurements.

In order to have reference values, tests in open space were carried out using the same configuration as those within the trench. The results of these measurements are shown in Figures 6.50 and 6.51.

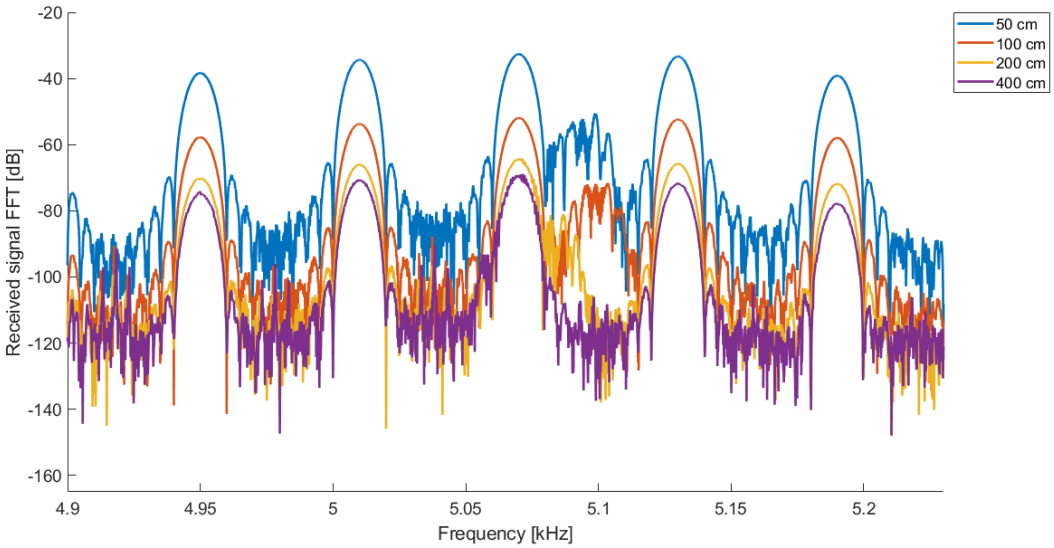

Figure 6.50: Tag to tag received signal FFT in the open space scenario.

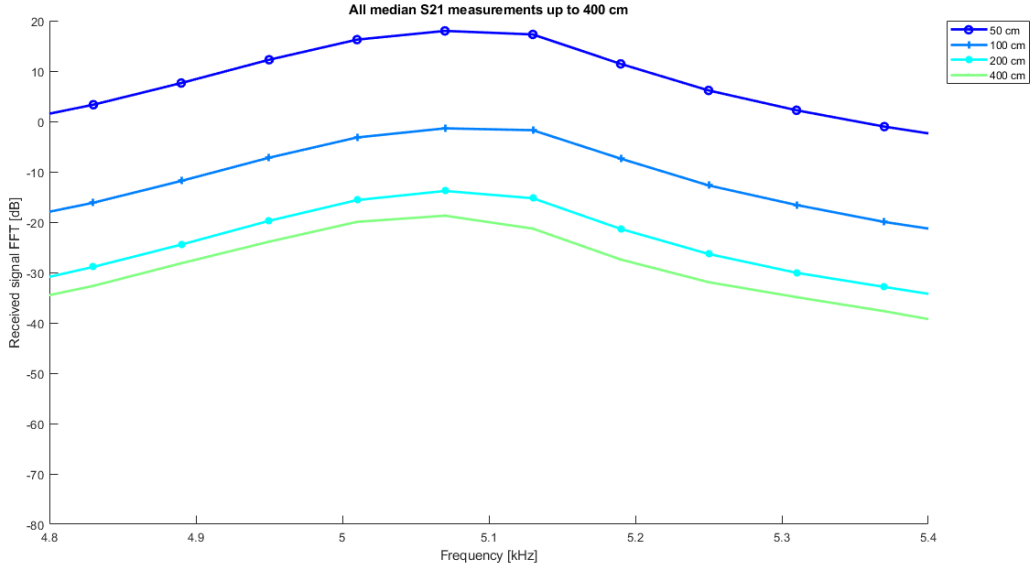

Figure 6.51: Tag to tag received signal S21 in the open space scenario.

Afterwards, the underwater transmission was performed for the different distances and the signal received as shown in Figures 6.52 and 6.53.

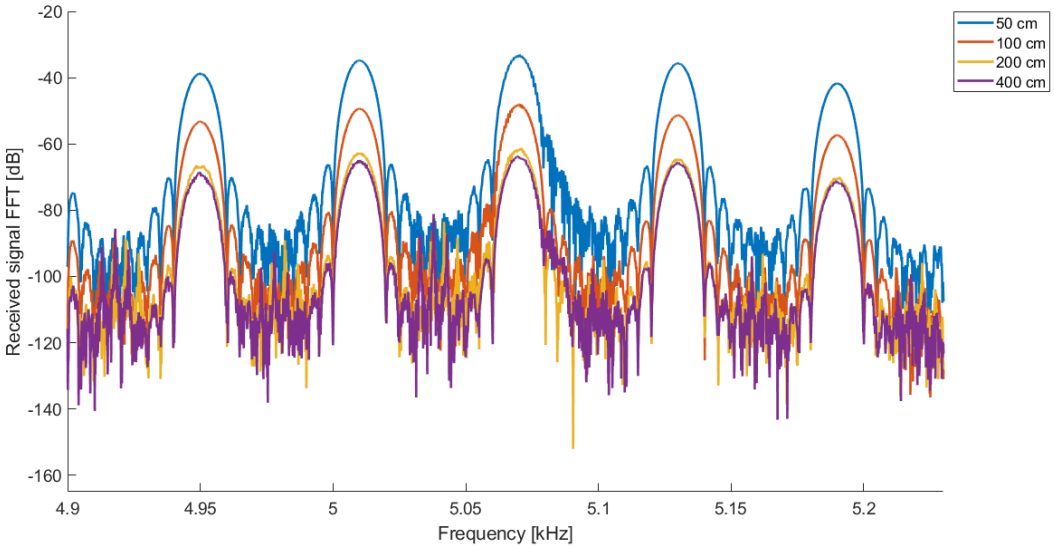

Figure 6.52: Tag to tag received signal FFT in the underwater scenario.

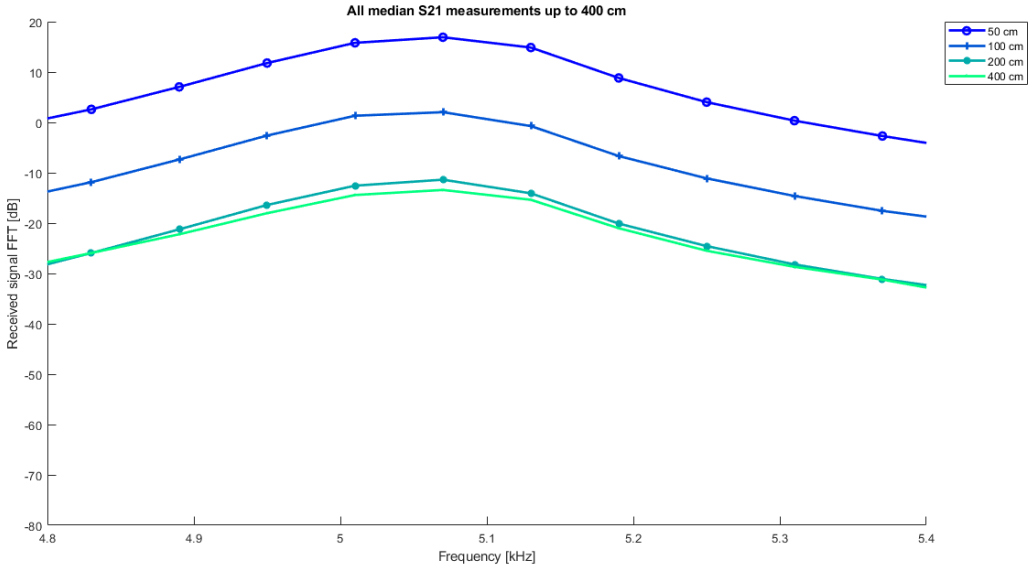

Figure 6.53: Tag to tag received signal S21 in the underwater scenario.

Finally, Figure 6.54 shows the comparison of the S21 values from the open space and underwater scenarios. From these results it is possible to infer that for short distances (up to four meters) both scenarios do not present significant differences, being close to zero for some frequencies and some distances. Thus, it is feasible to assume that underwater transmission is not significantly different from an open space transmission for frequencies from 4.8 to 5.6 kHz and separation between the antennas up to 4 m. These results are promising and could be the starting point for future research that could bring more transmission methods for applications as tailing dams and underwater pipes in the oil industry.

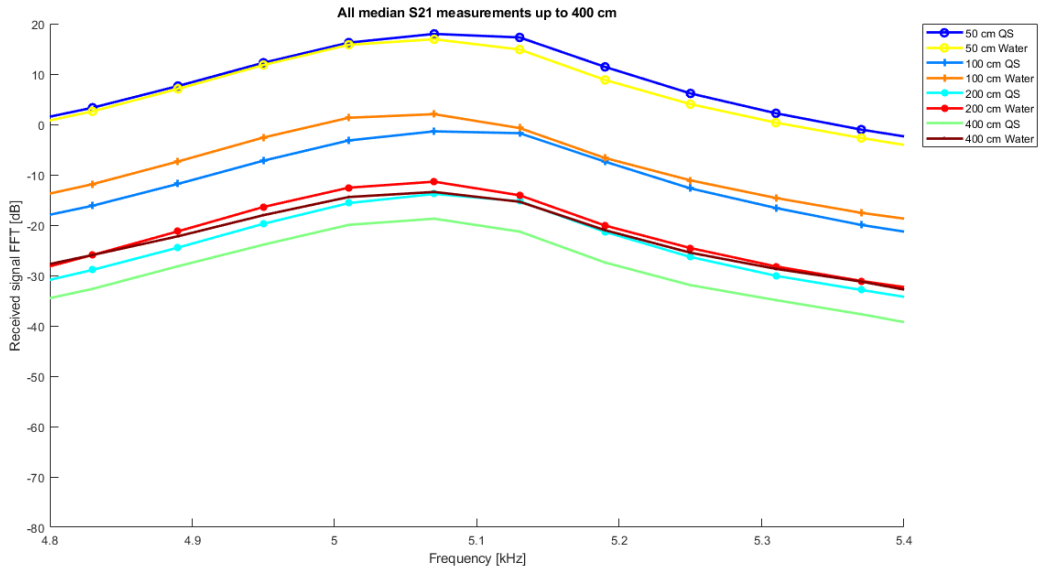

Figure 6.54: Tag to tag received signal S21 comparison of open space and underwater transmission.

7 LIST OF PUBLISHED ARTICLES

Pena Carreno, J. D. & De Barros Braga, A. J., Stochastic Generation of Subsurface Profiles for Realistic Simulation of Through-the-Earth Communication Systems *International Journal of Antennas and Propagation, Hindawi*, **2019**, 2019, 6361218

Pena Carreno, J. D.; Noll Barreto, A. & Braga, J. Propagation loss and apparent conductivity models for through-the-earth communication in sedimentary soil *IET Microwaves, Antennas & Propagation,* **2019**, 13, 1382-1388.

Mendes, H. B. S.; Braga, A. J.; Carreno, J. D. P.; Barreto, A. N.; Aguayo, L. & Garcia, L. G. U. Experimental platform for through-the-earth communication, *12th European Conference on Antennas and Propagation (EuCAP 2018)*, **2018**, 1-5

Braga, A.; Barreto, A. N.; Aguayo, L.; Maeda, G.; Pita, T.; Mendes, H. & Carreño, J. Medição e caracterização de ruído para simulador de enlace de comunicação TTE, *XXXVI Simpósio Brasileiro de Telecomunicações e Processamento de Sinais*, **2018**.

Carreño, J.; Aguayo, L.; Braga, A. & Barreto, A. N. Modelo Empírico-Estatístico de Canal para Comunicações em Minas Subterrâneas *XXXIV Simpósio Brasileiro de Telecomunicações e Processamento de Sinais*, **2016**

Sousa, L.; Carreño, J.; Neves, S.; Barreto, A. N.; Braga, A. & Aguayo, L. Sistema de comunicação através-da-terra usando codificação de resposta parcial *XXXIV Simpósio Brasileiro de Telecomunicações e Processamento de Sinais*, **2016**.

8 CONCLUSION

The Through-The-Earth communication system is an alternative to wired underground mining systems, especially in situations where humans get trapped underground as a result of tunnel burials that prevent wired underground connections to the surface. Another application of TTE systems is the activation of explosives, the automation of underground mining equipment and localization of buried sensors.

Wireless communication imposes severe restrictions on the communication system, so to mitigate the effects of soil attenuation in underground environments the use of low frequency signals is essential. The electrical characteristics of the soil enhance this attenuation; therefore, having the same environmental information facilitates the process of planning the communication structure for underground mines. As demonstrated in this thesis, the **TS** and **HHS** theoretical models do not correctly describe magnetic field propagation with a variety of media.

Magnetic field is affected in depth and frequency in TTE stratified communication environments. The H-field is affected to a lesser extent by short distances, where the frequency (0.1 to 10 kHz) does not significantly affect the communication link. For other depths, the frequency introduces more variation from field H to different mining sites, as well as greater signal attenuation.

For equivalent conductivity, according to the **TS** model, the equivalent conductivity is higher for lower depths due to the presence of highly conductive elements. However, according to the simulations presented in the previous chapter, in scenarios where no **TS** was predicted, the equivalent conductivity retained higher values for shallow depths.

The proposed empirical model of H-field median may give a reasonable direction for the calculation of link budget in TTE communication in coal mines. When compared to deterministic models, the empirical model in (4.1) suits better the median attenuation of simulated and measured data. Compared to models based on statistics of apparent conductivity, the proposed model is valid for a greater span of frequencies and not only for the four frequencies in [44]. Besides, it considers the channel variability for the optimum frequencies, which is not possible in [42] and [43]. Regarding the variation of magnetic field, for smaller depths the variance among trials is larger despite the lower overall attenuation.

For deeper positions, the attenuation becomes more severe at higher frequencies as field moves from transition zone to far field. In regard to the CDF of propagation loss, it is observed that for 300 m depth, which is the worst case condition, there is an additional loss of 16 dB for the scenario with cumulative probability of 95% compared to the scenario with 5% of cumulative probability. The variance, that may be seen within data collected at the optimal frequency for each trial, is smaller than that seen for all possible field values at frequencies higher than the optimum. Such smaller variation augments the predictability of the link budget in a TTE communication even though, in praxis, it also depends on atmospheric and man-made noise conditions at each site.

The study of electromagnetic noise levels at surface and underground as in [60, 9, 70, 77] may be used in conjunction with the proposed model to compute the median and the limits of the link budget used for communications in coal mines through vertical-axis transmission. The model presented here used 150 independent data points to achieve a RMSE of 3.7 dB, while choosing randomly any combination of only 10 trials the RMSE is always below 5 dB. Despite the estimation of median of field intensity could converge with much less trials than 150, the variability analysis from the discrete CDF would be impaired with few samples of propagation loss. The modeling process used here can be applied not only to mines of coal, but to any sedimentary structure. In such cases, statistical characteristics of soil extracted from magnetic field measurements in different sites may be used to tune the simulations to new conditions.

As discussed in previous chapters, ground electrical conductivity can be an important parameter to consider when transmitting signals through the earth. For an arbitrary mine configuration, after estimating the distance between the two ends and the frequency, it is possible to use the empirical H field equation presented in this thesis to predict the median of the magnetic field received by mines with similar soil characteristics to those of coal. With this information, all transmitter and receiver parameters can be adapted for effective communication.

Respecting antenna design, five different antennas were built and tested showing the applicability on TTE communication for short to mid distances. It is important to emphasize that all the antennas are simple to build, reproduce and test, opening the possibility of building a commercial product that can be sell primarily to the mining industry and to other areas that work in underground environments.

Regarding available bandwidth for TTE communication, it is possible to augment the bandwidth of an antenna by adding a restive circuit or dumping resistance. This insertion brings a larger bandwidth and reduces the maximum gain, so its utilization depends directly on the application. Nonetheless, as the reception end presents vulnerability to 60 Hz harmonics, the use of dumping resistances must be carefully evaluated.

In regard to magnetic field noise, measurements carried out in different spots in the city of Brasilia, Brazil, were presented to study the transmission quality in a TTE scenario. It was observed that the noise level varies with direction, time and place, and can be dominated by atmospheric noise, harmonic noise or noise coming from close-by machinery. According to equation (6.2) and considering only the noise floors for each of the curves in Figure 6.15, the measured noise temperature, normalized by the temperature of thermal noise, was, in 5 kHz, 193 dB for NR, 207 for CO and 215 for RU. The high value in RU shows that the atmospheric noise coming from distant sources was not dominant in the total noise composition, and that the number and power of machinery close to the measurement spot can greatly influence the noise level. Observing Figures 6.8 to 6.15, it is possible to notice that the data transmission quality in a TTE channel heavily depends on the impulsive atmospheric component and power line harmonics component, even if these terms have lower values. Regarding the influence of the transfer function of the TTE channel, for great depths, its bandwidth is relatively large around its optimum frequency. In prac-

tice, the bigger challenge in TTE communication is achieving desirable Eb/No levels, given the high attenuation in the conductive medium, which normally obliges to work on small bandwidths utilizing resonance circuits in the transmitter.

Additionally, a platform for channel sounding and digital transmission in short to mid range TTE scenarios was presented. The proposed method showed the feasibility of observing some characteristics of the TTE channel and predict and mitigate some of its effects. During the tests, capacitors were coupled to the antenna to study the resonance effect, adding 57 dB of gain in the transmission chain without any active or ohmic component. Tests for short and mid distances were carried out with different characteristics. Signal bandwidth for short distance (in University Restaurant - RU) were 300 Hz while only 50 Hz for Subway and Cave expedition. The favorable conditions at the university permitted to better control time measurement, more precise BER curves in presence of more background noise, harmonics and linear distortion.

For short distance transmission at the RU scenario, it is important to notice the presence of five strong harmonic components within the transmission bandwidth of the digital signal and the linear distortions due to the channel and resonance circuit, resulting in a non AWGN channel. Since signal bandwidth is twice as much the system bandwith, channel estimation and ZF equalization proved to be essential to achieve reasonable levels of system performance, assessed by measuring BER without channel coding or any technique to mitigate the harmonic components. The results proved the feasibility of TTE communication at short distances with relatively low power, in the order of -11 dBm for 4.5 m range, with potential applications where buried assets may be connected to transceivers fed by small and long-life batteries. Similarly, for distances up to 100 m, it is possible to establish a TTE communication link using as low power as 32 dBm to obtain a BER of 10^{-3}. Further test using different data rates and high-order constellations can be performed using the same experimental platform.

This platform is prone to be affected by 60 Hz harmonics generated by high voltage power lines close to the transmission site, fact that introduces band limitations because such noise could compromise the received signal at mid-distances from the source. The solution found for this situation is to use a narrow band for data transmission, even though the transmission rate is reduced significantly to around 40 bps. The inclusion of line codification might increase this rate and should be tested.

Originally, the measurement campaigns were carried out to validate propagation models developed during the doctorate; however, with time the project expedition capability resulted to be limited to mid range transmissions in few sites, not for the range itself since the platform is able to transmit up to 500 meters, but for the logistic for expeditions of higher range and especially the difficulty to find as many available sites. As discussed before, for the cave campaign with 99 m transmission the estimated equivalent conductivity is about 0.001 S/m which is much smaller value than that (0.03 S/m) computed by equation (4.5). Undoubtedly, a single measurement is not expected to fit on a median curve, as several measurements at distinct sites should be performed to qualitatively evaluate the model.

Regarding the use of TTE communication for wireless sensor networks, that supervise structures as tailing dams, the simulations presented in this work suggest that the transmission from within a loamy soil do not have significant attenuation when compared to an open space scenario for frequencies from 4.5 to 6.5 kHz and distances up to 20 m. Additionally, transmission tests inside an aqueous environment with separation between the antennas up to 4 m and frequency up to 10 kHz, suggest that the water inserts a low attenuation up to 2 dB in the 4.5 to 6.5 kHz band, which could be small enough for underwater applications, specially in the oil extraction industry. Though these results are promising, they must be reassured with further experimental tests.

8.1 FUTURE WORK

TTE communication is a field that has not been extensively studied, therefore there are several topics that can be researched after the present work. Among those topics are the following:

- Implement the Lincan model from section 3.2.4, use data from the Monte Carlo simulations to feed the simulator and compare the results to the median model proposed in here.
- Antennas, transmission/reception circuits and impedance matching circuits: it is necessary to improve the research on high sensibility antennas or magnetic sensor inside conductive medium and all circuits related to them.
- Design and build three axis tag loop antennas to provide more reliable connection using them as transmitters from the interior of an underground environment.
- Localization techniques based on multi-sensor networks: this application is vital for sensing mine status prior disasters and after any emergency situation where miners are trapped. By using small tags as those proposed in this thesis, it is possible to provide a new wearable system for miners and people living close to a mine or a failings dams.
- Reformat the software used for transmission and reception to improve its performance and reliability.
- Implement different modulation schemes as QPSK, 8PSK or 16QAM and line codification to improve the data transmission rate.
- Carry out tests on soils similar to the one found in tailing dams to prove the viability of using TTE transmission to transfer information from sensors located in interior.
- Implement waterproof and impact-resistance cases for the antennas that may be buried in tailing dams.

BIBLIOGRAPHICAL REFERENCES

1 ADMINISTRATION, O. S. . H. *Electromagnetic Radiation: Field Memo*. Accessed: 2015-02-22. Available at: <https://www.osha.gov/SLTC/radiofrequencyradiation/electromagnetic_fieldmemo/electromagnetic.html#section_6>.

2 CARRENO, J. D. P. *Channel modeling for through-the-earth (TTE) communication systems*. 117 p. Dissertação (Mestrado), 2016.

3 MINERAL, D. N. de Produção. *Código de Mineração - Capítulo I das Disposições Preliminares*. Http://www.dnpm-pe.gov.br/Legisla/cm_01.htm. Accessed: 2015-04-22. Available at: <http://www.dnpm-pe.gov.br/Legisla/cm_01.htm>.

4 GIBSON, D. *Channel Characterisation and System Design for Sub-Surface Communications*. Tese (Doutorado) — University of Leeds, Feb. 2003.

5 YAN, L. *Measurements and modeling of the electromagnetic fields in Through-The-Earth (TTE) wireless communications*. Tese (Doutorado) — University of New Mexico, 2014.

6 CARRENO, J. D. P. et al. Modelo empírico-estatístico de canal para comunicações em minas subterrâneas. In: . [S.l.: s.n.], 2016.

7 WAIT, J. R. Electromagnetic induction technique for locating a buried source. *Geoscience Electronics, IEEE Transactions on*, v. 9, n. 2, p. 95–98, Apr. 1971. ISSN 0018-926X.

8 WAIT, J. R.; SPIES, K. Subsurface electromagnetic fields of a circular loop of current located above ground. *Antennas and Propagation, IEEE Transactions on*, v. 20, n. 4, p. 520–522, July. 1972. ISSN 0018-926X.

9 HILL, D.; WAIT, J. *Theoretical noise and propagation models for through-the-earth communication.* [S.l.], 1982.

10 L., H. H.; M., M. J. *Introductory mining engineering*. [S.l.]: John Wiley, 2002.

11 HEM, P.; CALDWELL, J. *Block Caving*. Accessed: 2015-01-04. Available at: <http://technology.infomine.com/reviews/Blockcaving/welcome.asp?view=full>.

12 PRESS, A. *September U.S. Mine Inspections Result in 133 Citations*. 2015. Accessed: 2015-11-5. Available at: <http://wvpublic.org/post/september-us-mine-inspections-result-133-citations>.

13 RATCLIFFE, M. *Anglo American shares fall as miner completes sale of Norte copper mine after commodities fall hits profits*. 2015. Accessed: 2015-10-01. Available at: <http://www.cityam.com/224250/anglo-american-completes-sale-of-norte-copper-mine-after-commodities-fall-hits-profits>.

14 VICK, S. *Planning, Design, and Analysis of Tailings Dams*. BiTech, 1990. ISBN 9780921095125. Available at: <https://books.google.com.br/books?id=kqDuAAAACAAJ>.

15 HANZEN. *Mineral Beneficiation*. Available at: <https://www.hazenresearch.com/capabilities/mineral-beneficiation?gclid=Cj0KCQiAqo3-BRDoARIsAE5vnaJGDRvCDFA6mds_8pV08HWhCuT3OwarTiZTLPeVbgdzoHEGm5T7axoaAuAFEALw_wcB>.

16 GEOKON. *Earth dam instrumentation*. Available at: <https://www.geokon.com/content/posters/Earth_Dam_Poster_LARGE.jpg>.

17 HAJDUK, E. L.; PAIKOWSKY, S. G. Performance evaluation of an instrumented testpile cluster. In: *ASCE Geotechnical Special Publication*. [S.l.: s.n.]. p. 124–147.

18 MINING3. *Autonomous sensors monitoring tailings dams and spoil dumps*. Available at: <https://www.mining3.com/research/autonomous-sensors-tailings/>.

19 WICKS, B. *Autonomous Sensors for Monitoring Spoil Dumps and Tailings Dams*. Available at: <https://www.acarp.com.au/abstracts.aspx?repId=C26032>.

20 RAAB, F. H.; JOUGHIN, I. R. Signal processing for through-the-earth radio communication. *Communications, IEEE Transactions on*, IEEE, v. 43, n. 12, p. 2995–3003, 1995.

21 YARKAN, S. et al. Underground mine communications: A survey. *Communications Surveys Tutorials, IEEE*, v. 11, n. 3, p. 125–142, rd 2009. ISSN 1553-877X.

22 (UNDERGROUND), A. M. T. *MAGNETO MINE TELEPHONES*. 2012. Http://www.britishtelephones.com/ atm/atmtel6.htm. Accessed: 2015-04-15. Available at: <http://www.britishtelephones.com/atm/atmtel6.htm>.

23 ATM MINING TELEPHONES (UNDERGROUND). 2014. Accessed: 2014-09-30. Available at: <http://www.britishtelephones.com/atm/atmtel6.htm>.

24 AGGARWAL, R.; MOORE, P. Digital communications for protection. iii. fibre optics. *Power Engineering Journal*, v. 8, n. 5, p. 241–246, Oct. 1994. ISSN 0950-3366.

25 BANDYOPADHYAY, L.; CHAULYA, S.; MISHRA, P. Wireless communication in underground mines. *RFID-Based Sens. Netw*, Springer, 2010.

26 ASSOCIATION, T. I. *Fiber and cabling*. Available at: <https://www.tiaonline.org/industry-priorities/transforming-infrastructure/fiber-cabling/>.

27 CONTROL, C. for D.; PREVENTION. *Advanced Tutorial on Wireless Communication and Electronic Tracking: Communication System Performance*. Accessed: 2014-05-12. Available at: <http://www.cdc.gov/niosh/mining/content/emergencymanagementandresponse/commtracking/advcommtrackingtutorial2.html>.

28 SAFETY, N. I. for O.; HEALTH. *Tutorial on Wireless Communication and Electronic Tracking Part 1: Technology Overview*. 2010. Http://www.msha.gov/techsupp/PEDLocating/WirelessCommandTrack2009.pdf. Accessed: 2015-04-22. Available at: <http://www.msha.gov/techsupp/PEDLocating/WirelessCommandTrack2009.pdf>.

29 PATRI, A.; NAYAK, A.; JAYANTHU, S. Wireless communication systems for underground mines–a critical appraisal. *International Journal of Engineering Trends and Technology (IJETT)*, v. 4, n. 7, p. 3149–3153, 2013.

30 FOROOSHANI, A. et al. A survey of wireless communications and propagation modeling in underground mines. *Communications Surveys Tutorials, IEEE*, v. 15, n. 4, p. 1524–1545, Mar. 2013. ISSN 1553-877X.

31 EXCHANGE, P. S. *Transverse Magnetic (TM) and Transverse Electric (TE) modes*. Accessed: 2016-01-02. Available at: <http://physics.stackexchange.com/questions/78419/transverse-magnetic-tm-and-transverse-electric-te-modes>.

32 PEI, Z. et al. Application-oriented wireless sensor network communication protocols and hardware platforms: A survey. In: *Industrial Technology, 2008. ICIT 2008. IEEE International Conference on*. [S.l.: s.n.], 2008. p. 1–6.

33 BANDYOPADHYAY, L. K.; CHAULYA, S. K.; MISHRA, P. K. *Wireless Communication in Underground Mines: RFID-based Sensor Networking*. 1st. ed. [S.l.]: Springer Publishing Company, Incorporated, 2009. ISBN 0387981640, 9780387981642.

34 YIN, Z. J.; CHUNG, K.-S. Multiple access protocol for an underground mobile communication system. In: *Global Telecommunications Conference, 1998. GLOBECOM 1998. The Bridge to Global Integration. IEEE*. [S.l.: s.n.], 1998. v. 4, p. 2217–22224.

35 JING, G.; QIANPING, W. Application of hybrid routing protocol for mine WSN. In: *Environmental Science and Information Application Technology (ESIAT), 2010 International Conference on*. [S.l.: s.n.], 2010. v. 3, p. 353–355.

36 CHETAN, B. et al. Analysis of DSdv amp; aodv for disaster management system in coal mines. In: *Wireless Communications, Networking and Mobile Computing (WiCOM), 2011 7th International Conference on*. [S.l.: s.n.], 2011. p. 1–4. ISSN 2161-9646.

37 WU, D.; LI, R.; BAO, L. A holistic routing protocol design in underground wireless sensor networks. In: *Mobile Ad-hoc and Sensor Networks, 2008. MSN 2008. The 4th International Conference on*. [S.l.: s.n.], 2008. p. 187–194.

38 SUN, Y.; LIU, X. Wireless multi-hop ad hoc networks based on olsr for underground coal mine. In: *Wireless Communications and Signal Processing (WCSP), 2010 International Conference on*. [S.l.: s.n.], 2010. p. 1–6.

39 WENQI, C.; ZHAO, X. Multi-hop routing for wireless network in underground mines. In: *Wearable Computing Systems (APWCS), 2010 Asia-Pacific Conference on*. [S.l.: s.n.], 2010. p. 337–340.

40 JIANG, H.; PENG, J.; PENG, W. Nonuniform clustering routing protocol for tunnel wireless sensor network in underground mine. In: *Wireless Communications Signal Processing, 2009. WCSP 2009. International Conference on*. [S.l.: s.n.], 2009. p. 1–5.

41 ZHENG, Z.; HU, S. Research challenges involving cross-layered communication protocol design for underground WSNs. In: *Anti-counterfeiting, Security and Identification, 2008. ASID 2008. 2nd International Conference on*. [S.l.: s.n.], 2008. p. 120–123.

42 DURKIN, J. *Apparent Earth Conductivity Over Coal Mines as Estimated From Through-The-Earth Electromagnetic Transmission Tests*. United States Department of the Interior, Bureau of Mines, 1984.

43 YAN, L.; WAYNERT, J.; SUNDERMAN, C. Earth conductivity estimation from through-the-earth measurements of 94 coal mines using different elecetromagetic models. *Appl Comput Electromagn Soc. J*, v. 29, n. 20, p. 755–762, Oct. 2014.

44 LITTLE, A. *Detection of trapped miner Electromagetic signals above coal mines*. [S.l.], 1980.

45 MENDES, H. B. S. et al. Experimental platform for through-the-earth communication. In: *12th European Conference on Antennas and Propagation (EuCAP 2018)*. [S.l.: s.n.], 2018. p. 1–5.

46 RALCHENKO, M. et al. Near-field vlf electromagnetic signal propagation in multistory buildings. *IEEE Transactions on Antennas and Propagation*, v. 66, n. 2, p. 848–856, Feb 2018. ISSN 0018-926X.

47 KISSELEFF, S. et al. Localization of a silent target node in magnetic induction based wireless underground sensor networks. In: *2017 IEEE International Conference on Communications (ICC)*. [S.l.: s.n.], 2017. p. 1–7. ISSN 1938-1883.

48 KOROLKOVA, E. et al. Technological advancement for a novel through-the-earth communication system. In: *2018 IEEE Canadian Conference on Electrical Computer Engineering (CCECE)*. [S.l.: s.n.], 2018. p. 1–5. ISSN 2576-7046.

49 YENCHEK, M. R. et al. Niosh-sponsored research in through-the-earth communications for mines: a status report. *Industry Applications, IEEE Transactions on*, IEEE, v. 48, n. 5, p. 1700–1707, 2012.

50 AL., G. S. et. *To the rescue!* 2010. World Coal.

51 NEWS, E. *New Through Earth Communication System for Coal Mining*. 2014. Endeavour Magazine.

52 SAFETY, M.; ADMINISTRATION, H. *APPROVAL AND CERTIFICATION CENTER 9B APPROVALS*. 2019. Available at: <https://arlweb.msha.gov/TECHSUPP/ACC/lists/23teleph.pdf>.

53 GRIFFITHS, D. J. *Introduction to Electrodynamics*. 3a. ed. [S.l.]: Prentice Hall, 1999, p. 215 – 301. 215, 301 p.

54 STARKEY, D. B. Electromagnetic transmission and detection at deep depths. *Sandia Laboratories Report SLL-73-5278*, 1973.

55 SOUTERWEB. *ASSEMBLY OF THE 2008 DQ RECEIVER BOARDS WITH THE NEW 3496 Hz CLASS-E HIGH_EFFICIENCY BEACON DESIGN*. 2008. Accessed: 2016-01-09. Available at: <http://souterweb.free.fr/boitaoutils/prospection/annexes/NotesOnThe2008_DQReceiverBoards.html>.

56 LOKE, M. H. et al. Recent developments in the direct-current geoelectrical imaging method. *Journal of Applied Geophysics 95*, p. 135–156, 2013.

57 AYUSO, N. et al. Through-the-earth magnetic field propagation: Modelling for underground applications. *Electromagnetics in Advanced Applications, 2009. ICEAA '09. International Conference*, p. 525 – 528, 2009.

58 ABBAS, T. *Measurement Based Channel Characterization and Modeling for Vehicle-to-Vehicle Communications*. 215 p. Tese (Doutorado) — Lund University, 2014.

59 DURKIN, J. Surface vertical magnetic field produced by a finite loop buried in an earth containing a thin conducting sheet. *Radio Science*, Wiley Online Library, v. 32, n. 1, p. 19–23, 1997.

60 GEYER, R. G.; KELLER, G. V.; OHYA, T. *Research on the Transmission of Electromagetic Signals between mine workings and the surface*. Goldlen, Colorado, USA, 1974.

61 RAPPAPORT, T. S. *Wireless communications: Principles and practice*. 2nd. ed. [S.l.]: Prentice Hall, 2002. 153-154 p. (Prentice Hall communications engineering and emerging technologies series). Includes bibliographical references and index. ISBN 0130422320.

62 SEYBOLD, J. S. *Introduction to RF propagation*. Hoboken, N.J.: Wiley-Interscience, 2005. 146-158 p. ISBN 0471655961.

63 BUTTERWORTH, S. Effective resistance of inductance coils at radio frequency - part 1. experimental wireless & wireless engineer,. 1926.

64 AUSTIN, B. B. The effective resistance of inductance coils at radio frequency. experimental wireless & wireless engineer. 1934.

65 WATT, A. Vlf radio engineering. international series in electromagnetic waves: 14j. *Oxford: Pergamon Press.*, 1967.

66 DRUMMOND, I. Letters: Antenna design. cregj 10, 5. 1992.

67 BALANIS, C. A. *Antenna Theory: Analysis and Design. New York: John Wiley & Son.* [S.l.]: OXFORD, 1997.

68 SMITH, G. S. (Ed.). *Proximity Effect in Systems of Parallel Conductors. Journal of Applied Physics 43(5), 2196-2203.* 1972a.

69 SMITH, G. S. *Radiation Efficiency of Electrically Small Multitum Loop Antennas. IEEE Transactions on Antennas and Propagation 20(5), 656-657.* 1972b.

70 H., R. F. Noise model for low-frequency through-the-earth communication. *Radio Science*, v. 45, n. 6, 2010.

71 ALHAJ, H. M. M. et al. Power system harmonics estimation using LMS, LMF and LMS/LMF. In: *2014 5th International Conference on Intelligent and Advanced Systems (ICIAS)*. [S.l.: s.n.], 2014. p. 1–5.

72 NEVES, S. et al. Análise de ruído antrópico em comunicações através do solo. In: *Simpósio Brasileiro de Telecomunicações e Processamento de Sinais (SBrT)*. [S.l.: s.n.], 2017.

73 SCHLEGEL, C.; MALLAY, M.; TOUESNARD, C. Atmospheric magnetic noise measurements in urban areas. *IEEE Magnetics Letters*, v. 5, p. 1–4, 2014. ISSN 1949-307X.

74 FIELD, E.; LEWINSTEIN, M. Amplitude-probability distribution model for VLF/ELF atmospheric noise. *Communications, IEEE Transactions on*, IEEE, v. 26, n. 1, p. 83–87, Jan. 1978. ISSN 0090-6778.

75 SKOMAL, E. *Man-made radio noise*. [S.l.]: Van Nostrand Reinhold, 1978. ISBN 9780442276485.

76 BALANIS, C. *Antenna Theory: Analysis and Design*. 3rd. ed. [S.l.]: John Wiley and Sons, 2005.

77 YAN, L. et al. Statistical analysis and modeling of VLF/ELF noise in coal mines for through-the-earth wireless communications. In: *2014 IEEE Industry Application Society Annual Meeting*. [S.l.: s.n.], 2014. p. 1–5. ISSN 0197-2618.

78 MSHA. *Mine Improvement and New Emergency Response Act of 2006*. 2006. Accessed: 2016-01-06. Available at: <http://www.msha.gov/mineract/MineActAmmendmentSummary.asp>.

APPENDIX

I. MINER ACT OF 2006

The following text was extracted from United States Department of Labor website in January 6th 2016 [78]

"The Mine Improvement and New Emergency Response Act of 2006 would require operators of underground coal mines to improve accident preparedness. The legislation would require mining companies to develop an emergency response plan specific to each mine they operate, and require that every mine have at least two rescue teams located within one hour. S. 2803 would also limit the legal liability of rescue team members and the companies that employ them. The act would increase both civil and criminal penalties for violations of federal mining safety standards and would give the Mine Safety and Health Administration (MSHA) the ability to temporarily close a mine that fails to pay the penalties or fines. In addition, the act calls for several studies into ways to enhance mine safety, as well as the establishment of a new office within the National Institute for Occupational Safety and Health devoted to improving mine safety. Finally, the legislation would establish new scholarship and grant programs devoted to training individuals with respect to mine safety.

Key Provisions of the MINER Act:

- Require each covered mine to develop and continuously update a written emergency response plan;
- Promote use of equipment and technology that is currently commercially available;
- Require each mine's emergency response plan to be continuously reviewed, updated and re-certified by MSHA every six months;
- Direct the Secretary of Labor to require wireless two-way communications and an electronic tracking system within three years, permitting those on the surface to locate persons trapped underground;
- Require each mine to make available two experienced rescue teams capable of a one hour response time;
- Require mine operators to make notification of all incidents/accidents which pose a reasonable risk of death within 15 minutes, and sets a civil penalty of $5,000 to $60,000 for mine operators who fail to do so;
- Establish a competitive grant program for new mine safety technology to be administered by NIOSH;
- Establish an inter-agency working group to provide a formal means of sharing non-classified technology that would have applicability to mine safety;

- Raising the criminal penalty cap to $250,000 for first offenses and $500,000 for second offenses, as well as establishing a maximum civil penalty of $220,000 for flagrant violations;
- Give MSHA the power to request an injunction (shutting down a mine) in cases where the mine has refused to pay a final order MSHA penalty;
- Create a scholarship program available to miners and those who wish to become miners and MSHA enforcement staff to head off an anticipated shortage in trained and experienced miners and MSHA enforcement;
- Establish the Brookwood-Sago Mine Safety Grants program to provide training grants to better identify, avoid and prevent unsafe working conditions in and around the mines. These grants will be made on an annual, competitive basis to provide education and training for employers and miners, with a special emphasis on smaller mines."

II.1 3D MAGNETIC FIELD SIMULATION ON CST STUDIO SUITE

The following pages present a brief manual on how to build a simulation scenario for a TTE transmission system using the commercial software CST STUDIO SUITE.

For building the TTE transmission simulation computer environment, it is necessary to establish simulator options and constructing the simulation scenario. CST comes with a native application within the application that permit customization and simulation settings in a easy sequence as listed below:

1. Select an application area and a workflow. The application area depends on license purchased. For this investigation was acquired the Microwaves, Radio Frequencies and Optical license. This area opens six workflows: Antennas; Circuit & Components; Radar Cross Section; Biomedical, Exposure, SAR; Optical Applications, and Periodic Structures. Also it is possible to improve the workflow selection through more options according to each item.

2. Select the numerical method solver. According to each workflow, the software will suggest those methods recommended.

3. Select simulation units. For every simulation it is necessary to determine which units will be used for 3D structure building and simulation results.

4. Introduce frequency range or simulation time depending on selected method. In this stage is possible to determine frequency monitors for sensing E-field, H-Field, Power flow, Power losses and Far-field magnitudes.

5. 3D Structure construction. This stage is where physical characteristics of environment are defined. Using several 3D CAD functions is feasible to construct all structures needed. There is a grand material library for choosing from and it is possible to create new materials to fulfill specific conditions. Additionally, external CAD projects can be used to improve structure building velocity.

Aiming an acceptable relation between processing time and accuracy, it is important to select a suitable meshing of all structures and numerical method. CST offers two meshing options, a tetrahedral and hexahedral. Such option controls simulation time and it is available for both time and frequency domain. Figure II.1 shows how meshing adapts to each structure depending on its geometric characteristics. For simpler structures as cubic blocs, this adaptive meshing allows using bigger cells which diminish total node number and reduces time processing.

Border conditions are chosen in such way that numerical calculations can converge. That software offers usual conditions as: electric or magnetic planes, free space, conductive walls, periodic characteristic walls and unit cells. In figure II.2, all open boundaries are selected.

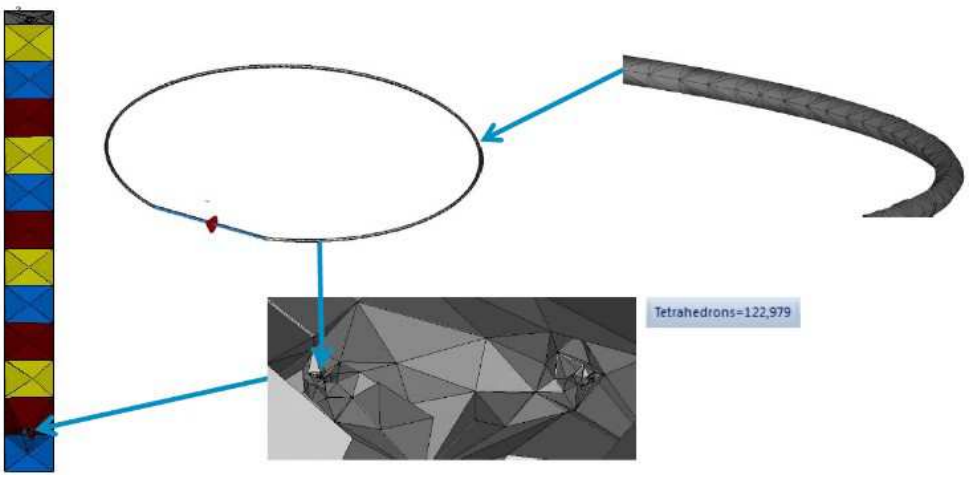

Figure II.1: Tetrahedral meshing

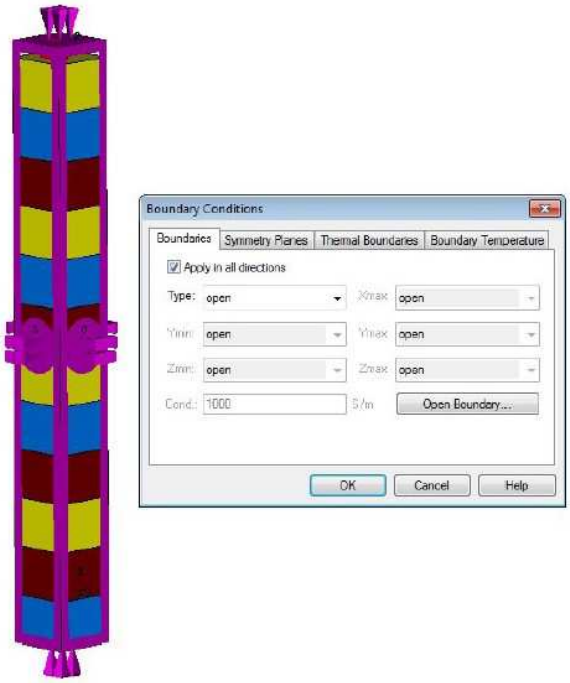

Figure II.2: Border conditions

Field intensities can be measured using probes located on positions of interest. Among that data, it is possible to measure voltages, currents, S parameters, and Z and Y matrix through ports on radiating structures. Generally, those responses are shown in 2D or 3D graphics, which can use several representations as logarithmic, polar, phase and magnitude. Some of them can be visualized as 3D animated images as a function of time and space changing colors for giving motion sensation. Also, it is feasible to use 3D vector plots with arrows, cones, hedgehog shape lines and streamlines that moves according to field's direction. In figure II.3 is represented a frame of an animated 3D image where is indicated magnetic field variations on space.

Commercial software, as CST STUDIO SUITE, have post-processing tools that include pro-

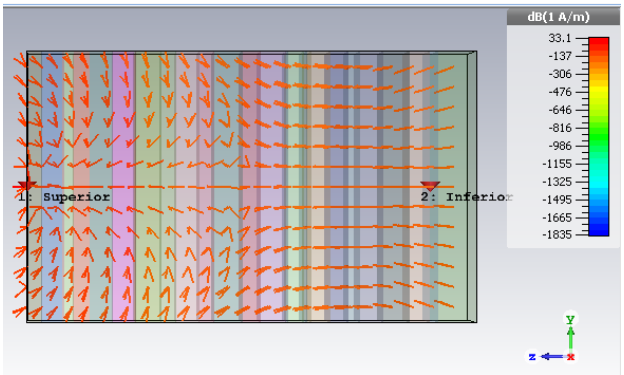

Figure II.3: Magnetic field inside substrates

grammable routines. Result data can be processed directly at CST for generating new graphics and comparing them to theoretical data without using any other software. Additionally, for some more complex calculation it is possible to use VBA code for upgrading post-processing analysis. Next figure represents a result obtain with CST.

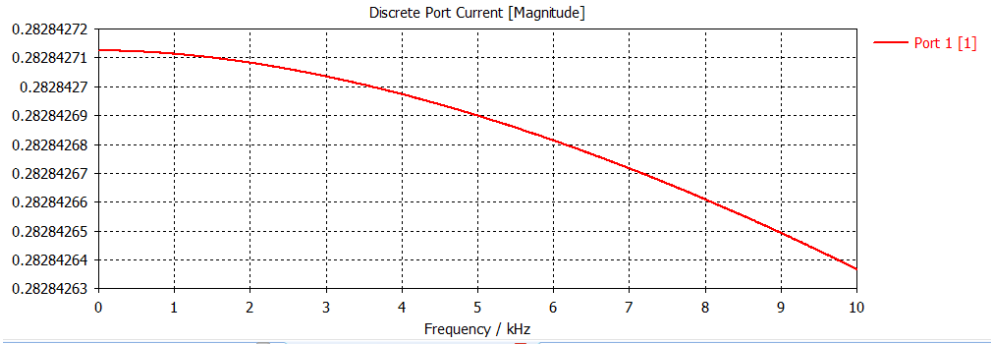

Figure II.4: Current result in linear scale